AD NUMBER

AD822008

LIMITATION CHANGES

TO:

Approved for public release; distribution is unlimited.

FROM:

**Distribution authorized to U.S. Gov't. agencies and their contractors;
Administrative/Operational Use; OCT 1967. Other requests shall be referred to Rome Air Development Center, Rome, NY.**

AUTHORITY

AFSC ltr 14 Oct 1971

RADC-TR-67-502

EXPANDED LITTLE IDA - INSTRUMENTATION

Raymond J. Coates
General Electric Company HMED

TECHNICAL REPORT NO. RADC-TR-67-502
October 1967

Rome Air Development Center
Air Force Systems Command
Griffiss Air Force Base, New York

When US Government drawings, specifications, or other data are used for any purpose other than a definitely related government procurement operation, the government thereby incurs no responsibility nor any obligation whatsoever; and the fact that the government may have formulated, furnished, or in any way supplied the said drawings, specifications, or other data is not to be regarded, by implication or otherwise, as in any manner licensing the holder or any other person or corporation, or conveying any rights or permission to manufacture, use, or sell any patented invention that may in any way be related thereto.

Do not return this copy. Retain or destroy.

EXPANDED LITTLE IDA – INSTRUMENTATION

Raymond J. Coates
General Electric Company HMED

AFLC, GAFB, N.Y., 23 Oct 67-145

FOREWORD

The fifth interim report was prepared by the General Electric Company, Advance Development Engineering, Heavy Military Electronics Department, Syracuse, New York, under Contract AF3-(602)-3946, Project No. 5582, Task No. 558202.

This technical documentary report represents the efforts of a number of contributors who had an important part in writing various parts of this document. The editorial responsibility for this report was assigned to Raymond J. Coates. The list of the individual contributors follows: Raymond J. Coates, Ted C. Matsumoto, Edward K. Mofford, Mathew R. Scalzetti, Robert D. Wengenroth, and Eugene D. Wurdinger.

RADC Project Engineer was Robert A. Mather (EMASA).

Release of subject report to the general public is prohibited by the Strategic Trade Control Program, Mutual Defense Assistance Control List (revised 6 January 1965) published by the Department of State.

This technical report has been reviewed and is approved.

Approved: Robert A. Mather

Robert A. Mather
Contract Engineer

Approved Joseph Fallik

Joseph Fallik
Chief, Space Surveillance and Instrumentation Branch
Surveillance and Control Division

ABSTRACT

This fifth interim report describes the work performed on Contract AF30(602)-3946, from 15 September 1966 to 15 June 1967 in the area of instrumentation. The Expanded Little IDA Program is a continuation, as well as an expansion, of the effort previously carried out under Contract AF30(602)-3360 to investigate the characteristics of ionospherically propagated high frequency signals. The long term objective of these studies is to provide more accurate estimates of the major environmental factors needed for over-the-horizon radar system design. The equipment described in this report is being designed and installed to provide the proper tools to meet this objective.

The overall block diagrams and status for each of the three transmitter sites and the common receiver site are discussed in the introductory section. In the following sections, equipment developments not previously reported (Interim Reports Nos. 1 and 3 on this program) are discussed. In the first of these sections the status of each of the antenna installations is discussed and an analysis of the ground screen requirements for the Starr Hill receiver site is given. The system parameters for the noise/interference system are given, along with the latest status of the major component of this system, a high dynamic range high frequency receiver. The design details, alignment, and operating instructions for the completed mode processor are given. The concluding section on azimuth of arrival discusses both the system objectives and the equipment developments to meet these objectives.

TABLE OF CONTENTS

TABLE OF CONTENTS (concluded)

LIST OF ILLUSTRATIONS

LIST OF ILLUSTRATIONS (concluded)

SECTION I

INTRODUCTION

This technical documentary report reviews work performed from 15 September 1966 to 15 June 1967 on U.S. Air Force Contract AF30(602)-3946 under supervision of the Rome Air Development Center in providing instrumentation for the Expanded Little IDA Program. The long term objective of this program is to provide more accurate estimates of the major environmental factors needed for the over-the-horizon radar (OHR) system design. This program is a continuation, as well as expansion, of the effort previously carried out under U.S. Air Force Contract AF30(602)-3360, also directed by the Rome Air Development Center, to determine the characteristics of ionospherically propagated high frequency (HF) signals. The experiment design, data reduction, and data analysis being performed under this contract have been discussed in Interim Reports Nos. 2 and 4 on this program. In addition, instrumentation developments have been given in Interim Reports Nos. 1 and 3; hence, only new work performed since the last report will be presented.

1. STARR HILL RECEIVER SITE

Since the last report, Starr Hill -- near Remsen, New York -- has been implemented as the new receiver site. The move to Starr Hill was accomplished during March 1967. The equipment layout at the new site is shown in Figure 1.

A functional block diagram of this receiver complex is shown in Figure 2. This block diagram was discussed in detail in Interim Report No. 1. Two important changes have been incorporated into the system since that time. Since no Eastern site was available, installation of the eastward looking horizontal and vertical log periodic antennas has been deferred indefinitely. The use of two separate receivers for the azimuth of arrival experiment has been discontinued. Instead, both signals are being time multiplexed through one receiver. The reasons for this change and the equipment details are described in Section V.

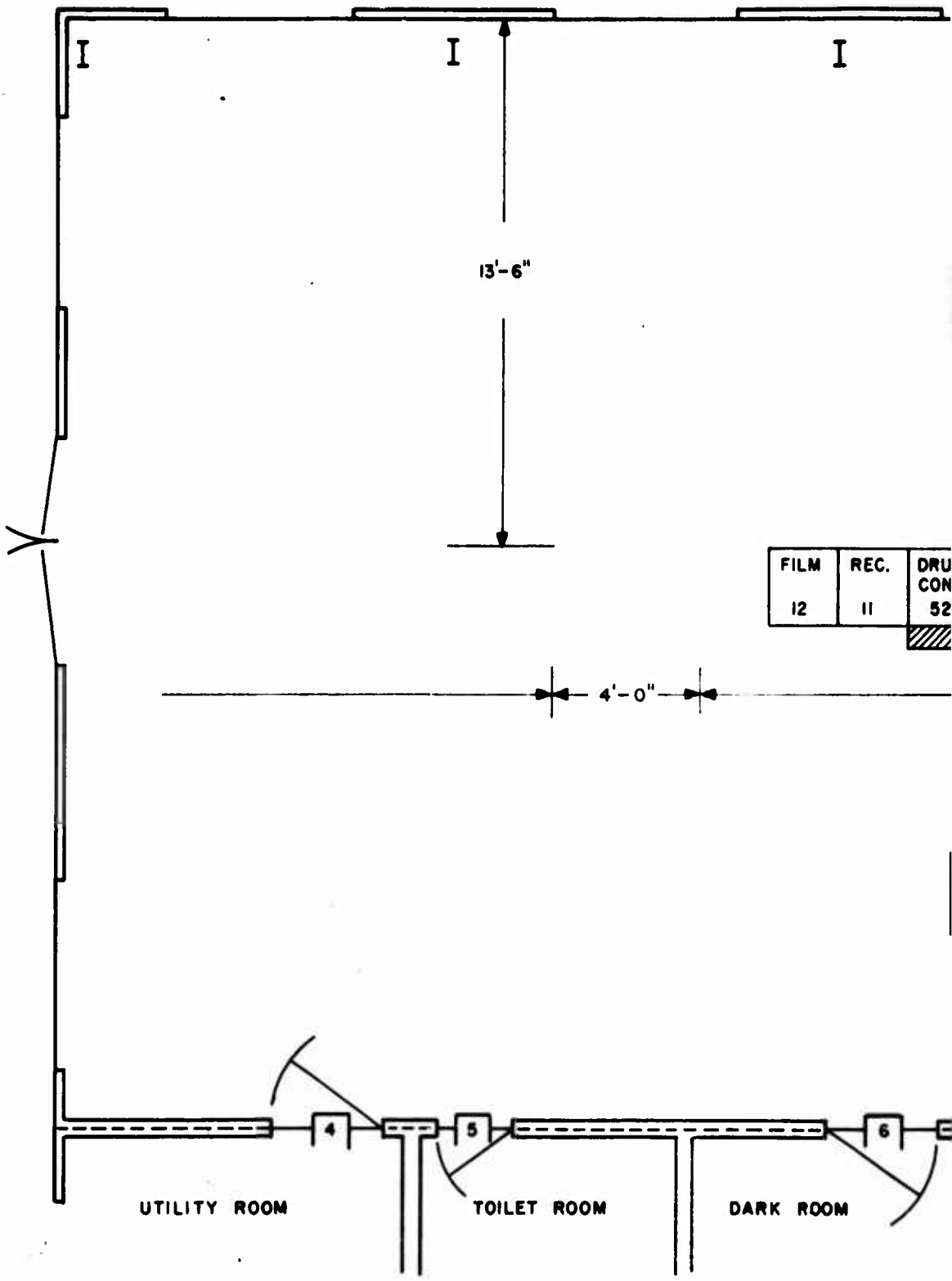
I
I
I
13'-6"
FILM
REC.
DRU
CON
12
11
52
4'-0"
4
5
6
UTILITY ROOM
TOILET ROOM
DARK ROOM

1

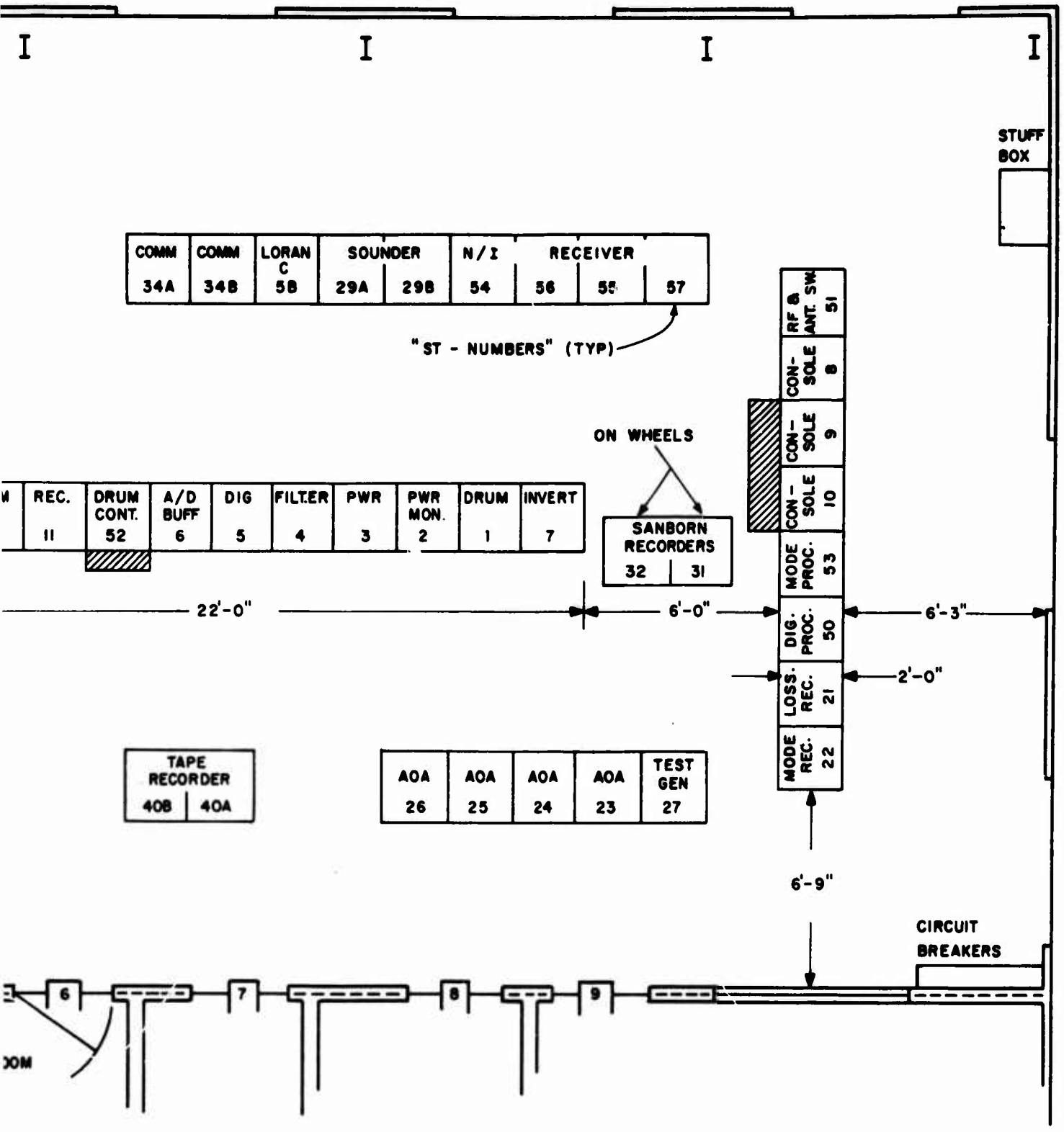

Figure 1. Receiver Site Equipment Layout

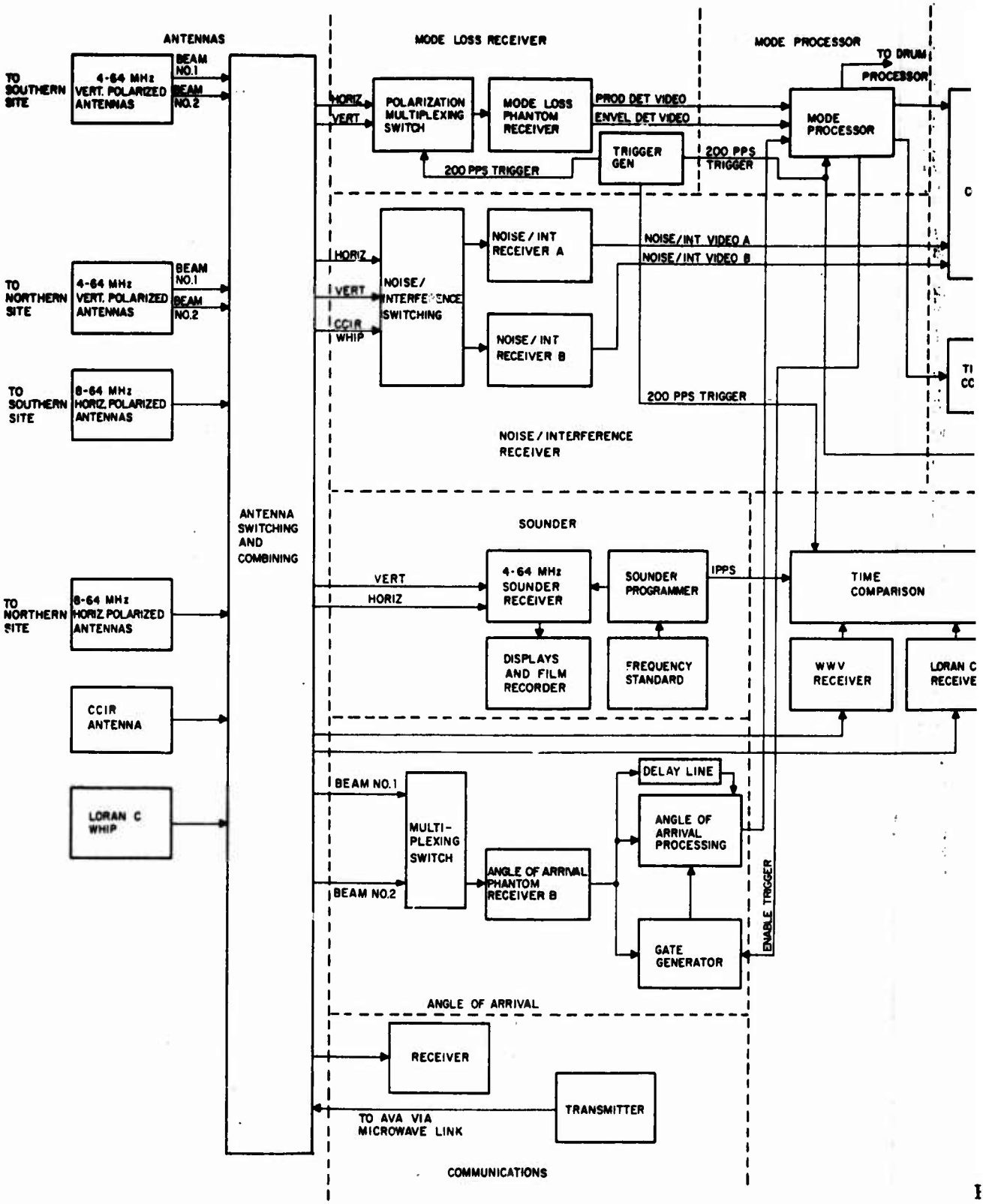
ANTENNAS
MODE LOSS RECEIVER
MODE PROCESSOR
TO DRUM PROCESSOR
TO SOUTHERN SITE
4-64 MHz VERT. POLARIZED ANTENNAS
BEAM NO.1
BEAM NO.2
HORIZ
VERT
POLARIZATION MULTIPLEXING SWITCH
MODE LOSS PHANTOM RECEIVER
PROD DET VIDEO
ENVEL DET VIDEO
MODE PROCESSOR
TRIGGER GEN
200 PPS TRIGGER
200 PPS TRIGGER
TO NORTHERN SITE
4-64 MHz VERT. POLARIZED ANTENNAS
BEAM NO.1
BEAM NO.2
HORIZ
VERT
CCIR WHIP
NOISE/ INTERFERENCE SWITCHING
NOISE / INT RECEIVER A
NOISE / INT RECEIVER B
NOISE/INT VIDEO A
NOISE/INT VIDEO B
200 PPS TRIGGER
NOISE / INTERFERENCE RECEIVER
TO SOUTHERN SITE
8-64 MHz HORIZ. POLARIZED ANTENNAS
ANTENNA SWITCHING AND COMBINING
SOUNDER
TO NORTHERN SITE
8-64 MHz HORIZ. POLARIZED ANTENNAS
VERT
HORIZ
4-64 MHz SOUNDER RECEIVER
SOUNDER PROGRAMMER
1PPS
TIME COMPARISON
DISPLAYS AND FILM RECORDER
FREQUENCY STANDARD
WWV RECEIVER
LORAN C RECEIVE
CCIR ANTENNA
LORAN C WHIP
BEAM NO.1
BEAM NO.2
MULTI-PLEXING SWITCH
DELAY LINE
ANGLE OF ARRIVAL PROCESSING
ANGLE OF ARRIVAL PHANTOM RECEIVER B
GATE GENERATOR
ENABLE TRIGGER
ANGLE OF ARRIVAL
RECEIVER
TRANSMITTER
TO AVA VIA MICROWAVE LINK
COMMUNICATIONS

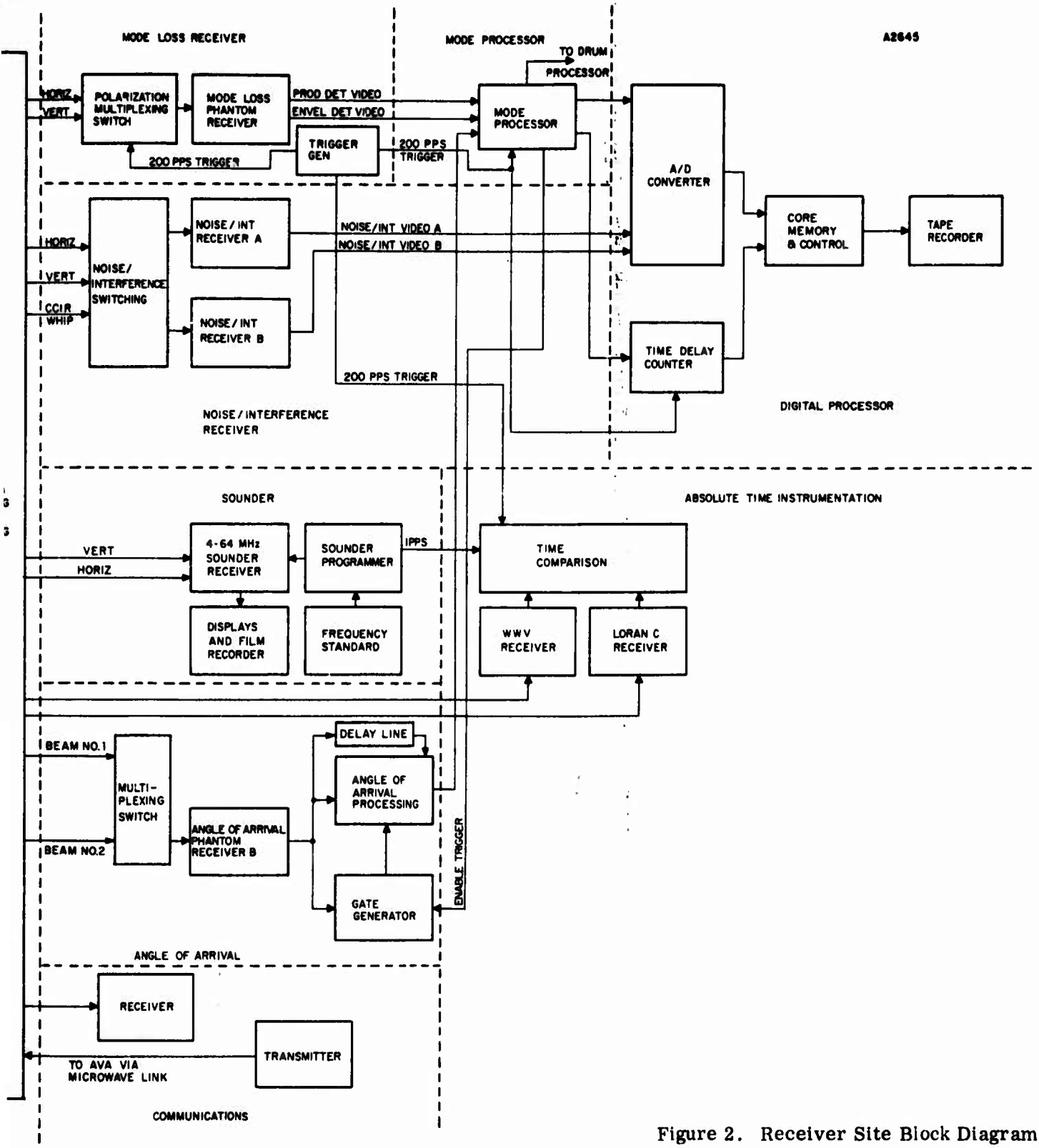

Figure 2. Receiver Site Block Diagram

2. COCO SOLO TRANSMITTER SITE

The functional block diagram of the Coco Solo transmitter site is shown in Figure 4. This diagram is essentially the same as that included in the previous reports as the transmitter site block diagram. It has, however, been modified to indicate the setup at the older Coco Solo site. From a functional point of view, the differences between this site and the newer Thule site are trivial. These differences in the areas of antennas and antenna switching are caused by maximum utilization of existing equipment. Figure 3 is a layout of the Coco Solo equipment room.

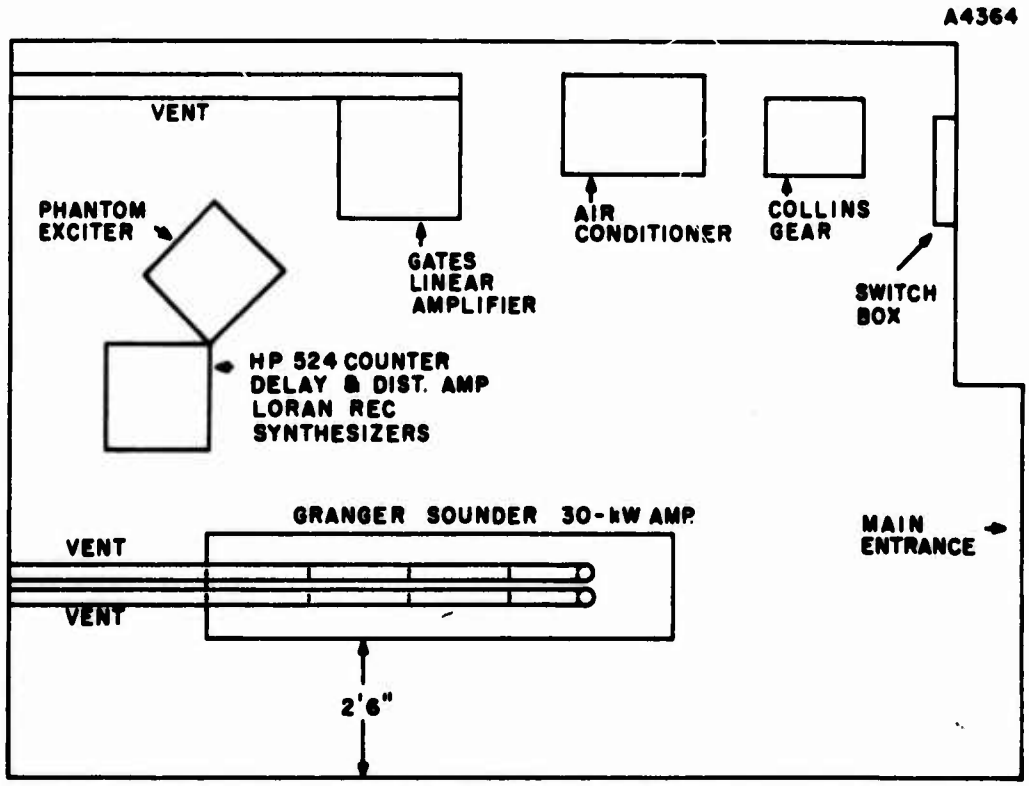

Figure 3. Coco Solo Transmitter Site Layout

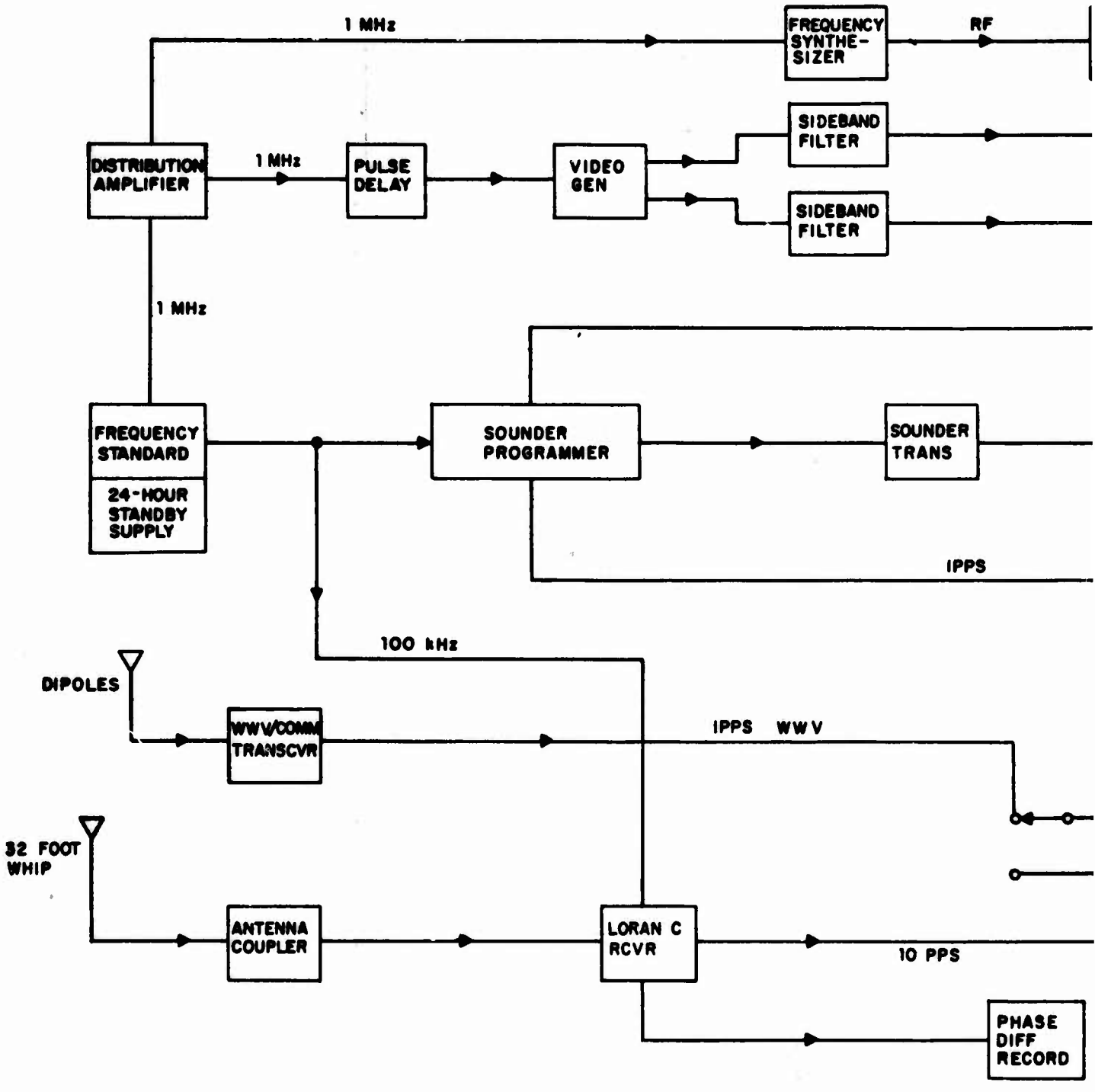
1 MHz
FREQUENCY SYNTHE-SIZER
RF
SIDEBAND FILTER
DISTRIBUTION AMPLIFIER
1 MHz
PULSE DELAY
VIDEO GEN
SIDEBAND FILTER
1 MHz
FREQUENCY STANDARD
24-HOUR STANDBY SUPPLY
SOUNDER PROGRAMMER
SOUNDER TRANS
IPPS
100 kHz
DIPOLES
WWV/COMM TRANSCVR
IPPS WWV
32 FOOT WHIP
ANTENNA COUPLER
LORAN C RCVR
10 PPS
PHASE DIFF RECORD

1

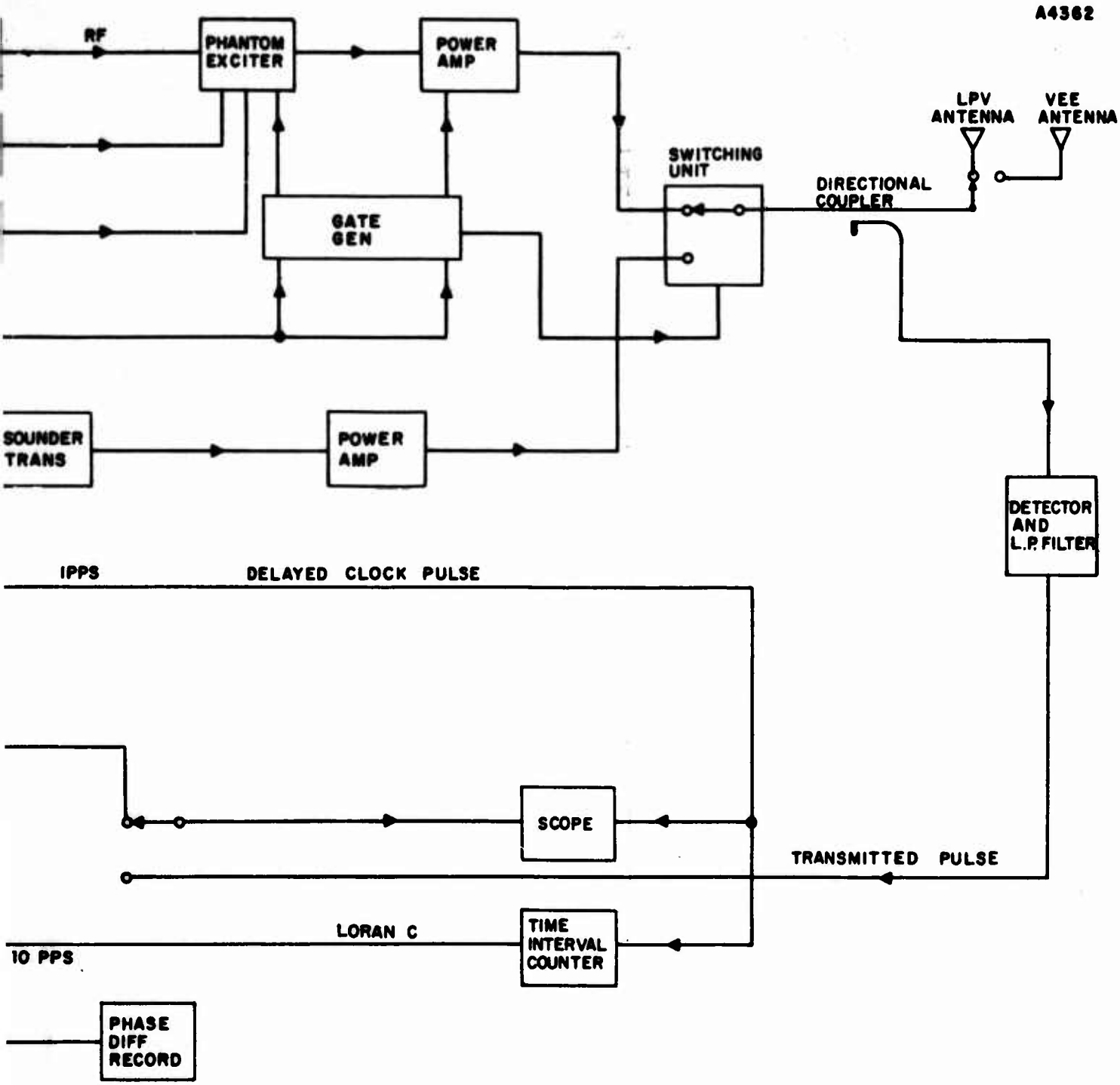

Figure 4. Coco Solo Transmitter Site Block Diagram

2

3. THULE TRANSMITTER SITE

The functional block diagram of the Thule transmitter site is shown in Figure 6. The distinguishing features of the Thule setup are the inclusion of a second RF switching unit to permit the communications transmitter to be connected to the LPV antenna in place of the Phantom transmitter. This switch is manually operated. A 200-foot horizontal antenna is employed at Thule in place of the 32-foot whip for Loran C; this arrangement yields improved reception. The equipment layout at the Thule "P" Mountain site is shown in Figure 5; this site is now operational.

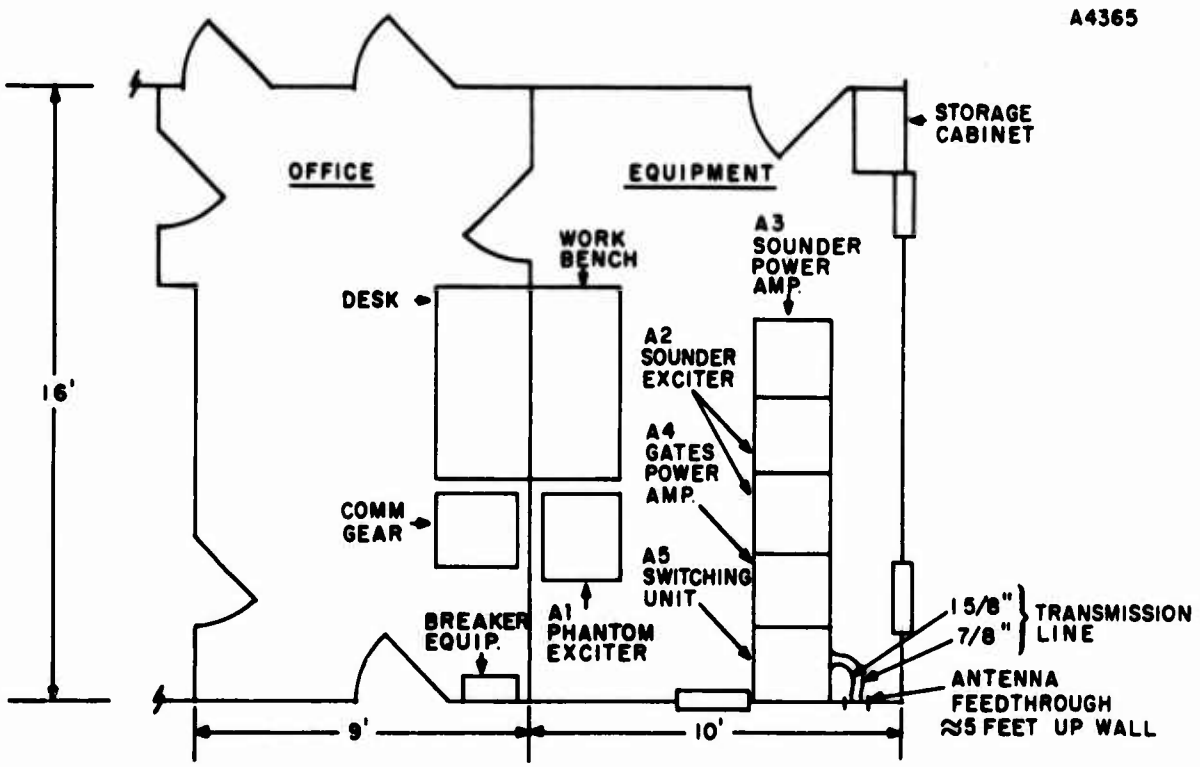

Figure 5. Thule Transmitter Site Layout

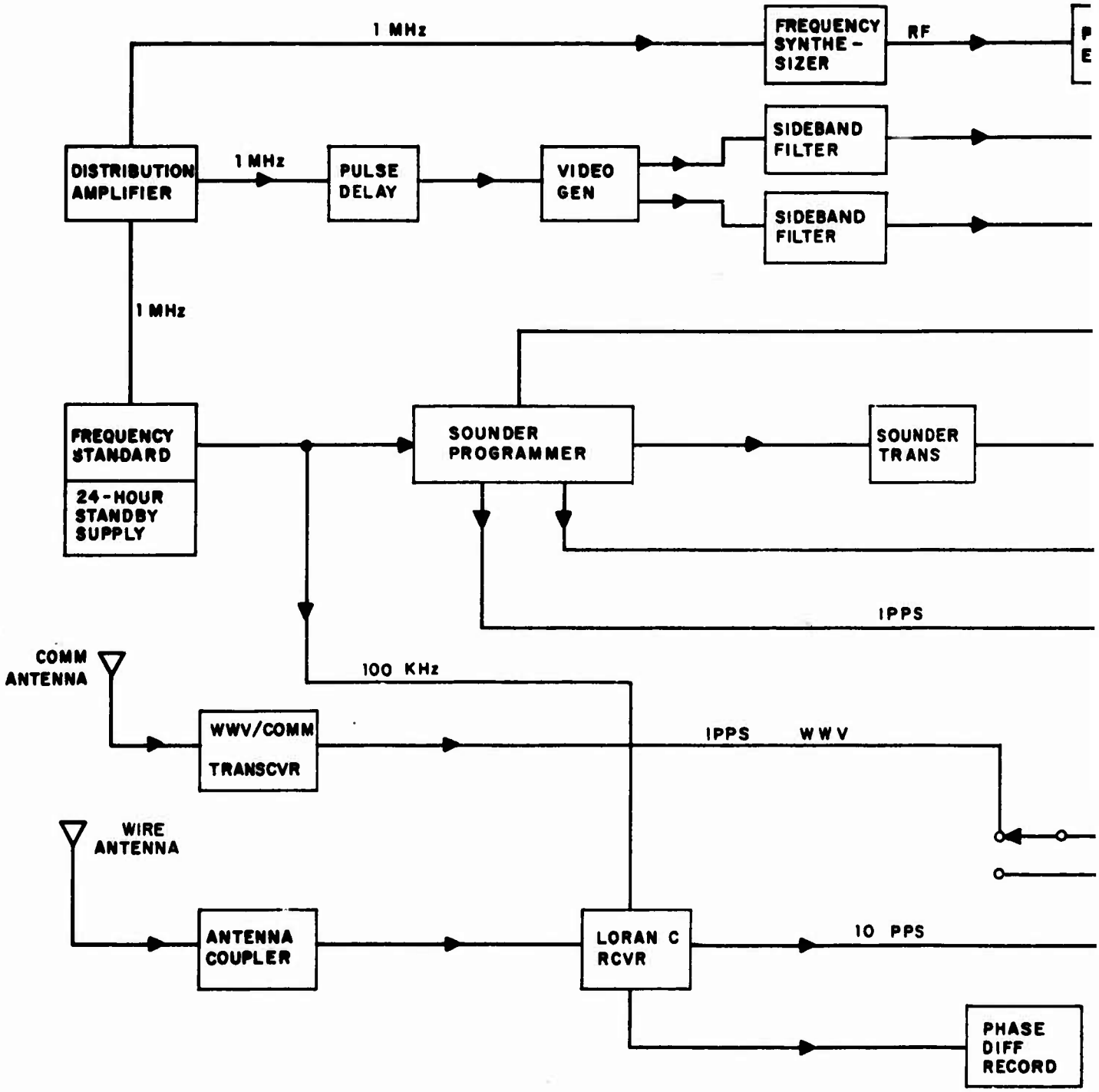
1 MHz
FREQUENCY SYNTHE-SIZER
RF
DISTRIBUTION AMPLIFIER
1 MHz
PULSE DELAY
VIDEO GEN
SIDEBAND FILTER
SIDEBAND FILTER
1 MHz
FREQUENCY STANDARD
24-HOUR STANDBY SUPPLY
SOUNDER PROGRAMMER
SOUNDER TRANS
1PPS
COMM ANTENNA
100 KHz
WWV/COMM TRANSCVR
1PPS
WWV
WIRE ANTENNA
ANTENNA COUPLER
LORAN C RCVR
10 PPS
PHASE DIFF RECORD

A4363

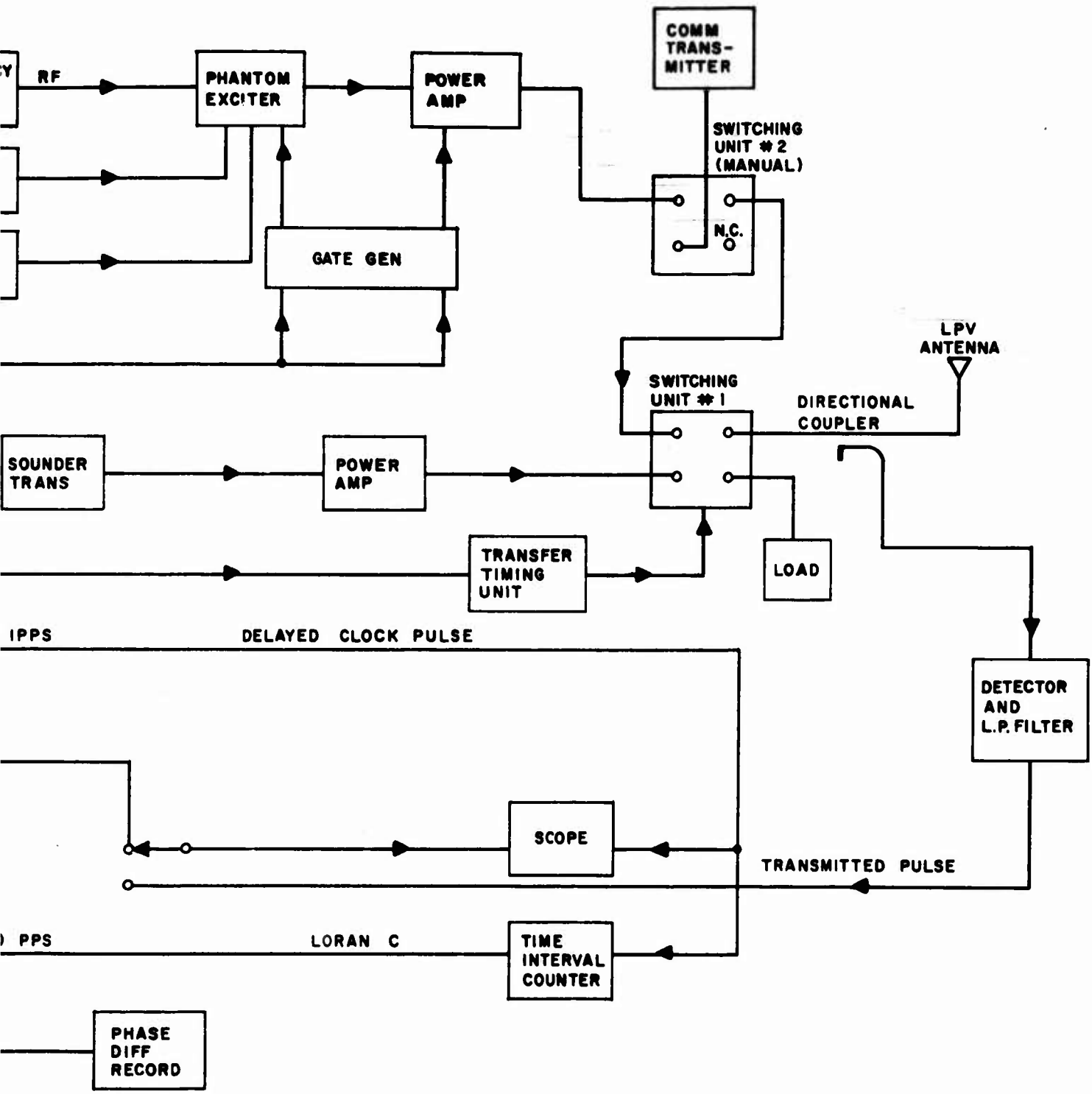

Figure 6. Thule/Keflavik Transmitter Site Block Diagram

2

4. KEFLAVIK TRANSMITTER SITE

Since no location directly east of Starr Hill at the proper range appeared to be available in the near future, the decision has been made to instrument a third transmitter site at Keflavik, Iceland. This site will enable data to be obtained over a path oblique rather than perpendicular to the line of maximum aurora disturbance as is the case with the Thule site. The functional block diagram of the yet-to-be installed Keflavik site is identical to the Thule diagram shown in Figure 5. It will employ equipment already available, with the exception of a Granger Model 726-5 LPV antenna which has just been procured.

SECTION II

ANTENNAS

The status of work on the Expanded Little IDA antennas is given in this section. Because the measurements of some of these antennas are not complete, the full description and calibration data are not yet available. As stated in Interim Report No. 2, these data will be presented in the final report.

1. STARR HILL RECEIVER SITE

a. Antenna Structures

The specifications for the antennas for the Starr Hill site are identified as SK 62667-782-11 and appeared as Appendix A of Interim Report No. 3. The antennas were manufactured and installed by American Electronics Laboratories, Inc. (AEL), Colmar, Pennsylvania. The antennas are basically revisions of existing designs, although the modifications proved more extensive than originally expected.

After the land was cleared so that precise contour information could be obtained, an error was found in one area on the east side of the Coco Solo directed antenna site which forced a change to a 4-3/4 percent slope. A resurvey to the Thule-directed antenna site shifted the elevation contour values for this area, necessitating a revision in the reference level for these antennas to 1780 feet.

The performance of the antennas was assured by close control of dimensions. The effects of the surroundings were potentially large enough that no technique for measuring the phase performance of the antennas appeared satisfactory.

Pattern data are being obtained as part of the calibration of the antennas. The design was accepted on the basis of previous model data. High power performance was also accepted on the basis of previous experience.

The VSWRs of the antennas were measured by a combination of point-by-point and swept techniques. The results, as reported by AEL, appear in Figures 7 through 11. The VSWRs exceed the specified 2:1 at a few points; the system implications are being explored before final acceptance of the antennas. Some of the peaks in the point-by-point data are unrealistically high and may be due to equipment limitations; this is being checked. Coco Solo curtain "A" was not measured by the sweep technique because the sweep detector picked up too much signal from a local broadcast station.

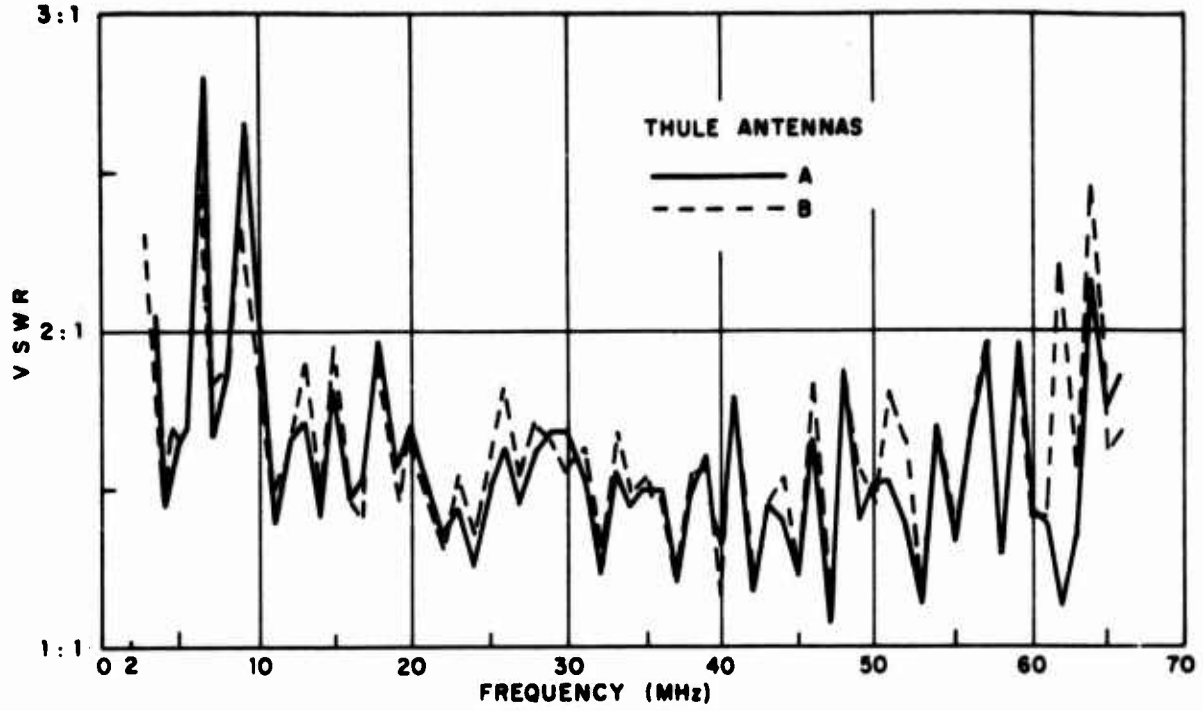

Figure 7. VSWR of Thule-Directed Vertically Polarized Antenna

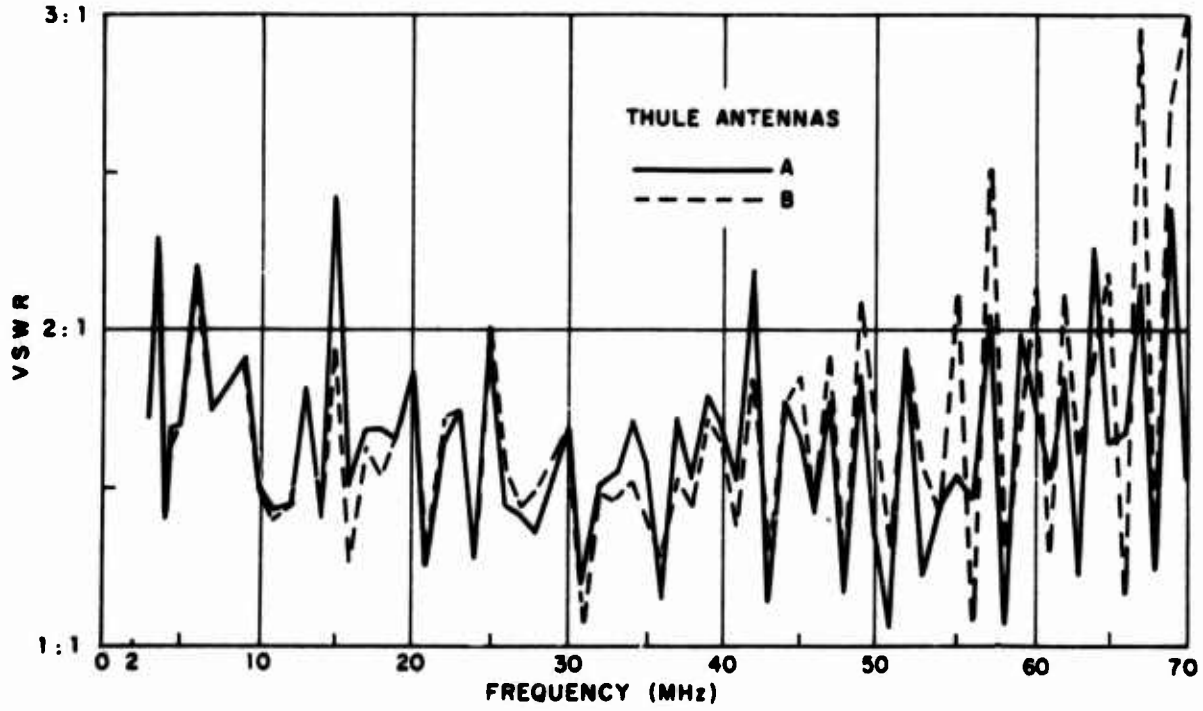

Figure 8. VSWR of Coco Solo-Directed Vertically Polarized Antenna

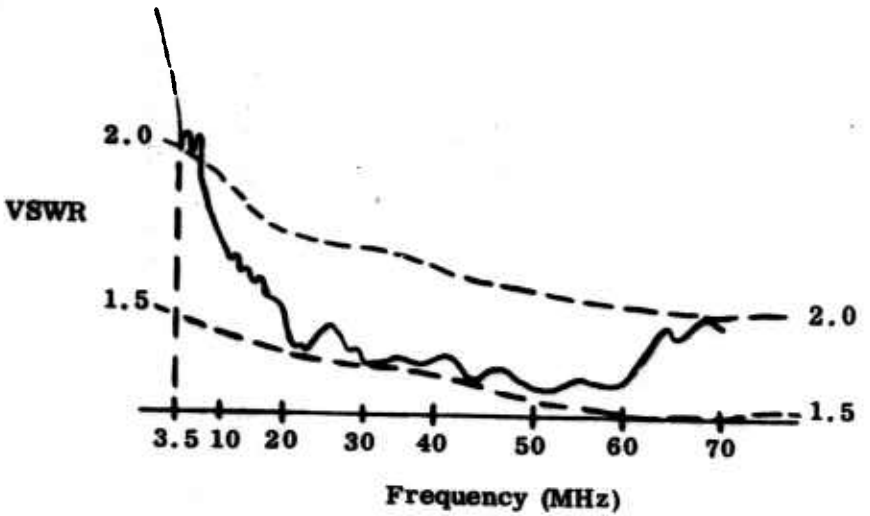

a. VSWR of Thule A Vertical Array at Antenna Input

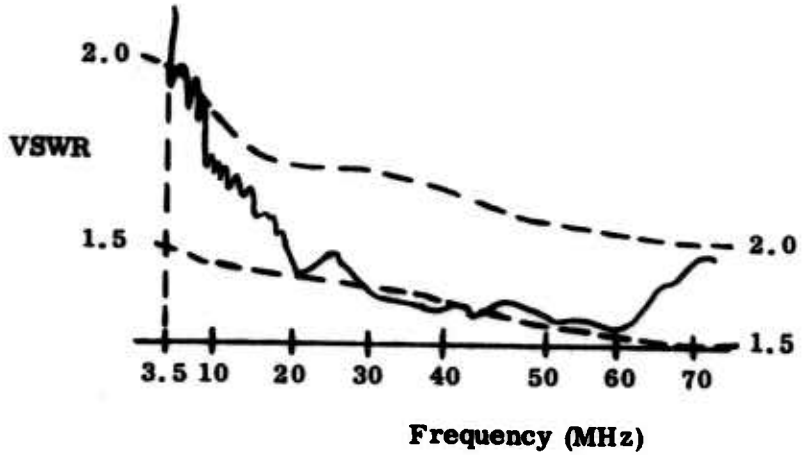

b. VSWR of Thule B Vertical Array at Antenna Input

Figure 9. VSWR by Swept Technique of Thule Vertical Antennas

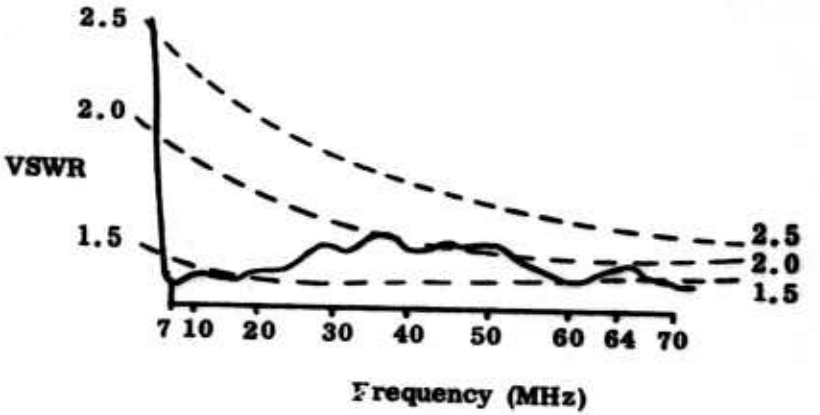

a. VSWR of Thule Horizontal Array at Antenna Input

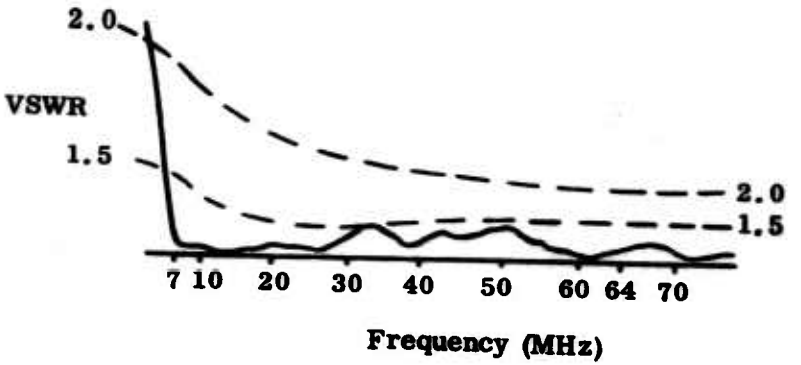

b. VSWR of Panama Horizontal Array at Antenna Input

Figure 10. VSWR by Swept Technique of Horizontal Antennas

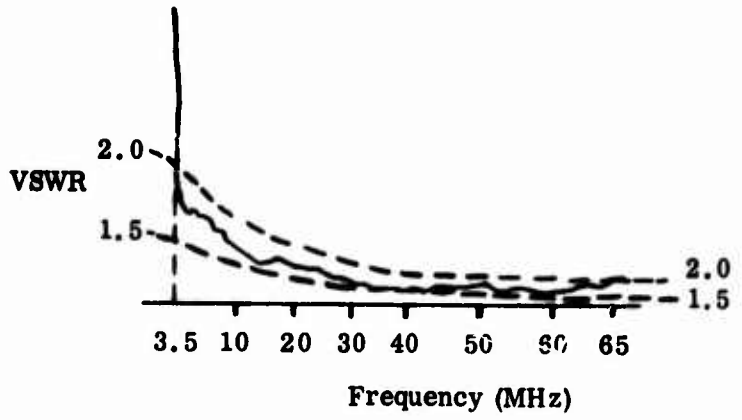

Figure 11. VSWR by Swept Technique of Coco Solo Curtain B Vertical Antenna

Calibration of the gain of the antennas is a service being provided by the RADC. The initial data indicate satisfactory performance. Full calibration is not expected to be completed before late summer; the data to be gathered by 1 Aubust should be sufficient for meaningful data reduction with the possibility that some modification would be needed if the remaining tests uncovered unexpected lobing from the surrounding terrain.

b. Ground Screens

A comparison was made of antenna performance with and without a ground screen. A value analysis showed that for the present the ground screen should be omitted. This was based upon the cost and the possibility that the installation might be halted by winter weather, making the patterns uncertain and the antennas effectively nonoperable.

Computations have been made of the field intensity at the nominal phase center of the vertical antennas for the cases of a 500-foot ground screen -- where the phase center is one-quarter wavelength above the screen -- and for no screen -- where the heights have been determined from the measured topography and given in Table I. To compare these data, it is necessary to insert the effective slope of the hill beyond the antenna. Note that these are "local" patterns; that is, the effects of the ridges miles from the site are not included.

The slope of the ground screen was originally designed to be 2.75°. Actually, the ground screen will have to follow the ground falloff somewhat. In the figures which follow, a slope of 3° was selected as an averaged effect. The effects of other averaged angles can be estimated by shifting the elevation angle scale.

TABLE I

HEIGHTS OF PHASE CENTERS ABOVE GROUND

Frequency (MHz)	Height (Wavelength)	
	Coco Solo Area	Thule Area
4	0.23	0.22
10	0.25	0.31
20	0.32	0.53
30	0.42	0.70
64	0.70	1.30

The mean slopes for the Coco Solo and Thule-directed antennas have been estimated at 6° and 9°, respectively. The Keflavik path is essentially the same as the Thule path. These values were applied in plotting the patterns. The patterns are those for the heights of the Coco Solo array as given in Table I; the effect of greater height on the Thule directed antenna has been estimated as about 1 dB. The curves have not been replotted for this report.

The patterns are presented in Figures 12 through 14. In a column are presented these cases as follows: (1) with ground screen (3° slope), (2) Coco Solo-directed array (6° slope), and (3) Thule-directed array (9° slope). The left column is for dry snow; the right column is for wet ground. Two intermediate cases of ground conditions are shown in Figure 15.

A horizontal pattern computed for nominal height above a smooth earth is shown in Figure 16. The slopes of 3°, 6°, and 9° cause effects approximately as shown by the shifted scales. Actually, the peak gain will probably be lower by perhaps 1 or 2 dB, and the pattern broader because the hills are not smooth slopes of indefinite length.

The angles of arrival for the modes of major interest are given in Table II. Other complex modes may arrive at intermediate angles.

Gains with and without the ground screen, and for the horizontal antenna, are most readily compared at these angles of major interest. The comparisons appear in Figures 17 through 21. A spreading loss of 1 dB was assumed for the horizontal antenna. No comparison was made for the higher angular limit of the two-hop F2 (2F2) mode, since the limit is above the range of the existing plots. Note that one advantage of omitting the ground screen is that, at the lower angles as well as the higher elevation angles, the variation of gain with elevation angle is comparable for the two polarizations.

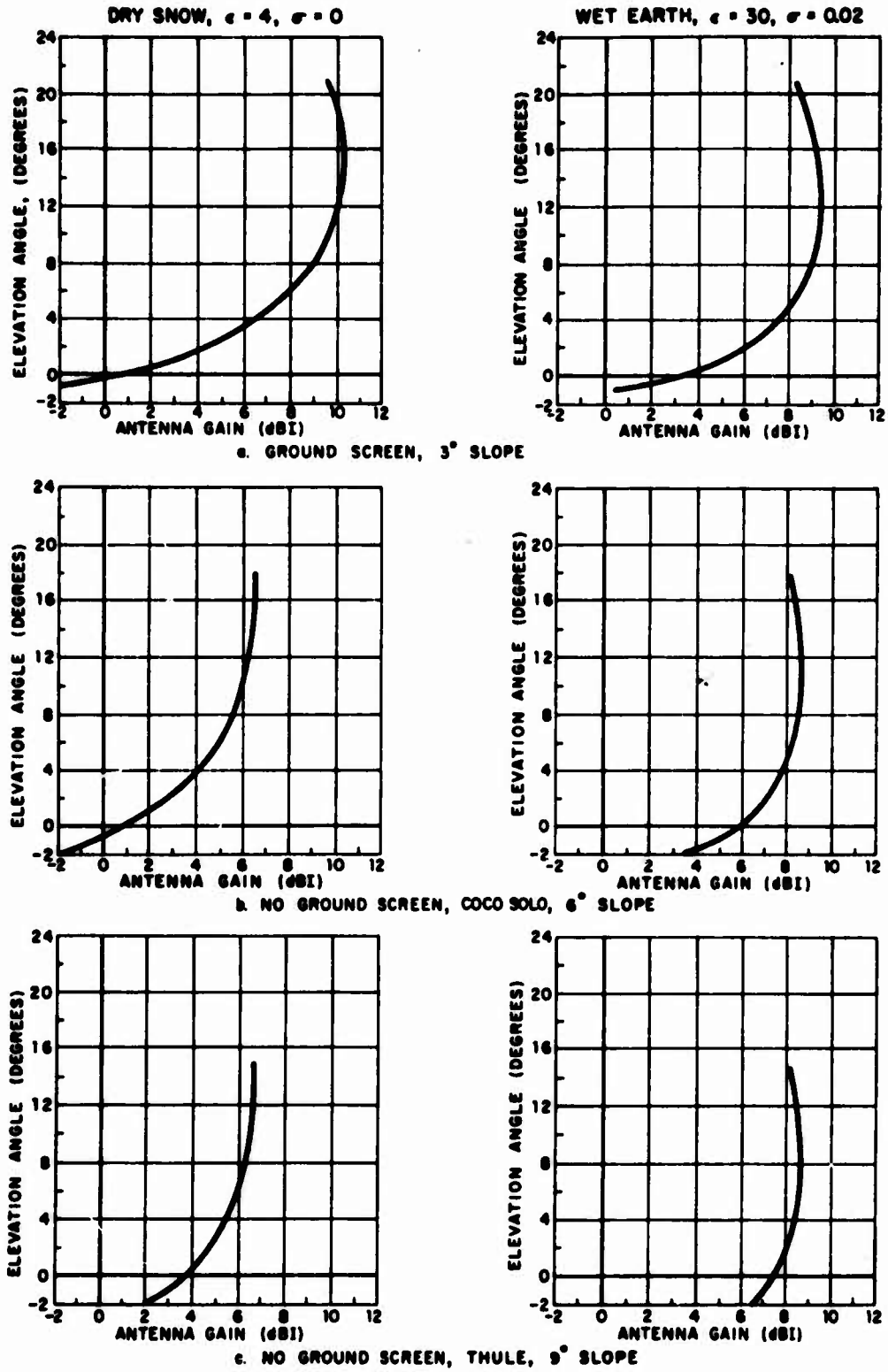

Figure 12. Computed Antenna Patterns at 10 MHz

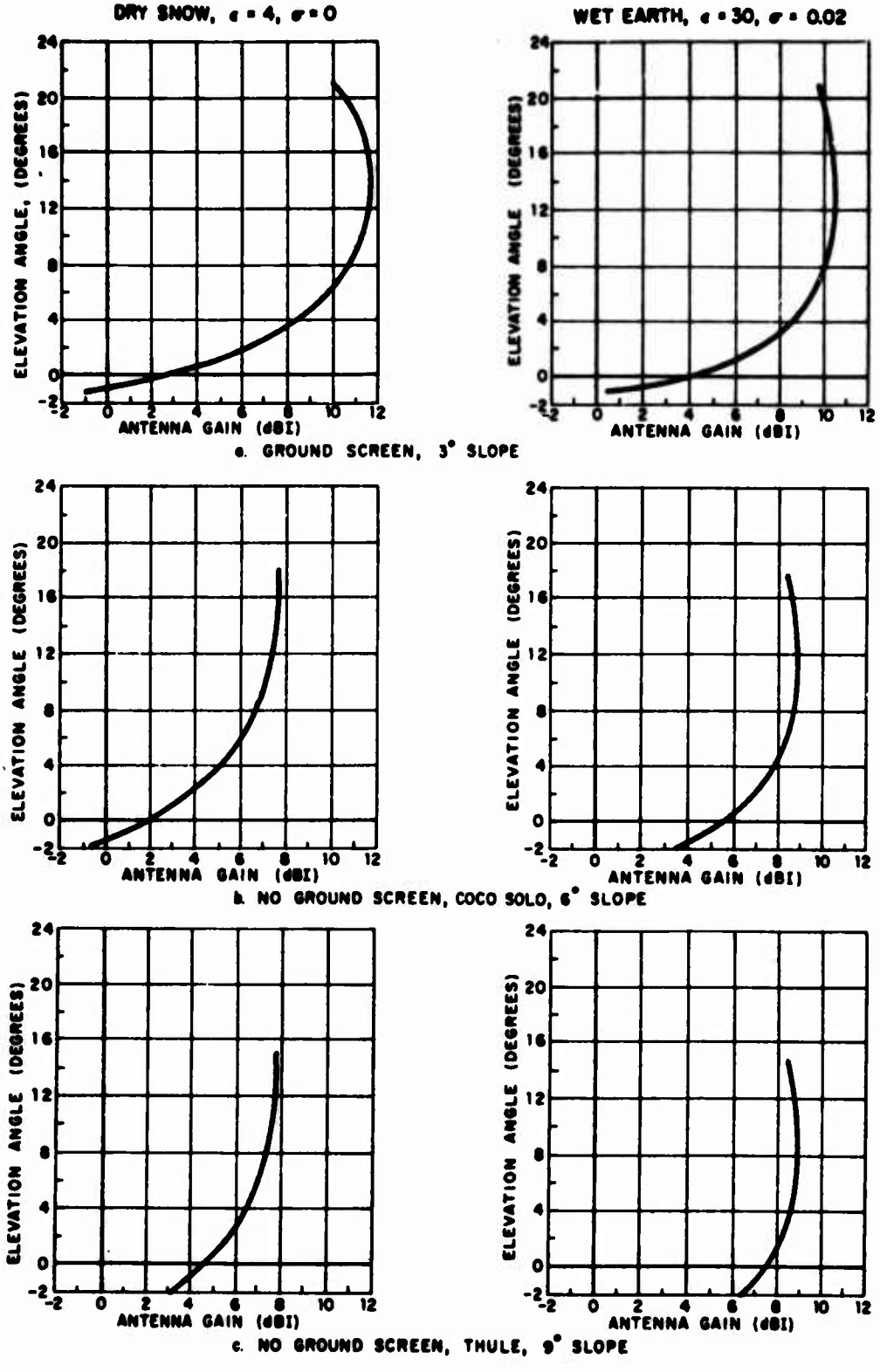

Figure 13. Computed Antenna Patterns at 20 MHz

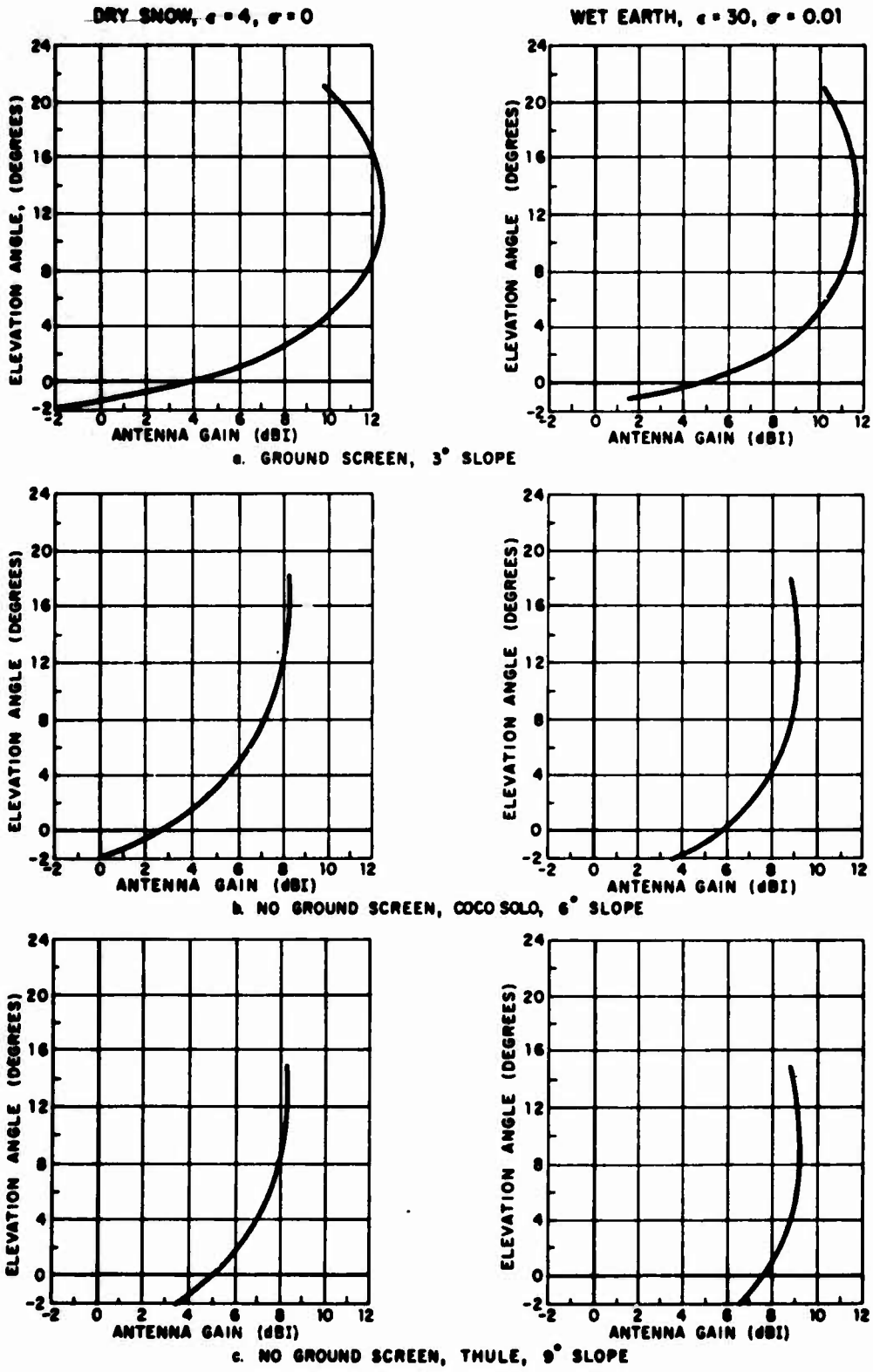

Figure 14. Computed Antenna Patterns at 30 MHz

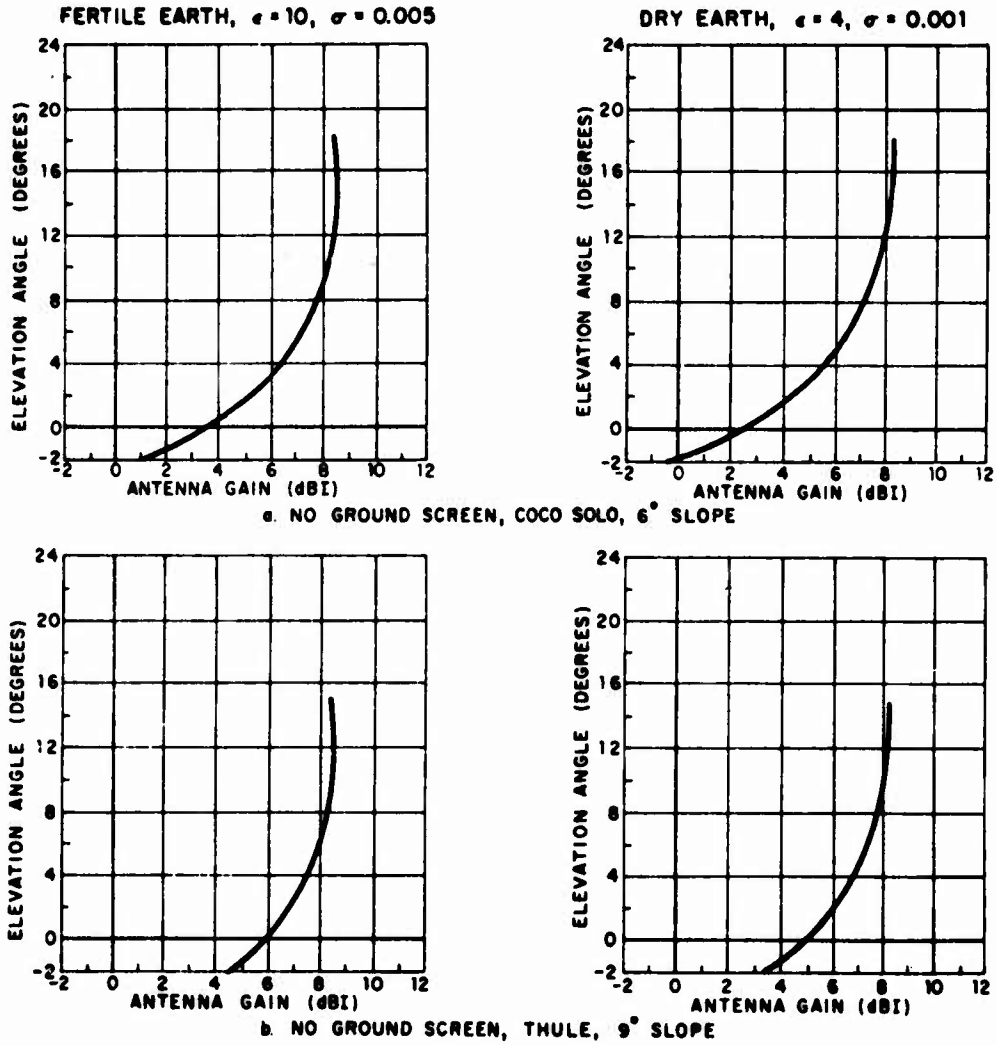

Figure 15. Computed Antenna Patterns Without Ground Screen, 30 MHz

ϵ = relative dielectric constant

σ = conductivity, mhos/m

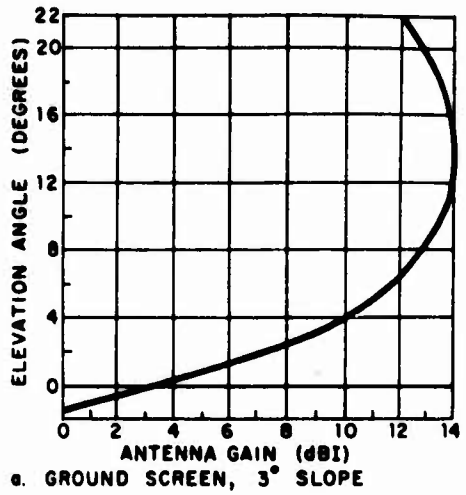

a. GROUND SCREEN, 3° SLOPE

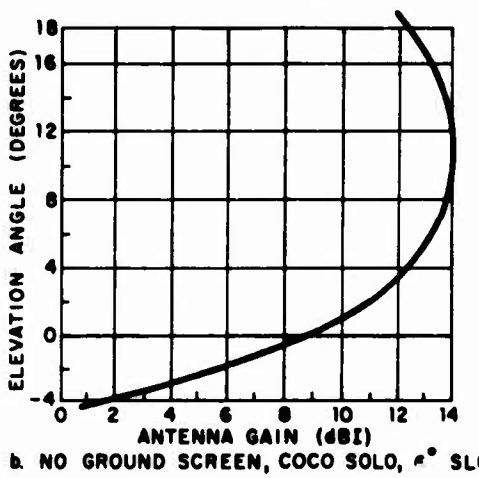

b. NO GROUND SCREEN, COCO SOLO, 0° SLOPE

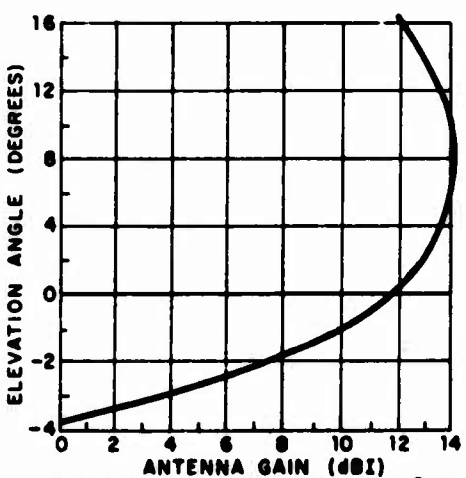

c. NO GROUND SCREEN, THULE, 9° SLOPE

Figure 16. Computed Antenna Patterns, Horizontal Polarization, Any Frequency, Smooth Earth

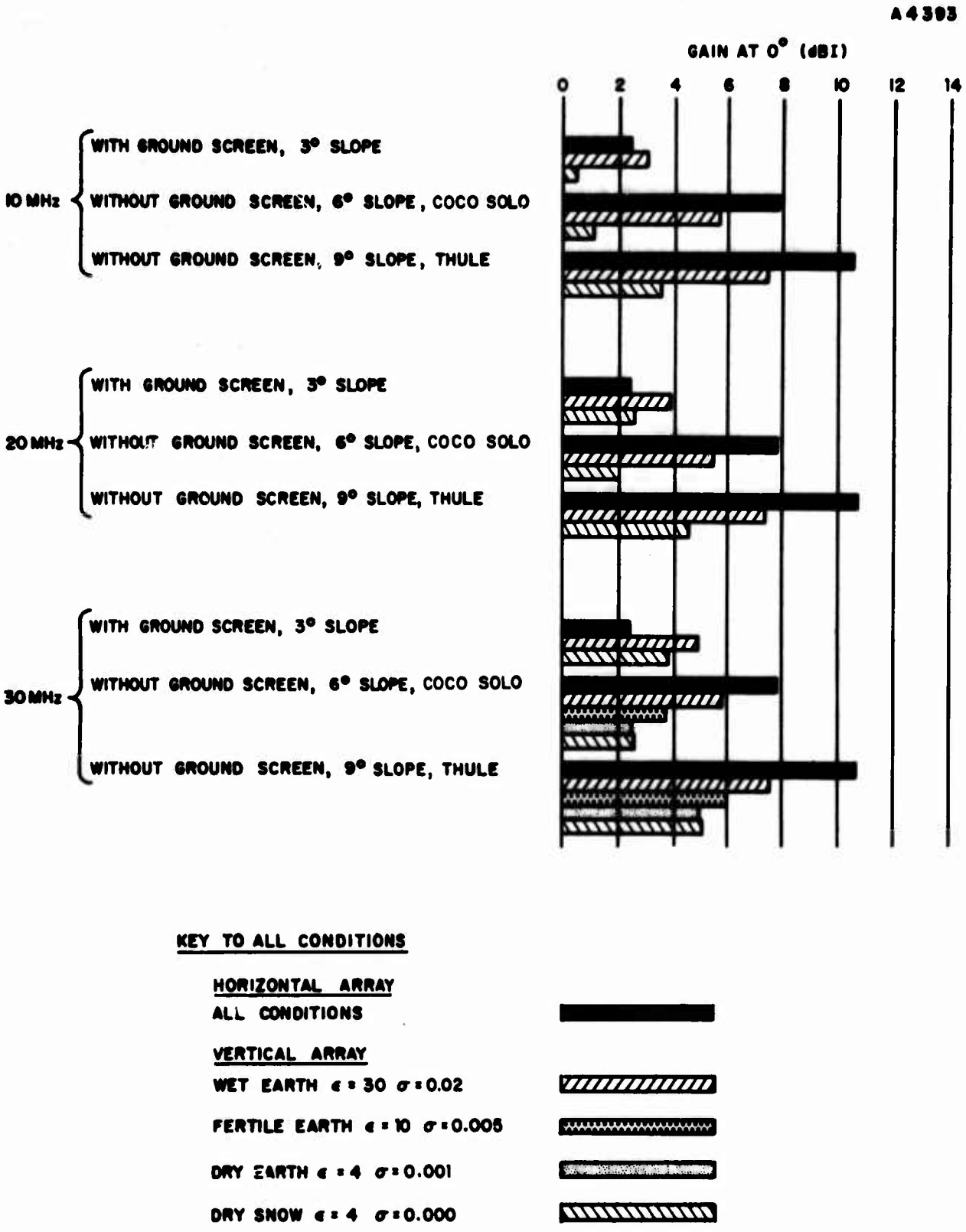

Figure 17. Comparison of Antenna Gains, 0° Elevation Angle

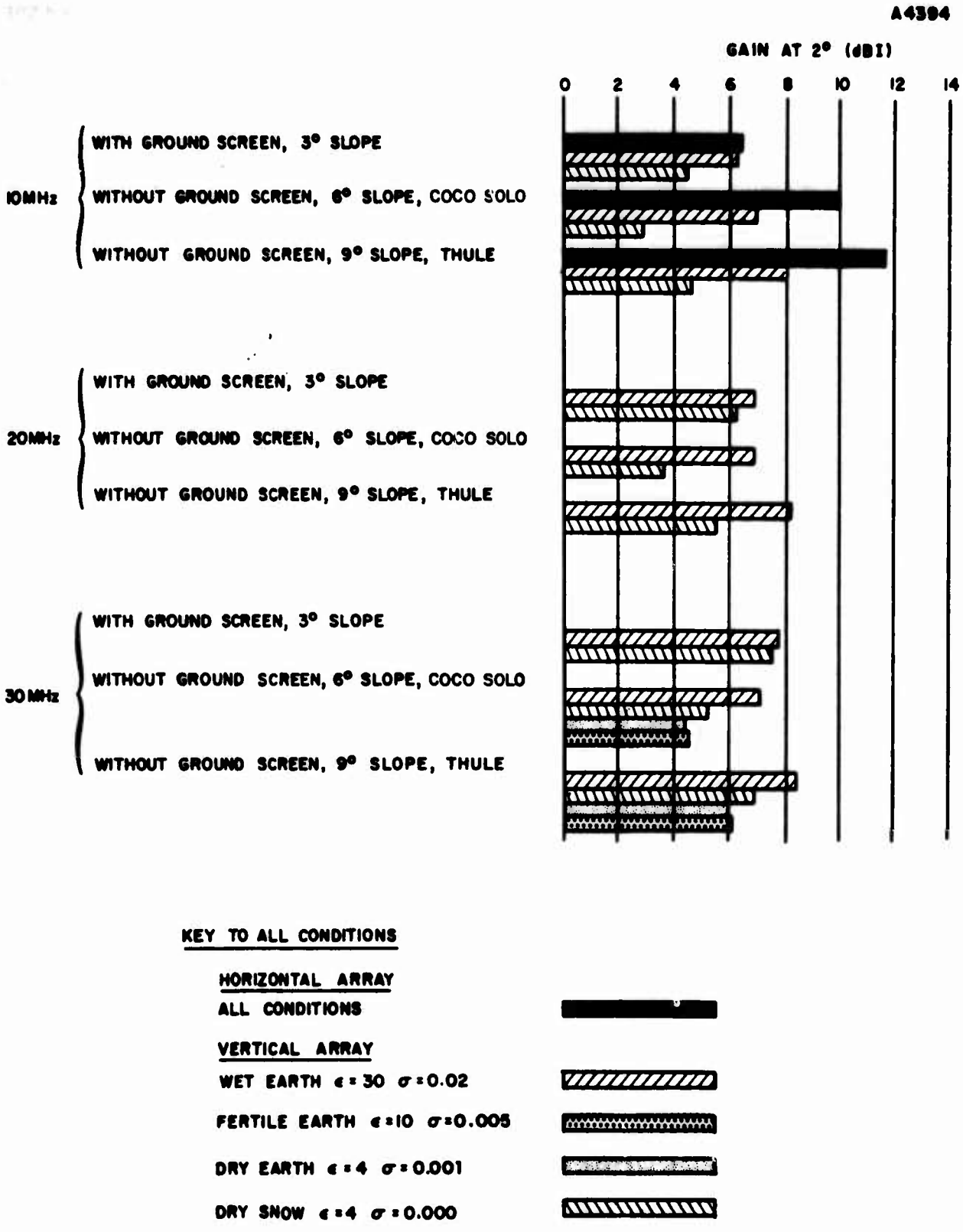

Figure 18. Comparison of Antenna Gains, 2° Elevation angle

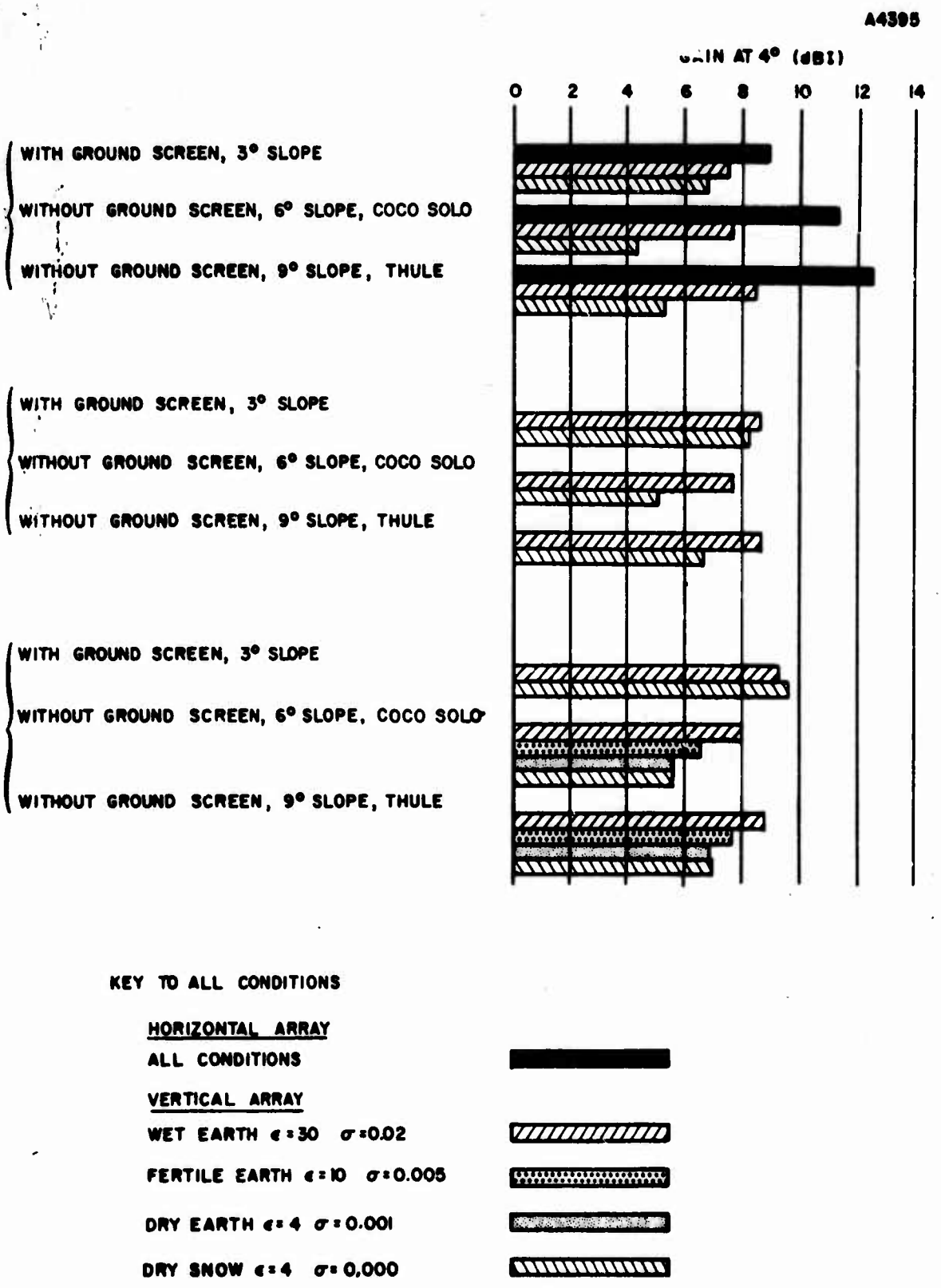

Figure 19. Comparison of Antenna Gains, 4° Elevation Angle

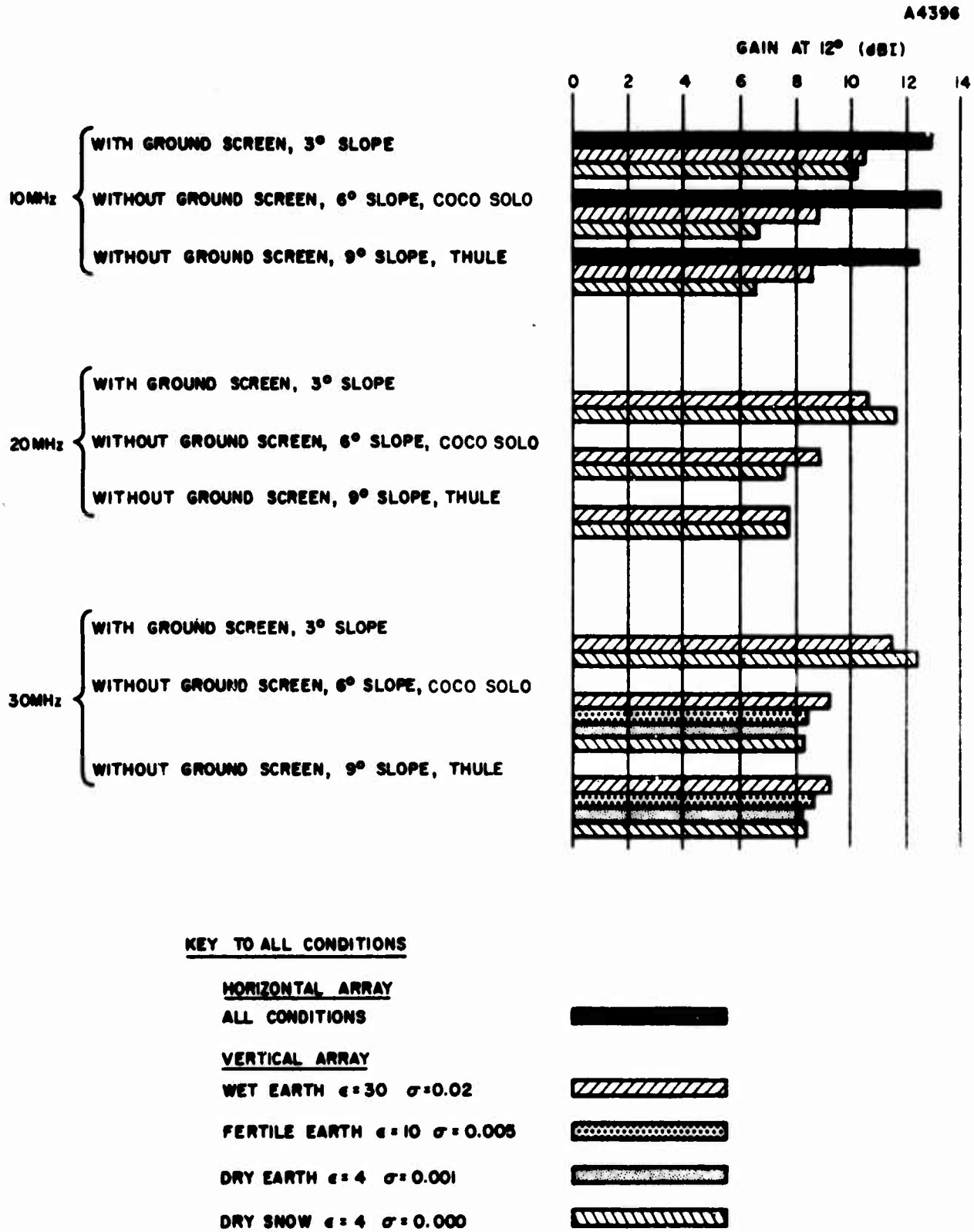

Figure 20. Comparison of Antenna Gains, 12° Elevation Angle

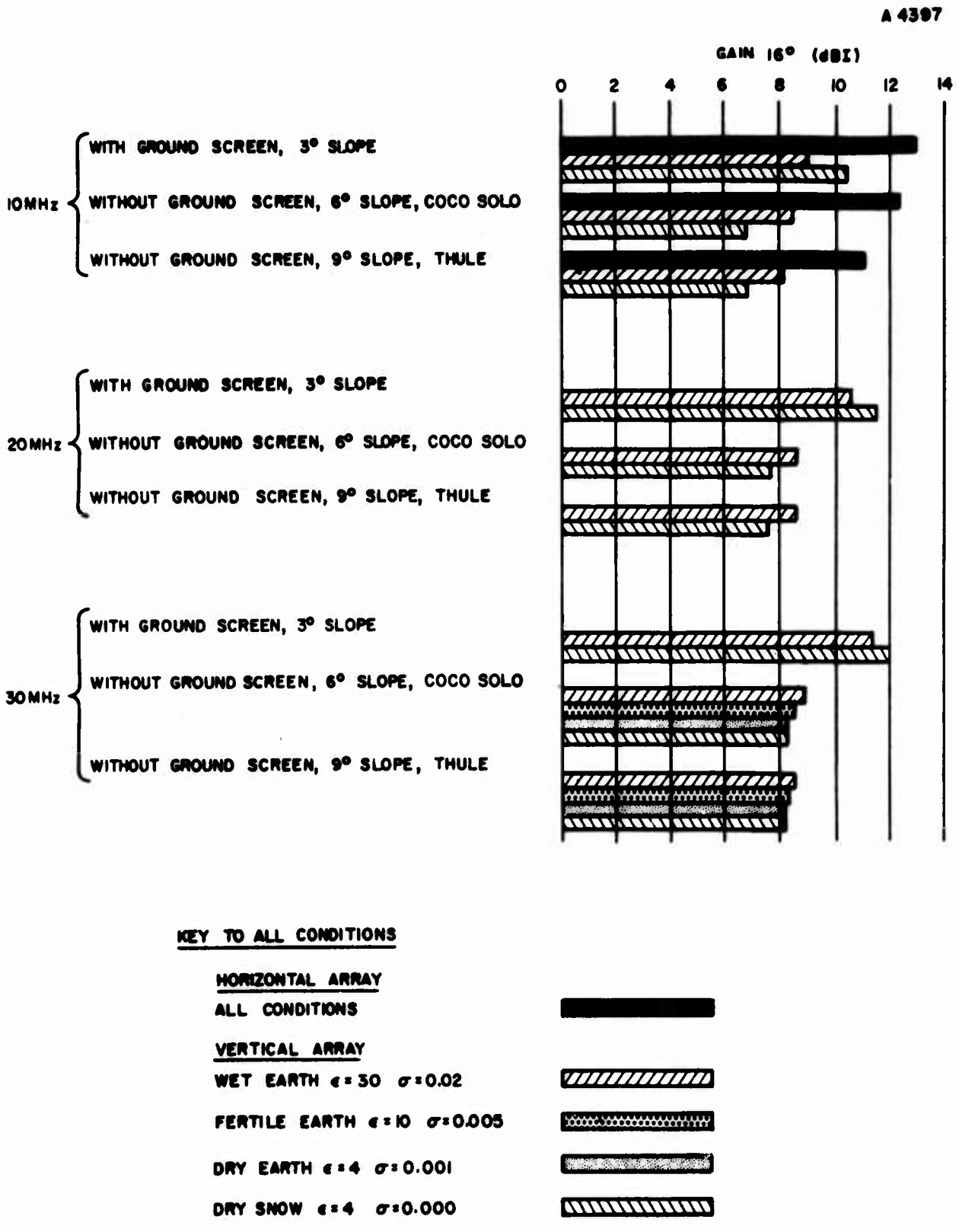

Figure 21. Comparison of Antenna Gains, 16° Elevation Angle

TABLE II

ELEVATION ANGLE OF ARRIVAL OF MAJOR MODES

Mode	Elevation Angle of Arrival (degrees)
1F2	0 to 4
2E	2 to 4
2F	12 to 20

The earth conditions around the antennas have a major effect on gain. The "wet earth" and "dry snow" conditions were selected to present extreme conditions with the various seasons. Data for the more probable "fertile earth" and "dry earth" conditions are included for 30 MHz. The variation of gain with earth condition depends upon frequency and elevation angle. At the lower frequency, the variation for the case with a ground screen is considerable, not only at the horizon but throughout the angles where the one-hop F2 (1F2) mode is expected. This results from the moderate size of the ground screen in wavelengths. The effects of ground are more severe without the ground screen, remaining important at all elevation angles and frequencies.

Various comparisons of gain can be made from the bar graphs. Typically, however, the horizontal antenna has 3 to 5 dB greater gain than the vertically polarized antenna without ground screen, even though both had the same nominal ideal-ground gain. This is the result of the ground losses in the direction where maximum gain occurs for the ideal vertical antenna: along the ground. The indicated changes in absolute gain are a result of slope; adequate gain exists in all cases.

The spread in gain with ground changes is maximum from wet to dry earth. The Starr Hill site turns to a bog under the antennas in the spring, but down-slope from the antennas the full wet-earth condition probably does not occur. Even during a drought, the soil probably does not dry to the "dry earth" condition. The maximum change probably occurs during the spring thaw, from dry snow in February to near "wet earth" in April. The possible range is near 6 dB; the probable range is perhaps nearer to 3 dB. No adequate measure is now available to permit assigning accurate values. The stabilizing effect of the ground screen is readily apparent.

The comparisons in Figures 17 through 21 can be misleading in terms of the low angle gain with the ground screen. While the ground screen under the antenna must have a 2.75° slope, that beyond the antenna can be made to conform to the slopes of the ground. The 3° mean slope selected may be shallow for both directions of antenna, and the gains indicated for the lower angles are correspondingly pessimistic. A more precise analysis has not been made, since the gains indicated are adequate, and the description of the screen shape requires major unjustified effort for a computation which would be of a much-simplified case.

A ground screen is considered desirable to reduce the variations in gain with season and weather, and to eliminate the ground resistive losses. The factors reviewed at the start of this section are the reasons no ground screen is being installed at this time.

c. RF Distribution Network

The outputs of the antennas are amplified, combined and divided to the several receivers in an RF distribution cabinet. The schematic of RF distribution circuitry appears in Figure 22.

The signals from the horizontally polarized antennas are preamplified, then power-divided. These antennas are the source of the receive signal for communications and can be connected as transmit antennas in the future should the Ava transmitters become unavailable. The necessary transfer relays have not been installed, nor is the necessary transmitter available at the time this report is prepared.

The signal from the vertical antennas are also preamplified, in phase- and amplitude-matched preamplifiers. The two vertical curtains in each direction are connected separately to the RF cabinet through lines matched in phase length to permit a comparison of the two outputs in an interferometer for azimuth of arrival measurements. The output from each preamplifier is split. One part from each split is combined to provide a "sum" signal to the noise/interference receiver. This minimizes the losses ahead of this receiver. The other part is further split. One signal from each side is supplied to the azimuth of arrival receiver. The remaining portions of the signals are combined to form a "sum" signal for either the mode loss receiver or the sounder receiver as selected by relays.

The figure shows the circuitry in detail. Much of the complexity provides flexibility to the noise/interference receiver and will be discussed with that equipment.

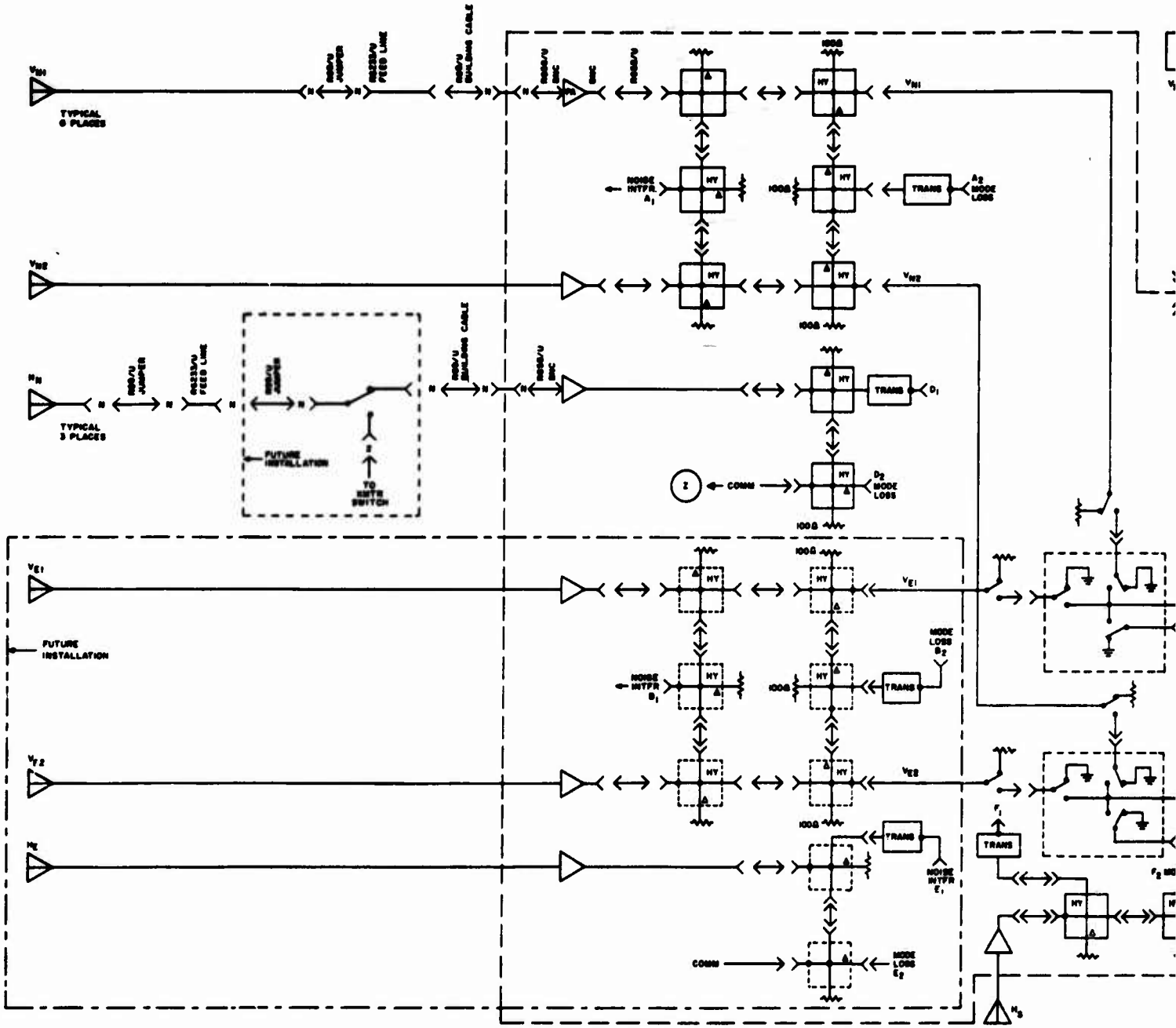
TYPICAL
6 PLACES
RG8/U
JUMPER
RG213/U
FEED LINE
RG8/U
BUILDING CABLE
RG8/U
BNC
BNC
RG58/U
100Ω
HY
TRANS
MODE
INTFR.
MODE
LOSS
TYPICAL
3 PLACES
FUTURE
INSTALLATION
TO
MATR
SWITCH
COMM
FUTURE
INSTALLATION

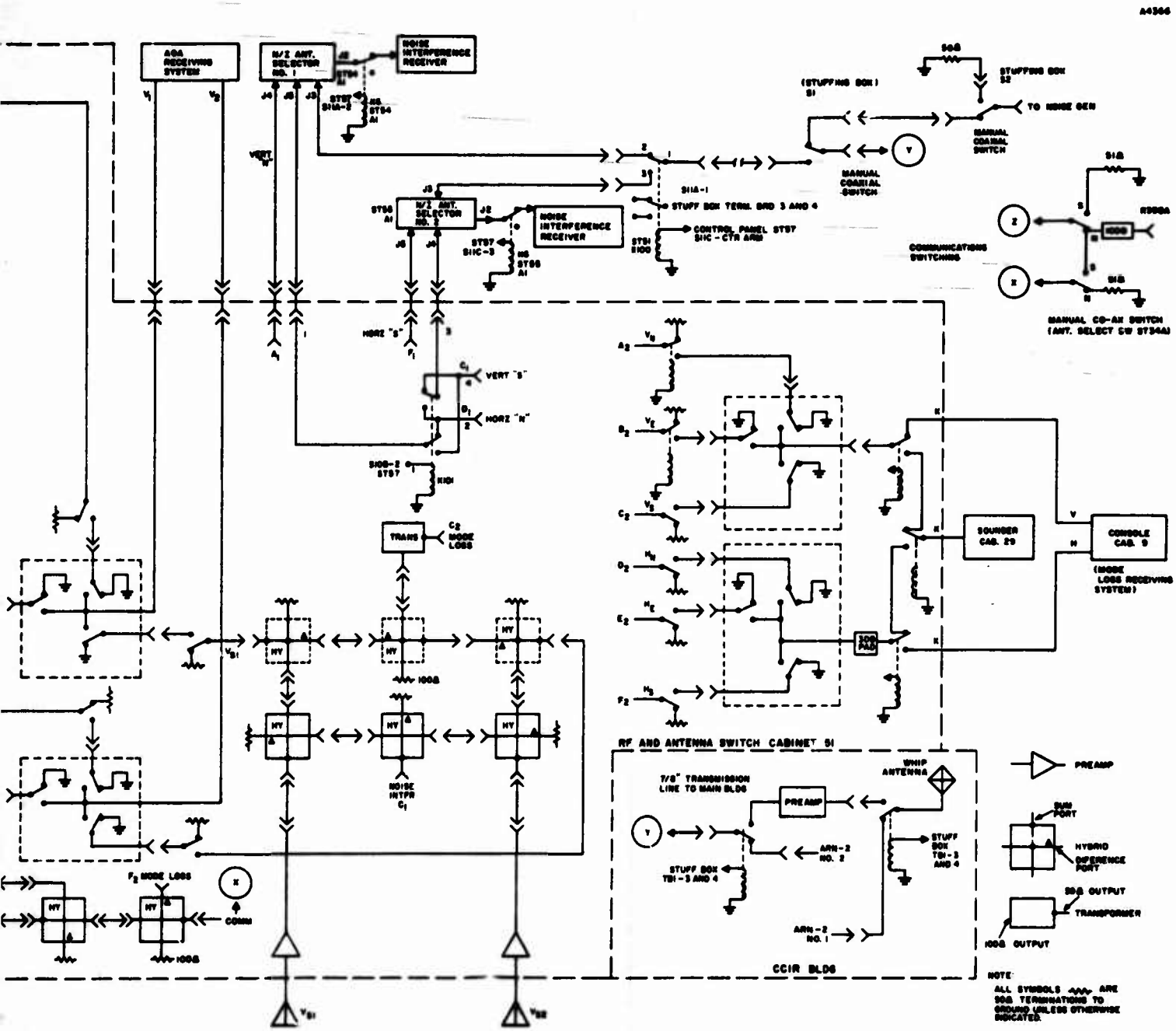

Figure 22. RF Distribution Network

2

2. ENVIRONMENTAL STUDIES SECTION

The results of the calibration flights flown in late August 1966 were reduced by the program group at RADC to individual run patterns, and then repeat patterns were averaged to produce mean measured patterns. A sample pattern is shown in Figure 23. A discussion of the data-taking appears in Section II-5.

The absolute gain was established through a complex series of steps effectively determining the calibration of the aircraft loop antenna. The inputs included near- and far-field ground calibration tests, flights against reference antennas, and an analysis of the measured patterns at both Coco Solo and Thule. The process of refining the calibration is continuing. The full process will be discussed, with the implications for accuracy, in a future report on antenna calibration when all steps have been completed and the final determination of the loop constant made.

The previous calibration of the horizontal antenna reported in Interim Report No. 4, Dispersive Characteristics of the Ionosphere, 30 June 1965, is the only data available for horizontal polarization. These data, too, are being examined for ways in which the uncertainty in gain can be reduced.

The horizontally polarized "V" antenna feed is open wire. The open wire was originally brought to a balun inside the building. To reduce the radiation from this line, which was affecting the sounder programmer, the balun was moved to the first transmission-line support tower, about 100 feet from the operating room. Coaxial line, available from the abandoned "delta" vertical sounding antenna, was moved to connect the balun to the switches in the operating room. The loss in this section of 7/8-inch heliax cable will not be significantly different from the open wire line loss, so no change in calibration data is required.

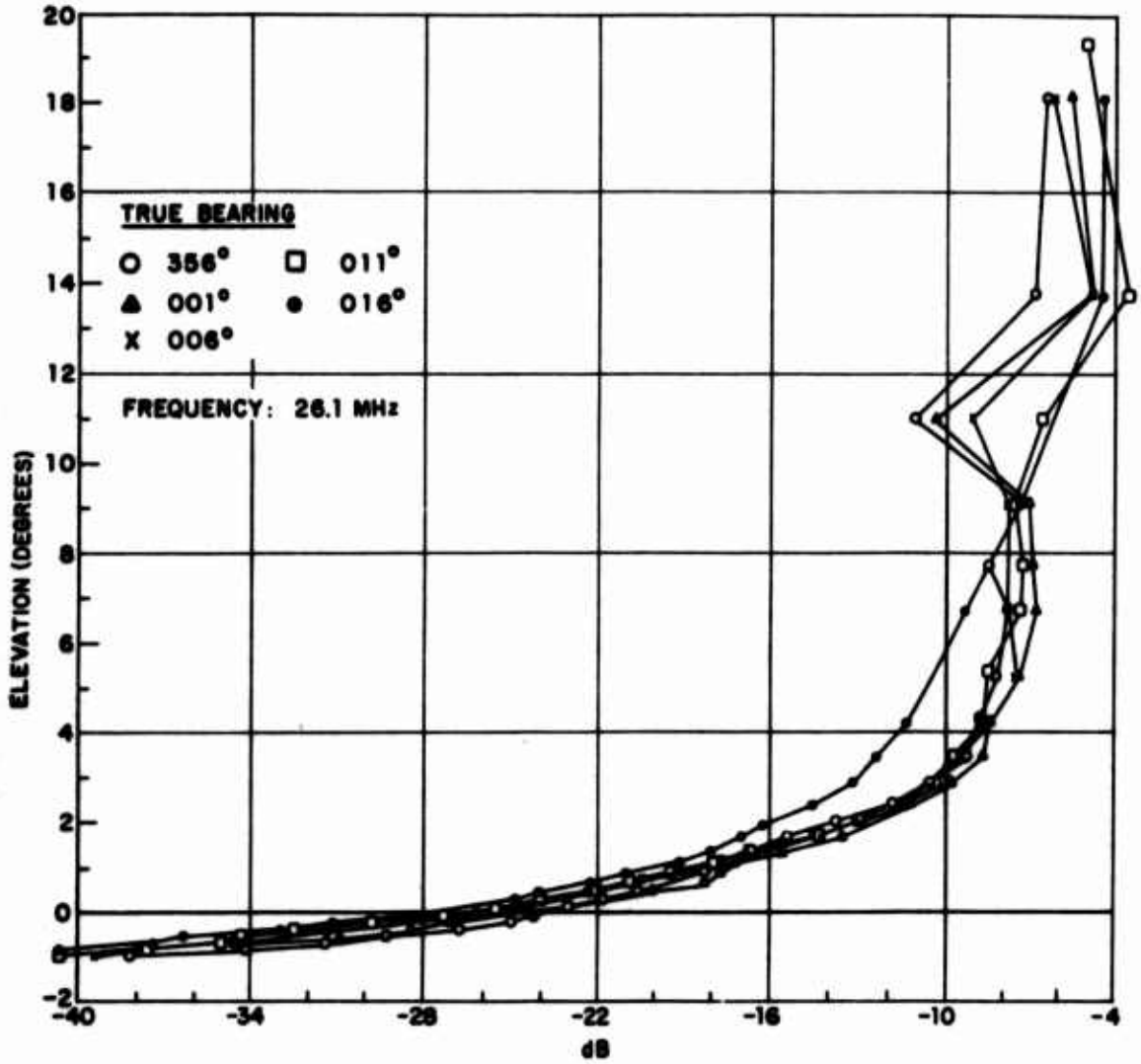

Figure 23. Averaged Antenna Patterns, Coco Solo LPV Antenna

3. THULE TRANSMITTER SITE

The antenna at Thule is located on a rocky point between the two troposcatter antenna installations on Pingorssuit mountain ("P" mountain). From this site there is an unobstructed path south, with the horizon being Baffin Bay 2600 feet below. From 2600 feet, the dip angle to the horizon is about 1°. The antenna and mountain-top complex appear in Figure 24; the view to the bay in Figure 25.

Because the site is exposed, weather conditions have been more severe than reported and far more severe than the design conditions for the Granger 726-5 antenna (see Table III).

TABLE III

SPECIFICATIONS FOR GRANGER MODEL 726-5 ANTENNA

Parameter	Specification
Frequency range	4 to 64 MHz
Application	Receive and transmit
Power capacity	1 kW average, 30 kW PEP
Input impedance	50 ohms coaxial
VSWR	Compatible with G/A sounder transmitter
Level of largest side or backlobe relative to mainlobe	-14 dB 4.4 to 64 MHz, -10 dB below 4.4 MHz
Connector	LC type, female
Approximate shipping weight	4390 pounds
Polarization	Vertical
Directive gain, relative to isotropic, above perfect ground	Greater than 10 dB
Azimuth beamwidth between half-power points	110° nominal
Permissible wind and ice	120 mph wind, no ice 100 mph wind, one-half radial ice

The antenna had been installed at Camp Tuto for about five years before being furnished to this program. Despite the previous fatigue factors and the severe weather encountered, only minor damage was done to the antenna through the winter and spring season. An example of the antenna damage is shown in Figure 26.

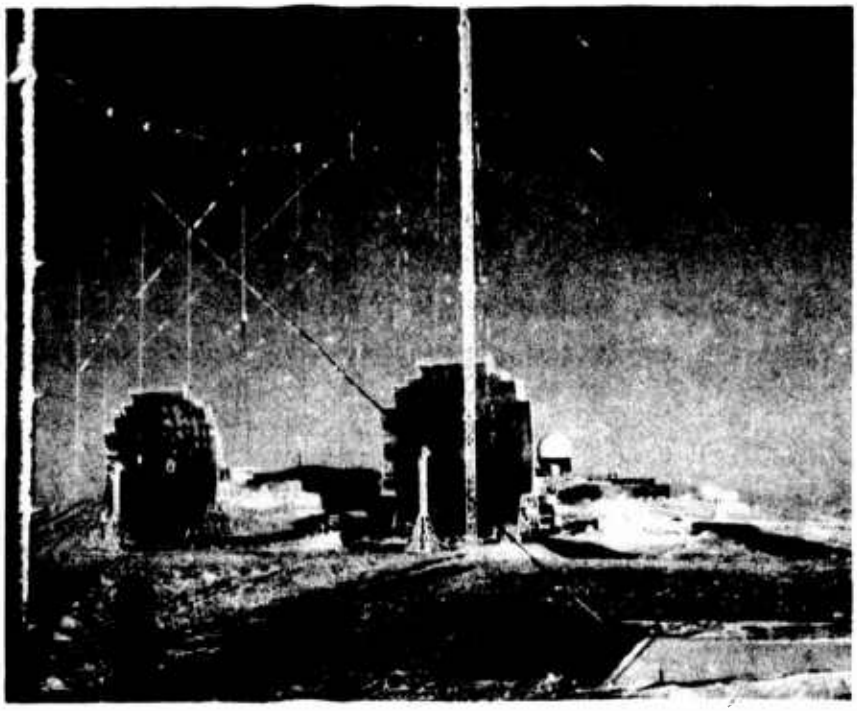

Figure 24. "P" Mountain, Thule Site and Antenna

Figure 25. Looking Toward Starr Hill from Thule Antenna

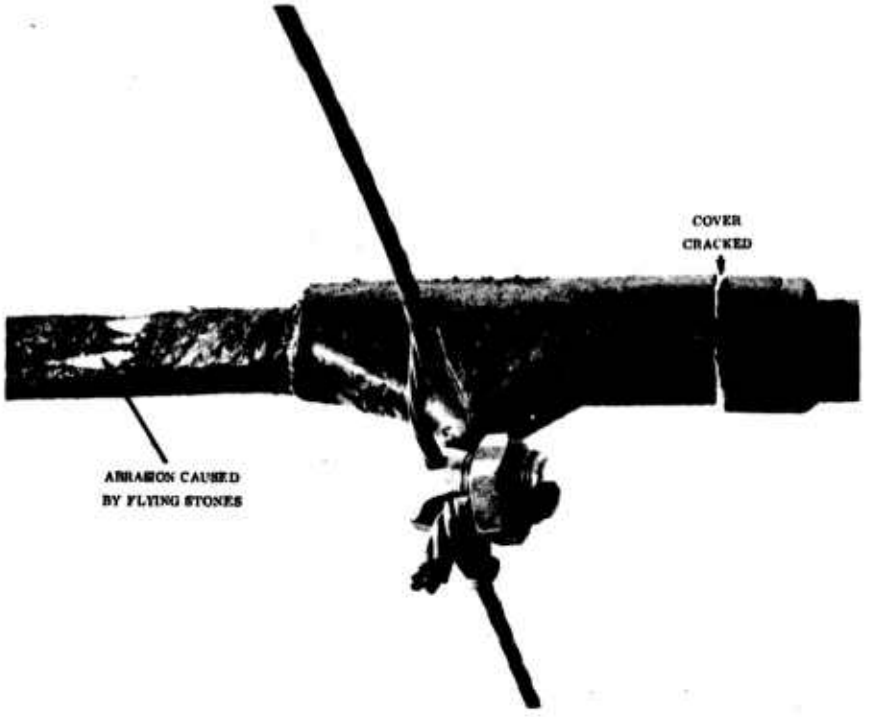

Figure 26. Feedline Damage on Thule Antenna

The antenna site layout drawing appears in Figure 27. The Granger 726-5 antenna was installed as shown. A wire antenna was run to the wood pole for communication monitoring.

Calibration flights were made during the last two weeks of October to obtain gain data on the antenna. Four transmitters on the ground were keyed in sequence to permit the pattern to be measured on four frequencies on each aircraft run. A typical partially reduced pattern appears in Figure 28.

Lobing caused by reflections from Baffin Bay is very apparent. The reduction of the pattern data to computer input will be covered fully in the final report as noted elsewhere.

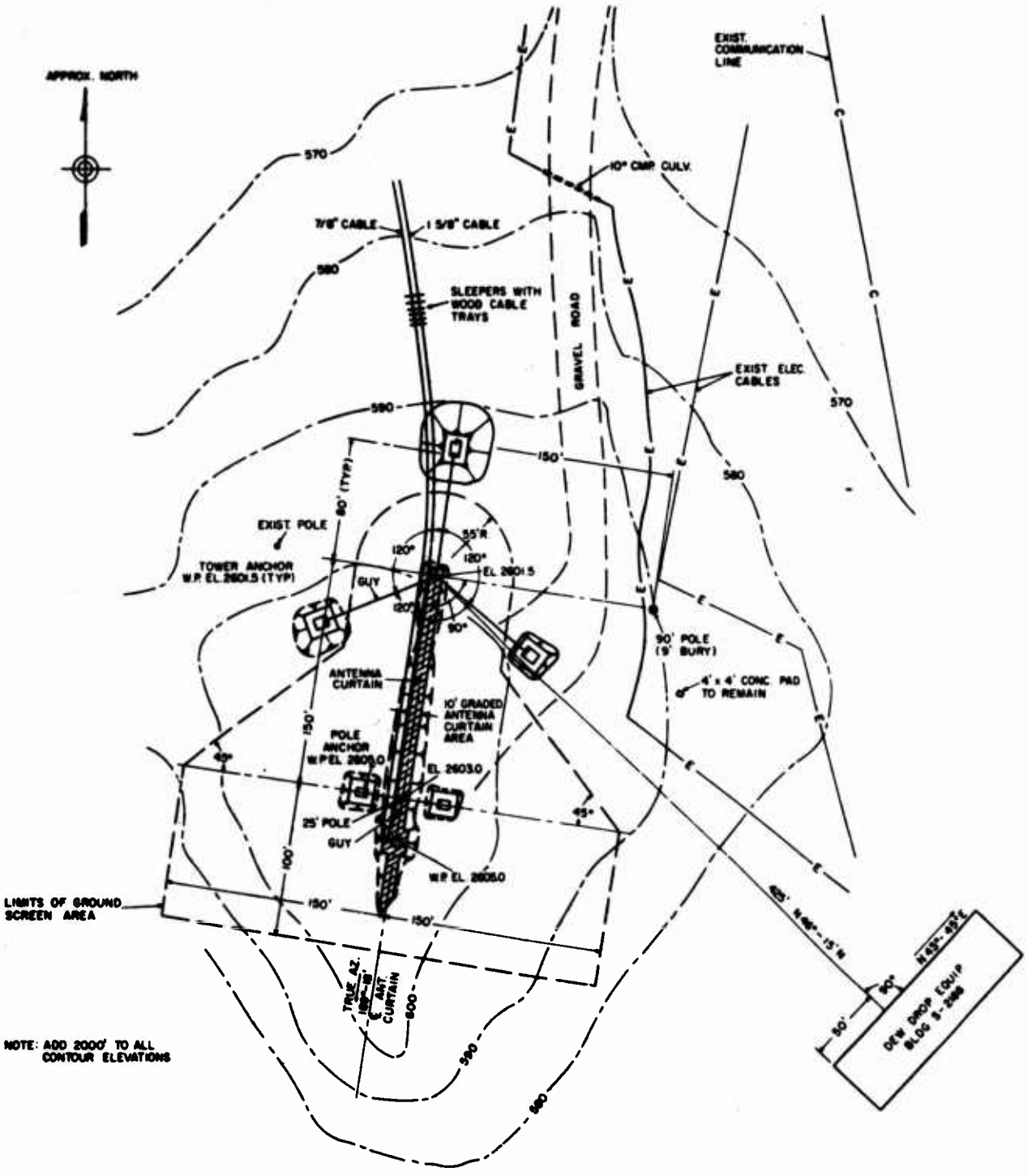

Figure 27.. Antenna Site Plan, Thule

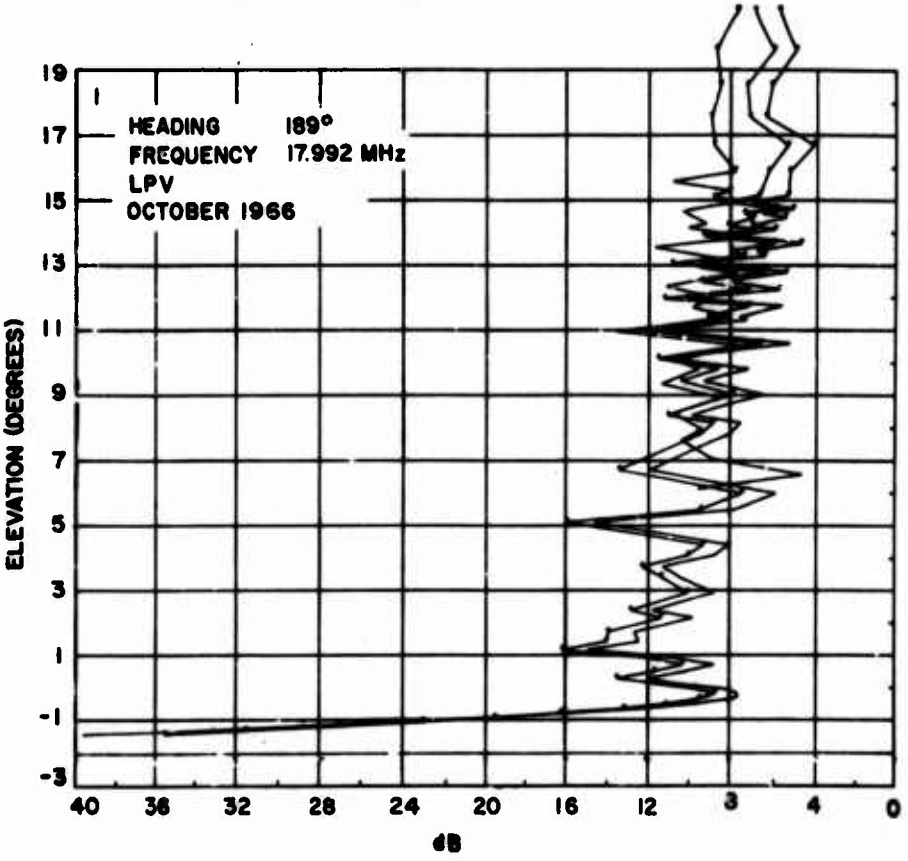

Figure 28. Sample Thule Antenna Pattern

4. KEFLAVIK TRANSMITTER SITE

Space has been obtained at the "Dye 5" site at Keflavik, Iceland, for an eastern site. The area includes both troposcatter and Navy HF communications facilities. The troposcatter antennas are the most prominent feature in Figure 29.

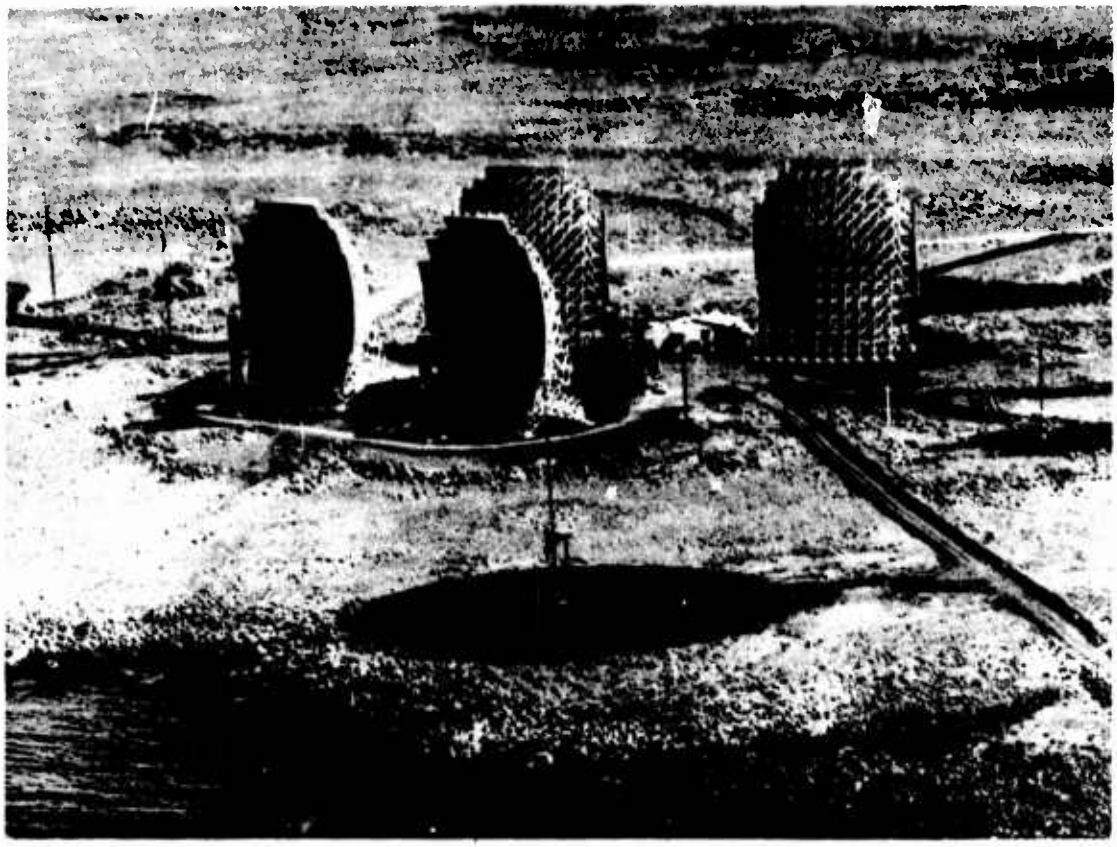

Figure 29. Keflavik Site Before Construction

The vertical antenna close to the water, on the circular graded area, is to be removed. This will be the location of the antennas for the Little IDA program. The equipment will be installed in the building behind the nearest troposcatter reflector. An artistis concept of the installation is shown in Figure 30. The antenna is the same type as installed at Thule: a Granger LPV 726-5 log periodic monopole. A communications monitoring antenna and a Collins Loran C 32-foot whip antenna will also be installed.

While the site equipment is like that at the Thule site, the location is a seaside site as at Coco Solo, and the antenna patterns should be similar. Calibration of the antennas is planned for the period shortly after the site is installed, now estimated to be in the fall of 1967.

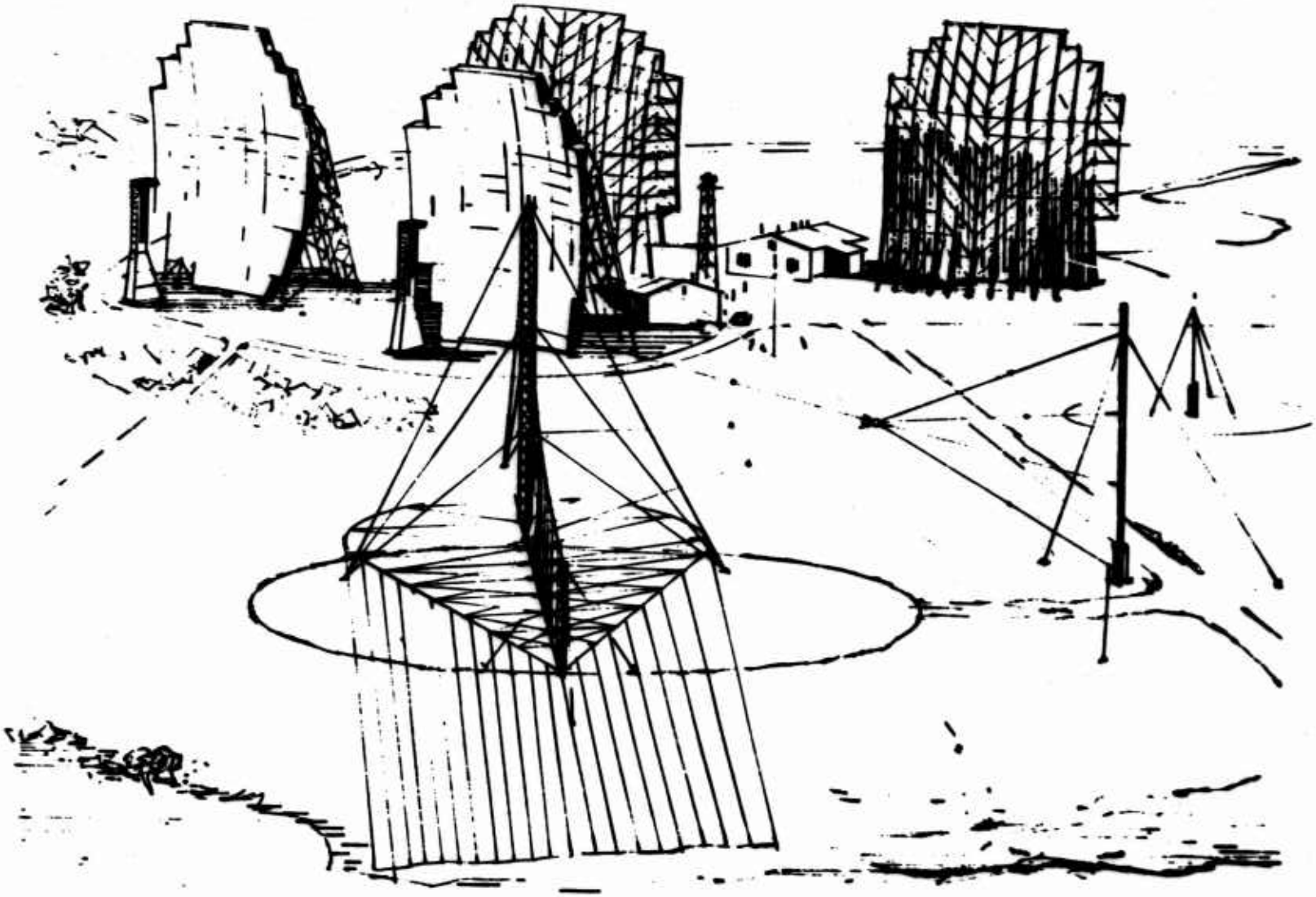

Figure 30. Artist's Concept of Keflavik Site

5. ANTENNA CALIBRATIONS

Data for the calibration of both the Coco Solo and the Thule antennas were taken by transmitting from the ground antennas and receiving on a jet aircraft flying at 30,000 feet. The aircraft was a KC-135, number 3125, with a loop antenna mounted on a modified refueling boom.

The aircraft was equipped with four receivers, type R-390, and light-beam-galvanometer recorders. Equipment to establish the calibration of the receivers in amplitude, and to adjust signal levels was also installed. The automatic gain control voltage, which is nearly logarithmic (equivalent to linear in dB) with signal input level, was recorded. Distance from the site was manually entered on the charts. From the altitude and distance the elevation angle of a point on the record could be determined; the track of the aircraft determined the azimuth. With this equipment, pattern data could be obtained for four frequencies on each outbound radial of the aircraft. To obtain data to about 1° below the horizon, each radial was about 300 nmi long.

The ground equipment included frequency synthesizers to establish frequencies, a combination of available transmitters, and a sequence keyer. At Coco Solo, two Collins KWM-2 plus 30-L-1 transmitters (self-controlled in frequency), a Viking Thunderbolt driven by the Phantom exciter, and a GPT-750 were employed. At Thule, the equipment included two KWM-2 plus 30-L-1 equipments, the station Gates HFL-3000, and a General Electric owned Globe Sidebander-Viking Thunderbolt chain, all synthesizer controlled. The sequence keyer connected each transmitter to the antenna in sequence for one second, and turned it on while it was connected. Thus, four frequencies were transmitted in four seconds. Power monitoring was by oscilloscope connected to a Sierra type 645A directional coupler. Power meters, and meter-type RF voltmeters do not have the speed of response required for one-second pulses.

The pulsing rate of one second on, three seconds off, provided adequate sampling of the antenna pattern, permitted four-frequency operation without complex and expensive multicouplers, and allowed the interference level to be checked. The trace was distinctive and readily identifiable by the receiver operators.

Data reduction was a combination manual and computer operation. The received signal levels and distance were manually read from the flight records. The transmitted power level was calculated. The values were entered into a computer which calculated points and prepared both printed output and a computer-drawn curve as shown in Figure 28. A

further averaging of repeated flights was computer made. The Coco Solo data shown in Figure 23 are such a plot for five different azimuths.

The pulsing technique worked very well. A one-second on period permitted the standard equipment to respond fully. The data rate was adequate for the patterns required, to about 25° elevation angle. The ability to measure the noise and interference level permitted the analysis of some data which would otherwise have been unusable. It also reduced the duty cycle on the transmitters.

The data taken in these flights will be reduced to a form convenient for computer reduction of the propagation data. This will be described in a later report.

SECTION III

NOISE/INTERFERENCE RECEIVING SYSTEM

This section reports the instrumentation progress during the preceding reporting period and the present status of the noise/interference (N/I) receiving system which is comprised of the cross-polarized antennas, RF distribution network, and the N/I receiver, all of which are located at Starr Hill, New York. Included in the N/I receiving system proper is the ESSA radio noise recording station which is operationally integrated with the N/I receiver and antennas.

1. SUMMARY

a. Noise/Interference Receiver

The N/I receiver was delivered to the Starr Hill site on 1 May 1967. Installation and interface connections were completed on 9 May; i.e., "power on."

The on-site checkout, which consisted of operational and electrical performance verification, has been satisfactorily completed with the exception of checkout of the CCIR operating mode and the checkout of antenna multiplexing mode.* These two remaining checkout tasks are scheduled as soon as the digital processor is available for these tasks. The results of the electrical performance verification are incorporated into the summary of the N/I receiving system electrical performance.

The most significant development problem which arose during the reporting period concerned local oscillator (LO) noise transfer in the receiver mixers. (A detailed discussion of this problem is contained in Appendix I.) An interim solution of this problem (Phase I) was effected which uses a manually tuned narrowband LO power amplifier. An automatically tuned LO consisting of a broadband LO amplifier and remotely selected narrowband bandpass filter is being designed and fabricated for later delivery (Phase II). The N/I receiver, as delivered, incorporates the Phase I capability. Design analysis and development of components for implementing the Phase II capability was initiated in June.

A data recording capability using six channels of a Sanborn recorder has been implemented to provide a data collection capability while the digital processor is being checked out.

---

* Third Interim Report, Table XI.

b. RF Distribution Network and Antennas

Measurements pertaining to the calibration of the RF distribution network have been made. The results are incorporated in the system electrical performance discussion.

Antenna efficiency measurements remain to be obtained.

The installation of switching relays and RF cables associated with the rewiring of the antenna selection switches have been accomplished during the reporting period.

c. ESSA Radio Noise Recording Station

One of the two ARN-2 noise receivers (the receiver connected to the whip antenna) became operational in February. The second ARN-2 receiver is utilized for data collection with the directional cross-polarized antennas. On 15 May this receiver was placed in operational status with a specified antenna connection schedule. Calibration of this ARN-2 to refer noise data to kT_oB has been completed with the exception of the antenna efficiency factor.

2. SYSTEM ELECTRICAL PERFORMANCE

a. System Representation

For purposes of discussing system electrical performance, the N/I receiving system may be considered to consist of the RF distribution network (Figure 31) and the N/I receiver.

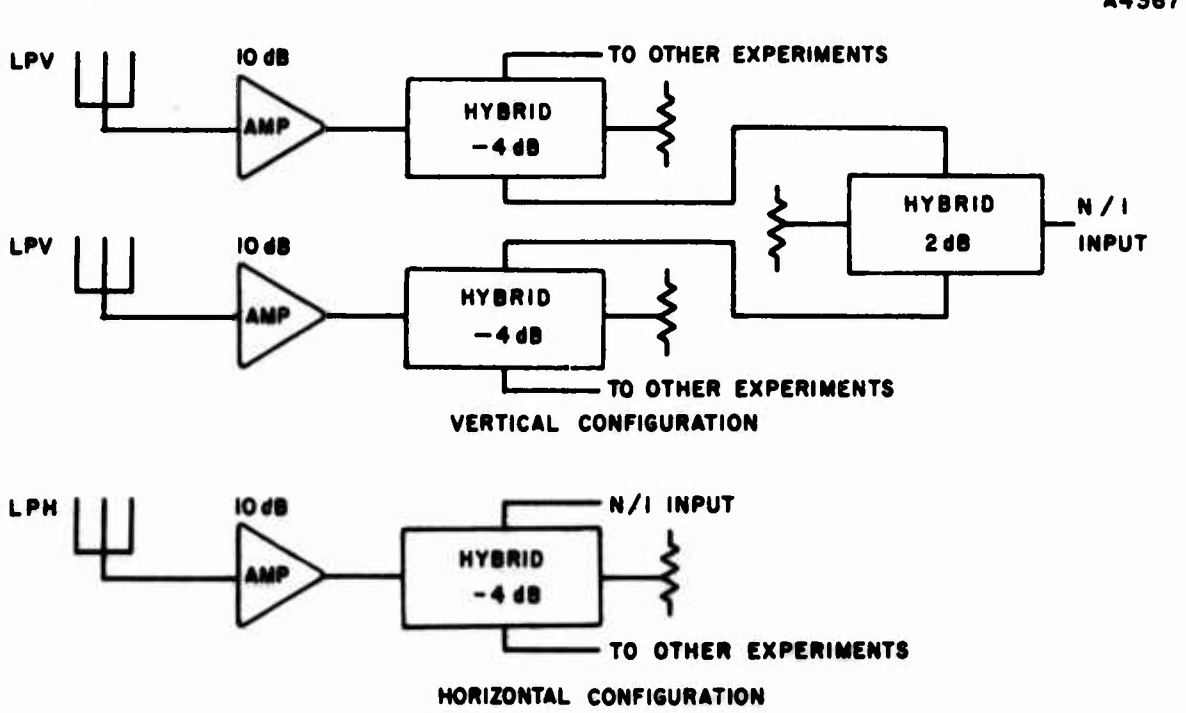

Figure 31. RF Distribution Network

The effect of the preamplification stage is to enhance the system noise figure performance at the sacrifice of some intermodulation performance, a sacrifice which will be shown to be imperceptible.

b. Performance Summary

The N/I receiving system performance is presented in Table IV, which compares the design objectives with measured performance.

TABLE IV

N/I RECEIVING SYSTEM ELECTRICAL PERFORMANCE

Parameter	Nominal Design Objectives	Measured Performance
Front-end dynamic range		
Inter/cross-modulation products from two 10-mV rms input signals (CW or 100 percent AM) shall produce		
Second-order intermodulation	< -89 dB	< -94 dB
Third-order intermodulation	< -103 dB	< -100 dB,* -124 dB**
Third-order cross-modulation	< -103 dB	< -104 dB
Linear operating range	>120 dB	>120 dB
Noise figure	< 10 dB nominal	< 12.7 dB nominal
Image rejection	< -80 dB	< -90 dB
IF rejection	< -80 dB	< -90 dB
Input impedance	50 ohms	50 ohms
Second IF linearity (over a 40-dB amplitude range)	±1.5 dB	±0.5 dB

* Two in-RF band signals.
** Two out-of-RF band signals.

The receiving system inter/cross-modulation performance, which is a measure of linearity over the dynamic range, is generally superior to the design objectives. The second-order intermodulation products for in- and out-of-band signals are, respectively, 3 dB above and 21 dB below design objectives. The use of preamplification before RF filtering increased the undesired intermodulation products, but improved the receiver noise figure and, hence, is felt to be worthwhile. The final measured in-RF band third-order intermodulation performance, which is 3 dB above the design objective, is felt to be insignificant in terms of the experiment.

The cross-modulation products are at least 6 dB lower than the intermodulation products depending on the exact modulation and are at least 3 dB superior to design objectives.

The receiving system linear operating range remains in excess of 120 dB. From preliminary data collected from the "live environment," this operating range appears to be quite satisfactory.

By the incorporation of RF preamplification prior to the N/I receiver, the 16.5-dB noise figure of the basic receiver is improved to a 12.7-dB noise figure for the overall N/I receiving system. This system value for the noise figure appears adequate based on "live" observations. Preliminary data collected indicate that the ambient noise and interference levels are sufficiently high to mask the receiving system noise.

The remaining parameters are more applicable to the receiver only and generally indicate that the performance meets or exceeds the design objectives.

3. ELECTRICAL DESIGN OF N/I RECEIVING SYSTEM

a. Antenna Selection Switch Modification

The function and selection of the antenna selection switches were modified to improve overall receiving system noise figure. A summary of the changes is given in Table V.

TABLE V

ANTENNA SELECTION SWITCH MODIFICATION

Old Designation	New Designation
Antenna Channel 1 H V MX CAL CCIR 50	Antenna Channel 1 VN VS or HN MX CAL CCIR 50
Antenna Channel 2 H V MX CAL CCIR 50	Antenna Channel 2 VS or HN HS MX CAL CCIR 50
Site Selection Channel 1 E N S	Antenna Control VS on CH 1; HN on CH 2 HN on CH 1; VS on CH 2 Unused
Site Selection Channel 2 E N S	Receiver Selection Normal (FE1-GE2) Unattended 1 (ARN GE-2) Unattended 2 (GE-1 ARN)

b. RF Distribution

The RF energy is coupled from the antennas to the N/I receiver by means of passive hybrids and amplifiers. Figure 31 depicts the configuration. The predicted gains and losses of the individual components are indicated.

The measured values of the transmission gain from the antennas bulkhead connections compare favorably with the predicted values. They are:

Antenna	Gain (dB)
VN	7.64
HN	5.20
VS	7.32
HS	5.60

The transmission lines connecting the building with the antennas contribute the losses given below:

Antenna	Loss (dB)
VN	1.74
HN	1.20
VS	2.19
HS	1.68

The average gain of the six preamplifiers used is plotted versus frequency in Figure 32.

c. Noise/Interference Receiver

Tests performed on the N/I receiver alone during the reporting period that pertain to the N/I receiving system were the gain measurement variation as a function of frequency and the spurious response measurement. Results of the gain measurement are presented in Figure 33. As can be seen, both receiver channels have essentially the same gain characteristics in the high, medium, and low gain banks. The gain droop with increasing frequency is corrected in the data reduction computer programs.

The existence of internally generated spurious signals could corrupt the N/I data if there are several, large magnitude such signals. Fortunately, as summarized in Table VI, only one or two exist in any 1-MHz band.

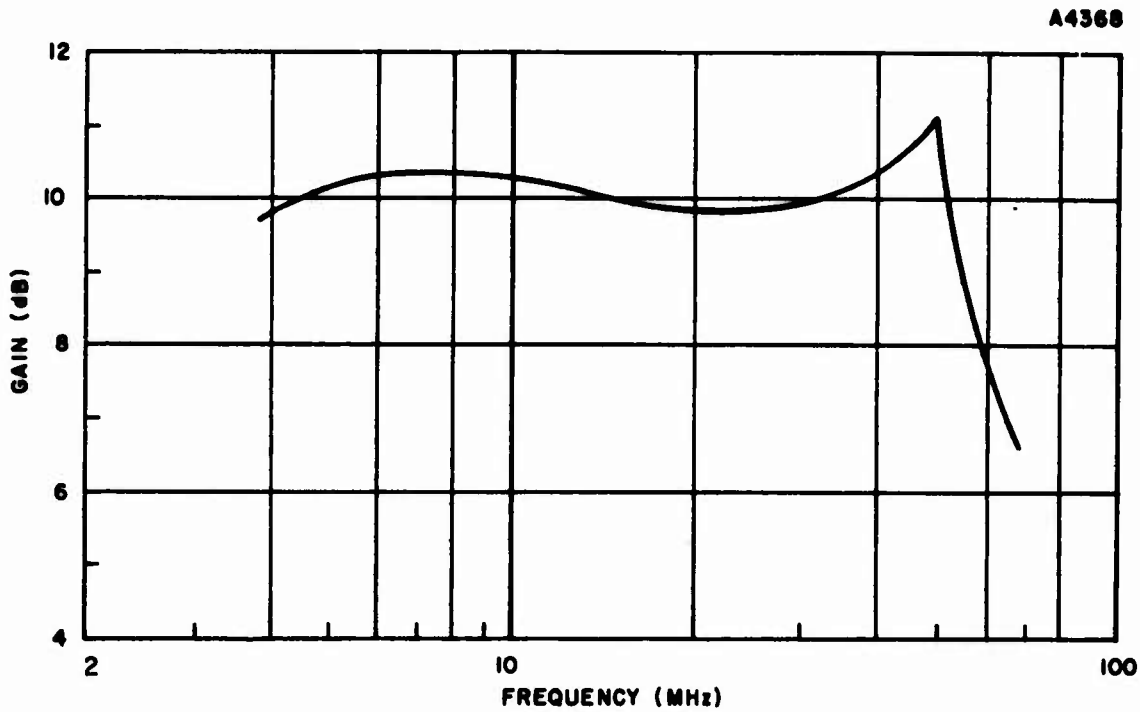

Figure 32. Average Transmission Gain, Starr Hill Preamplifiers

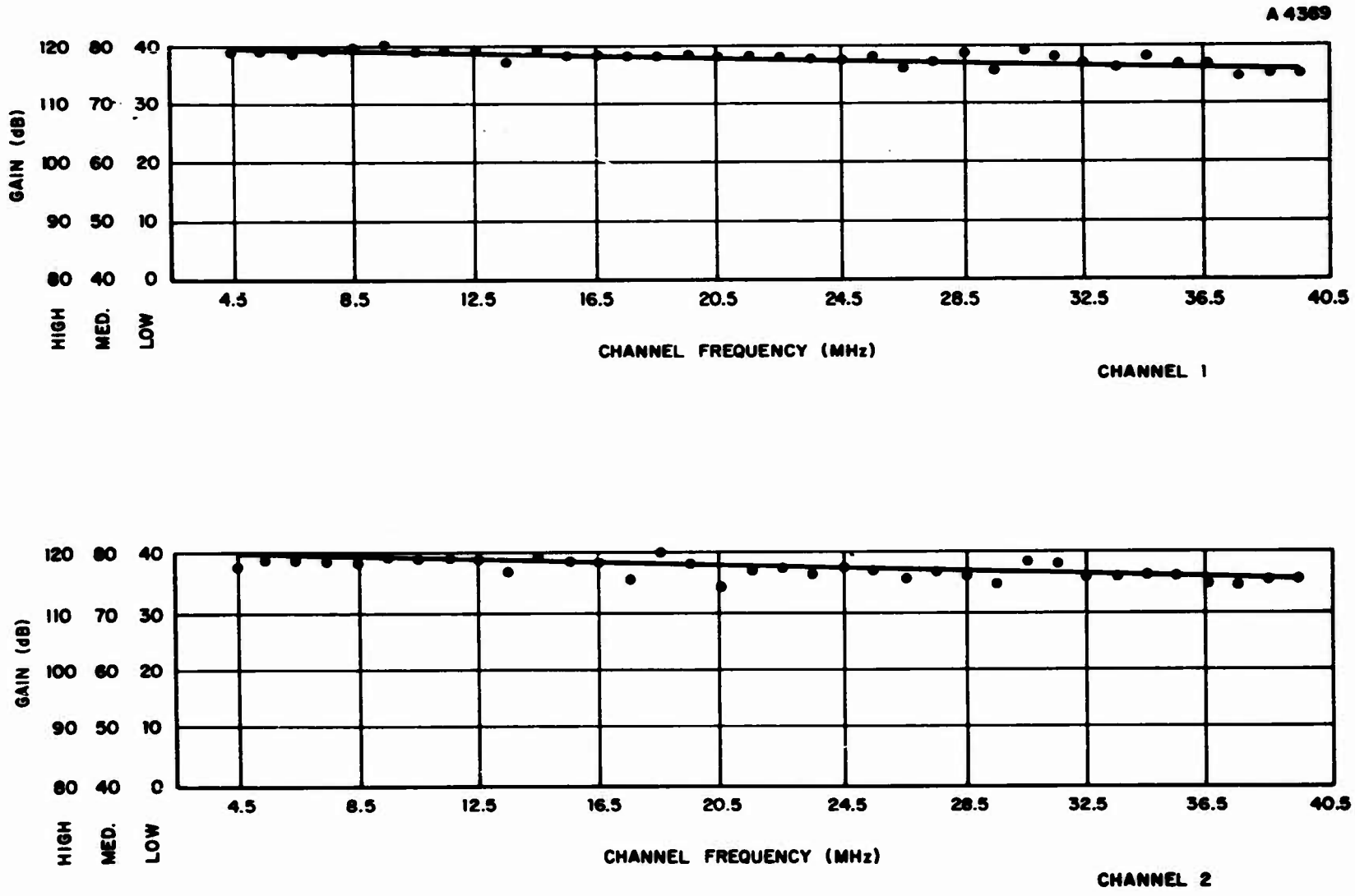

Figure 33. Noise/Interference Receiver Gain vs. Frequency

TABLE VI

RECEIVER SPURIOUS FREQUENCIES

RF Band (MHz)	Spurious Frequency (MHz)	Spurious Amplitude (dB re receiver floor level)
4-5	This band not measured	
5-6		
6-7	6.000	20
7-8		
8-9	8.124	5
	8.816	5
9-10		
10-11	10.000	38
	10.500	4
11-12		
12-13	12.500	7
13-14		
14-15		
15-16		
16-17		
17-18	17.692	4
18-19	18.000	36
	18.500	3
19-20		
20-21	20.000	27
	20.500	25
21-22		
22-23		
23-24		
24-25	This band not measured	
25-26		
26-27	26.500	9
27-28		
28-29		
29-30		
30-31	30.000	18
31-32		
32-33	32.000	47
33-34		
34-35	This band not measured	
35-36	This band not measured	
36-37		
37-38	37.500	3
38-39		
39-40	39.500	8

SECTION IV

MODE PROCESSOR

1. INTRODUCTION

The purpose of the mode processor is to convert the mode loss Phantom receiver outputs and the azimuth-of-arrival outputs into an analog form appropriate for processing by the digital processor or the drum processor (Figure 34). The following inputs are supplied to this equipment: (1) mode loss Phantom receiver video output containing horizontal and vertical polarized signals time multiplexed in alternate 5-ms intervals, (2) mode loss Phantom receiver 25-Hz output multiplexed in the same manner, (3) azimuth-of-arrival outputs (channel A and channel B), and (4) a prf trigger. In the 5-ms interval during which the horizontal polarization is present, four samples are taken of the mode loss video output and the azimuth of arrival. Since the drum processor has only two channels, only two samples are taken of the mode loss 25-Hz output. Each sample is 10 μs long and the relative position of the sample can be varied by the timing equipment from 20 μs to 5 ms after the prf trigger. During the vertical polarization 5-ms interval, only the mode loss video output is sampled. This sample occurs in the same relative positions within the 5-ms period as the horizontal samples. The azimuth of arrival contains no new information during this time. Each sample is peak detected with a dynamic range of 40 dB and stored in a boxcar circuit.

2. THEORY OF OPERATION

a. Subsystem Description

The overall block diagrams of the mode processor are shown in Figures 35, 36, and 37.

(1) Timing

The timing equipment provides the necessary gating pulses for the peak detector, boxcar sampler, reset, and azimuth-of-arrival gate generator circuits. A block diagram of one mode of the timing equipment is shown in Figure 38. Since the generation of gates for the four modes is the same, only one mode is shown.

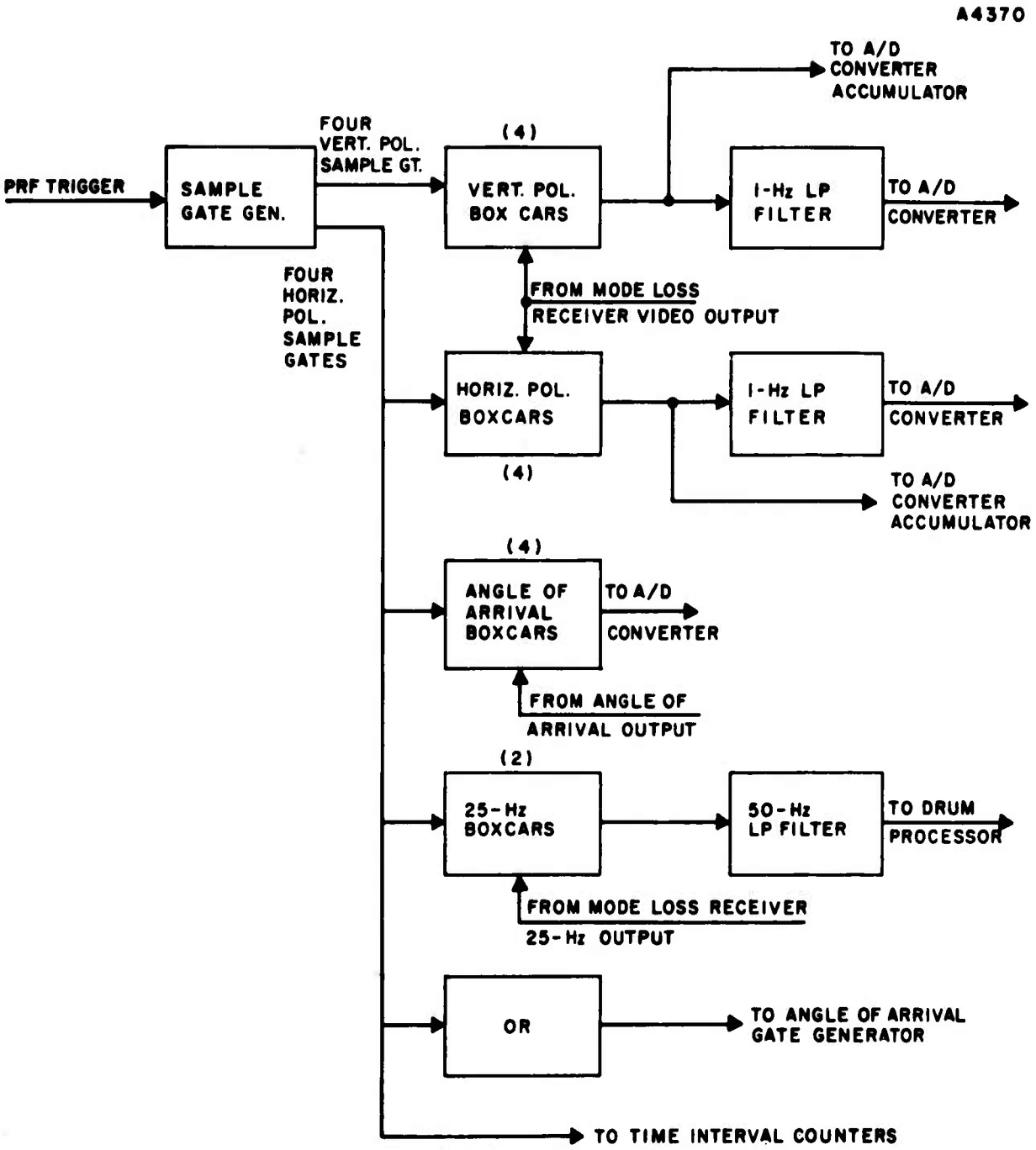

Figure 34. Mode Processor

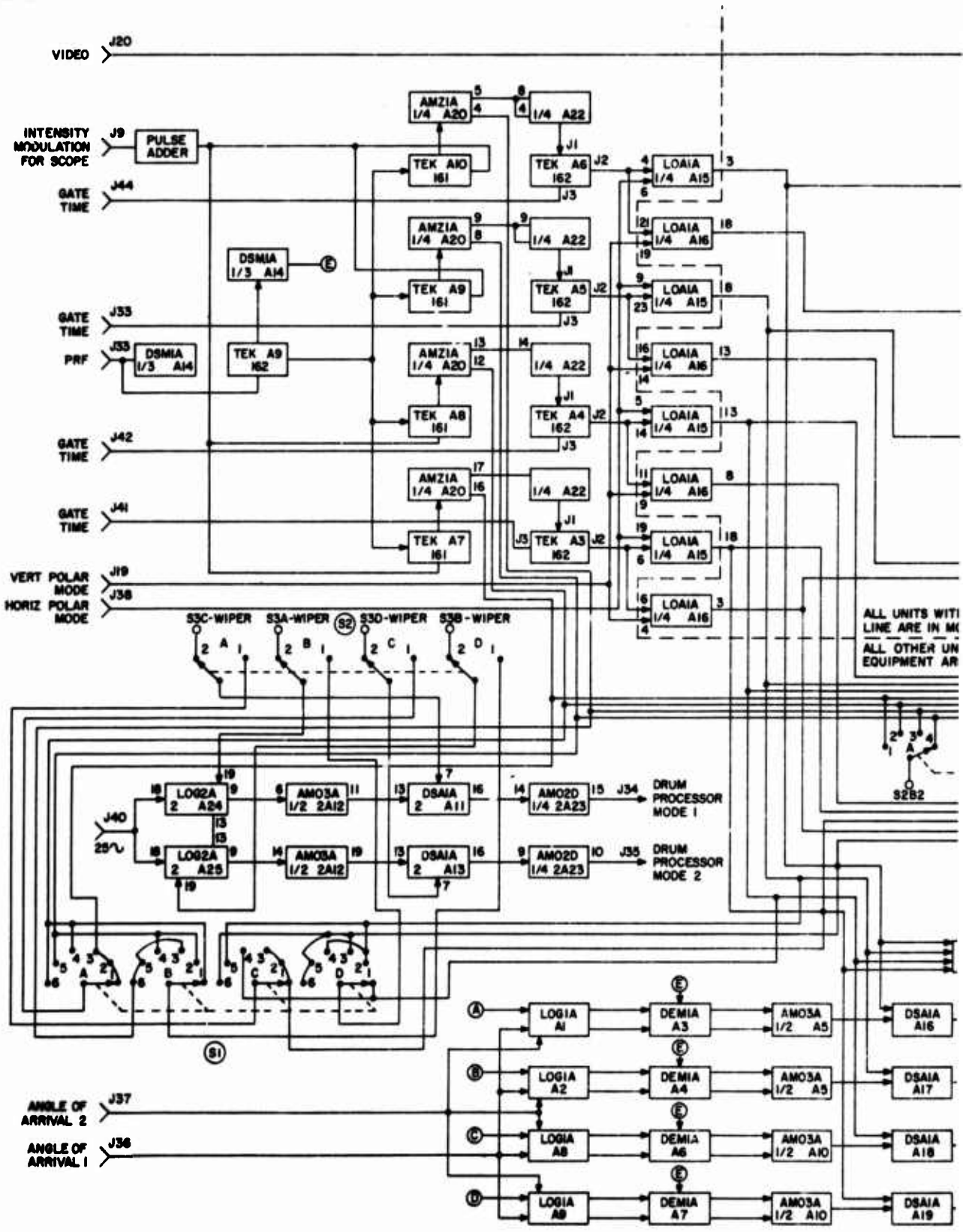
VIDEO
J20
INTENSITY MODULATION FOR SCOPE
J9
PULSE ADDER
GATE TIME
J44
GATE TIME
J33
PRF
J33
DSMIA 1/3 A14
GATE TIME
J42
GATE TIME
J41
VERT POLAR MODE
J19
HORIZ POLAR MODE
J38
AMZIA 1/4 A20
1/4 A22
TEK A10 161
TEK A6 162
LOAIA 1/4 A15
TEK A9 161
TEK A5 162
LOAIA 1/4 A16
TEK A8 161
TEK A4 162
TEK A7 161
TEK A3 162
S3C-WIPER
S3A-WIPER
S2
S3D-WIPER
S3B-WIPER
LOG2A 2 A24
LOG2A 2 A25
AMO3A 1/2 2A12
DSAIA 2 A11
DSAIA 2 A13
AMO2D 1/4 2A23
J34
J35
DRUM PROCESSOR MODE 1
DRUM PROCESSOR MODE 2
J40
25V
S1
LOGIA A1
LOGIA A2
LOGIA A8
LOGIA A9
DEMIA A3
DEMIA A4
DEMIA A6
DEMIA A7
AMO3A 1/2 A5
AMO3A 1/2 A10
DSAIA A16
DSAIA A17
DSAIA A18
DSAIA A19
ANGLE OF ARRIVAL 2
J37
ANGLE OF ARRIVAL 1
J36
ALL UNITS WITH
LINE ARE IN M
ALL OTHER UN
EQUIPMENT AR
S2B2

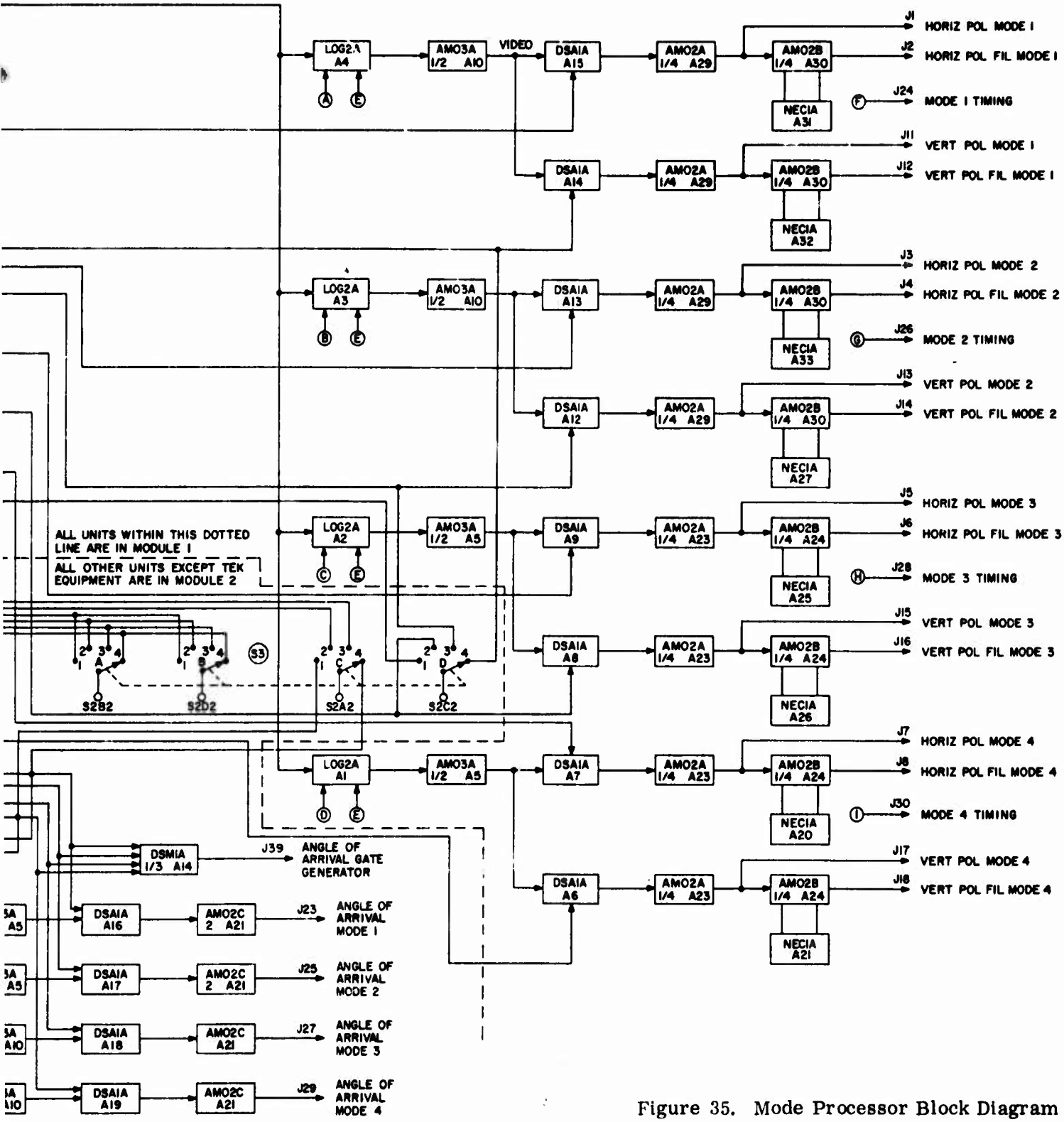

Figure 35. Mode Processor Block Diagram

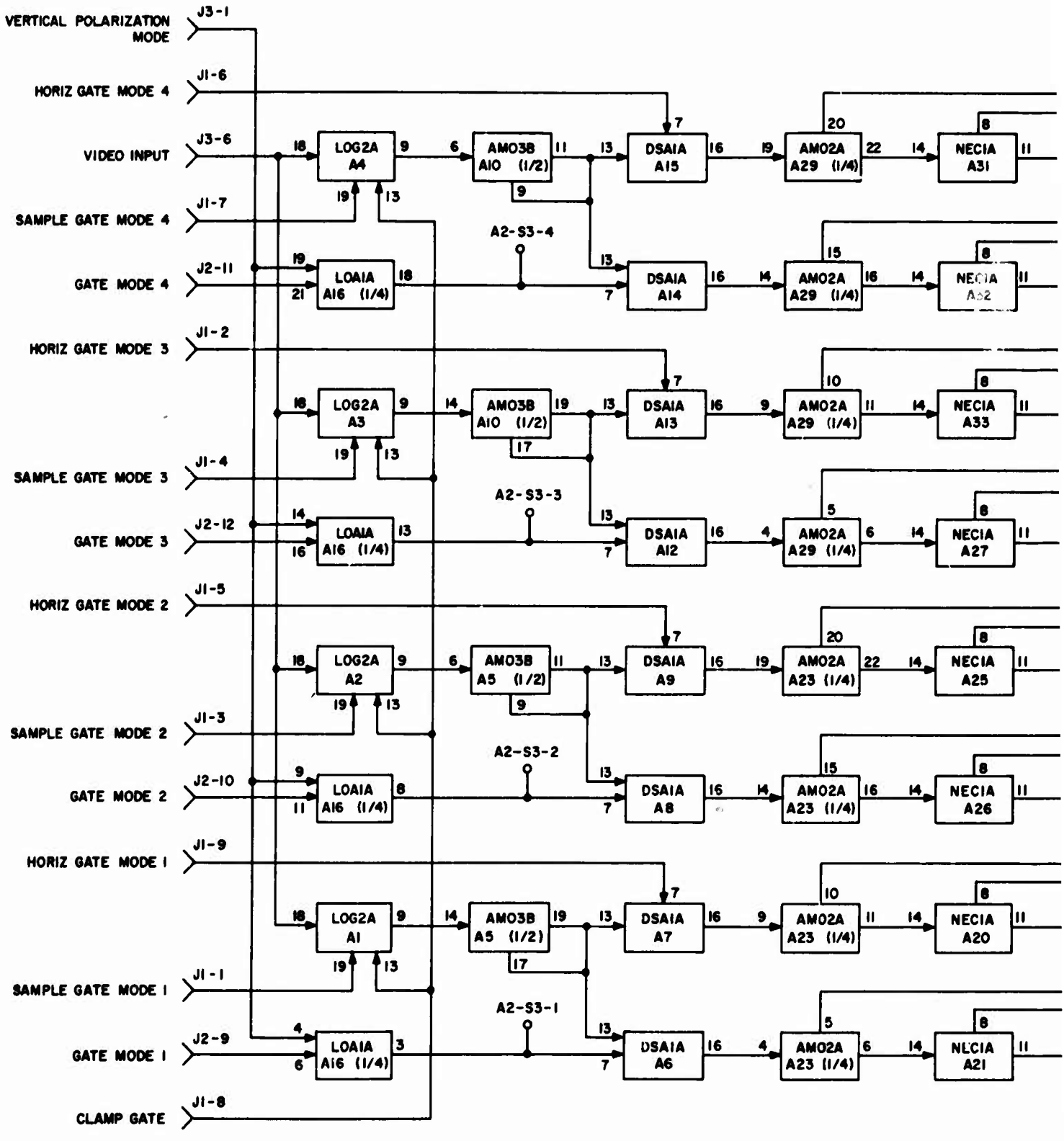
VERTICAL POLARIZATION MODE
J3-1
HORIZ GATE MODE 4
J1-6
VIDEO INPUT
J3-6
SAMPLE GATE MODE 4
J1-7
GATE MODE 4
J2-11
HORIZ GATE MODE 3
J1-2
SAMPLE GATE MODE 3
J1-4
GATE MODE 3
J2-12
HORIZ GATE MODE 2
J1-5
SAMPLE GATE MODE 2
J1-3
GATE MODE 2
J2-10
HORIZ GATE MODE 1
J1-9
SAMPLE GATE MODE 1
J1-1
GATE MODE 1
J2-9
CLAMP GATE
J1-8
LOG2A A4
LOG2A A3
LOG2A A2
LOG2A A1
LOAIA A16 (1/4)
AM03B A10 (1/2)
AM03B A5 (1/2)
A2-S3-4
A2-S3-3
A2-S3-2
A2-S3-1
DSAIA A15
DSAIA A14
DSAIA A13
DSAIA A12
DSAIA A9
DSAIA A8
DSAIA A7
DSAIA A6
AM02A A29 (1/4)
AM02A A23 (1/4)
NECIA A31
NECIA A32
NECIA A33
NECIA A27
NECIA A25
NECIA A26
NECIA A20
NECIA A21

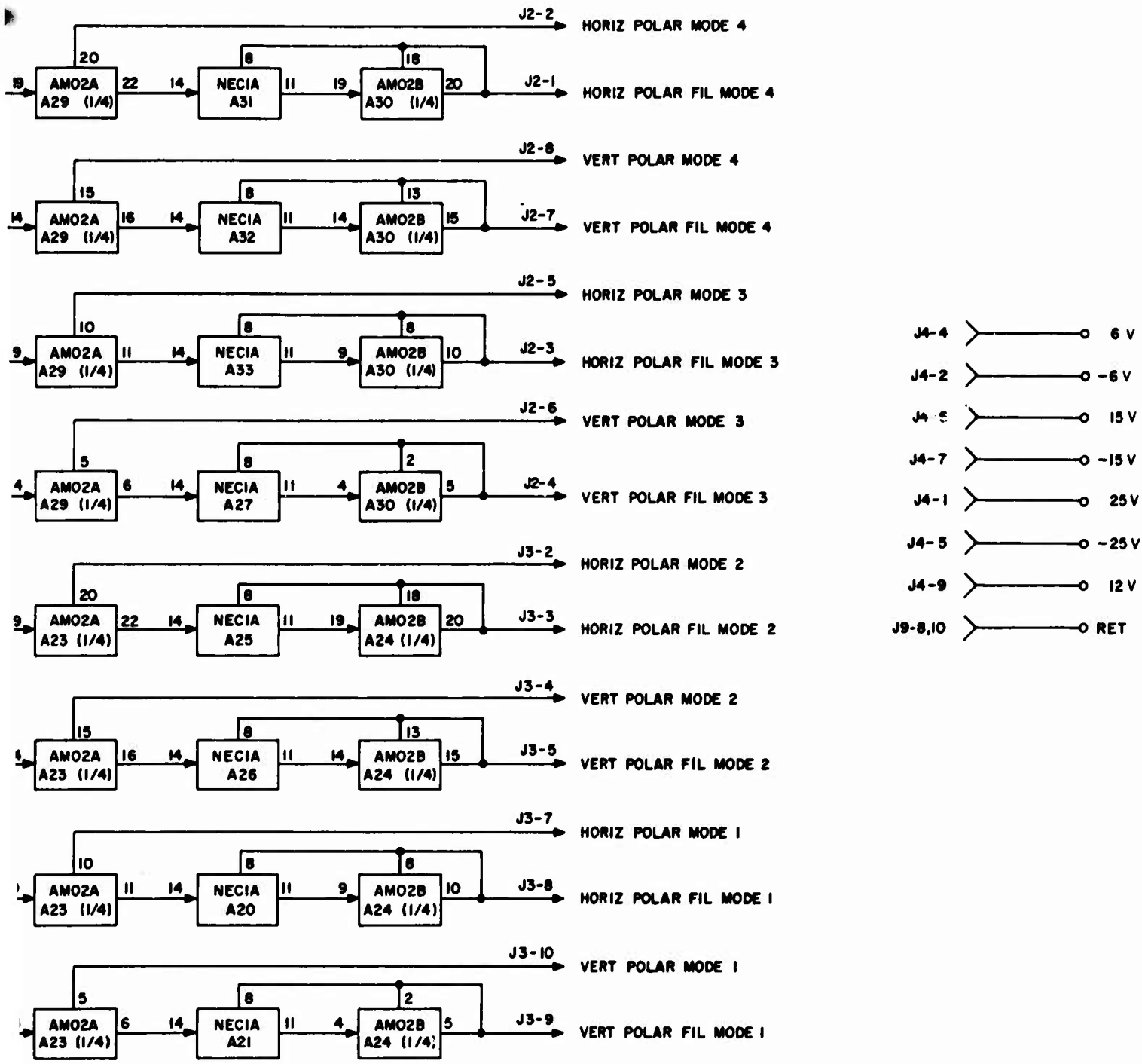

Figure 36. Mode Processor Module 1

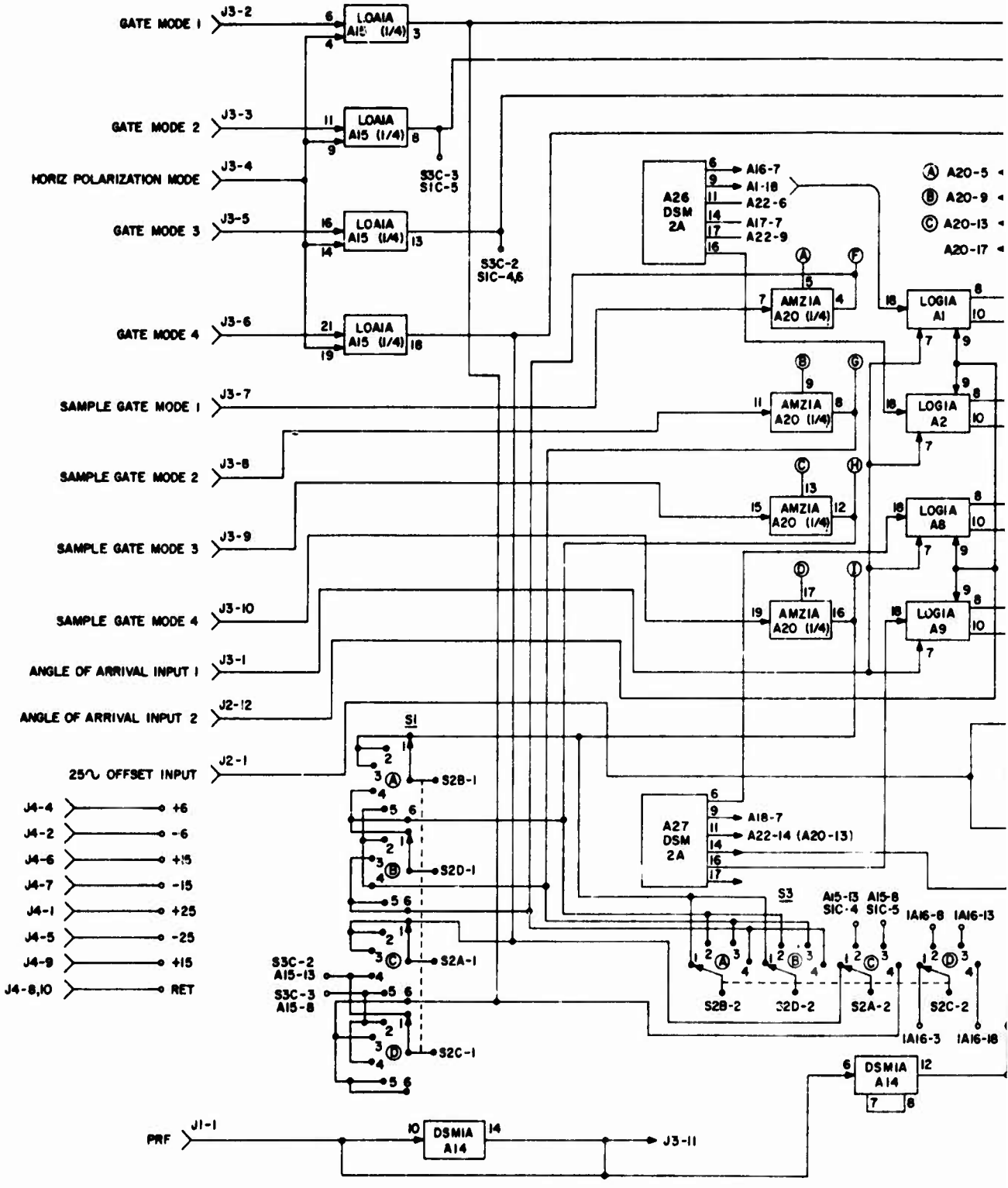
GATE MODE 1
J3-2
LOAIA A15 (1/4)
GATE MODE 2
J3-3
LOAIA A15 (1/4)
HORIZ POLARIZATION MODE
J3-4
S3C-3 S1C-5
GATE MODE 3
J3-5
LOAIA A15 (1/4)
S3C-2 S1C-4,6
GATE MODE 4
J3-6
LOAIA A15 (1/4)
SAMPLE GATE MODE 1
J3-7
SAMPLE GATE MODE 2
J3-8
SAMPLE GATE MODE 3
J3-9
SAMPLE GATE MODE 4
J3-10
ANGLE OF ARRIVAL INPUT 1
J3-1
ANGLE OF ARRIVAL INPUT 2
J2-12
25Ω OFFSET INPUT
J2-1
J4-4 +6
J4-2 -6
J4-6 +15
J4-7 -15
J4-1 +25
J4-5 -25
J4-9 +15
J4-8,10 RET
A26 DSM 2A
A16-7
A1-18
A22-6
A17-7
A22-9
A20-5
A20-9
A20-13
A20-17
AMZIA A20 (1/4)
LOGIA A1
LOGIA A2
LOGIA A8
LOGIA A9
A27 DSM 2A
A18-7
A22-14 (A20-13)
S1
S2B-1
S2D-1
S2A-1
S2C-1
S3
A15-13 S1C-4
A15-8 S1C-5
1A16-8
1A16-13
S2B-2
S2D-2
S2A-2
S2C-2
1A16-3
1A16-18
S3C-2 A15-13
S3C-3 A15-8
DSMIA A14
PRF
J1-1
J3-11

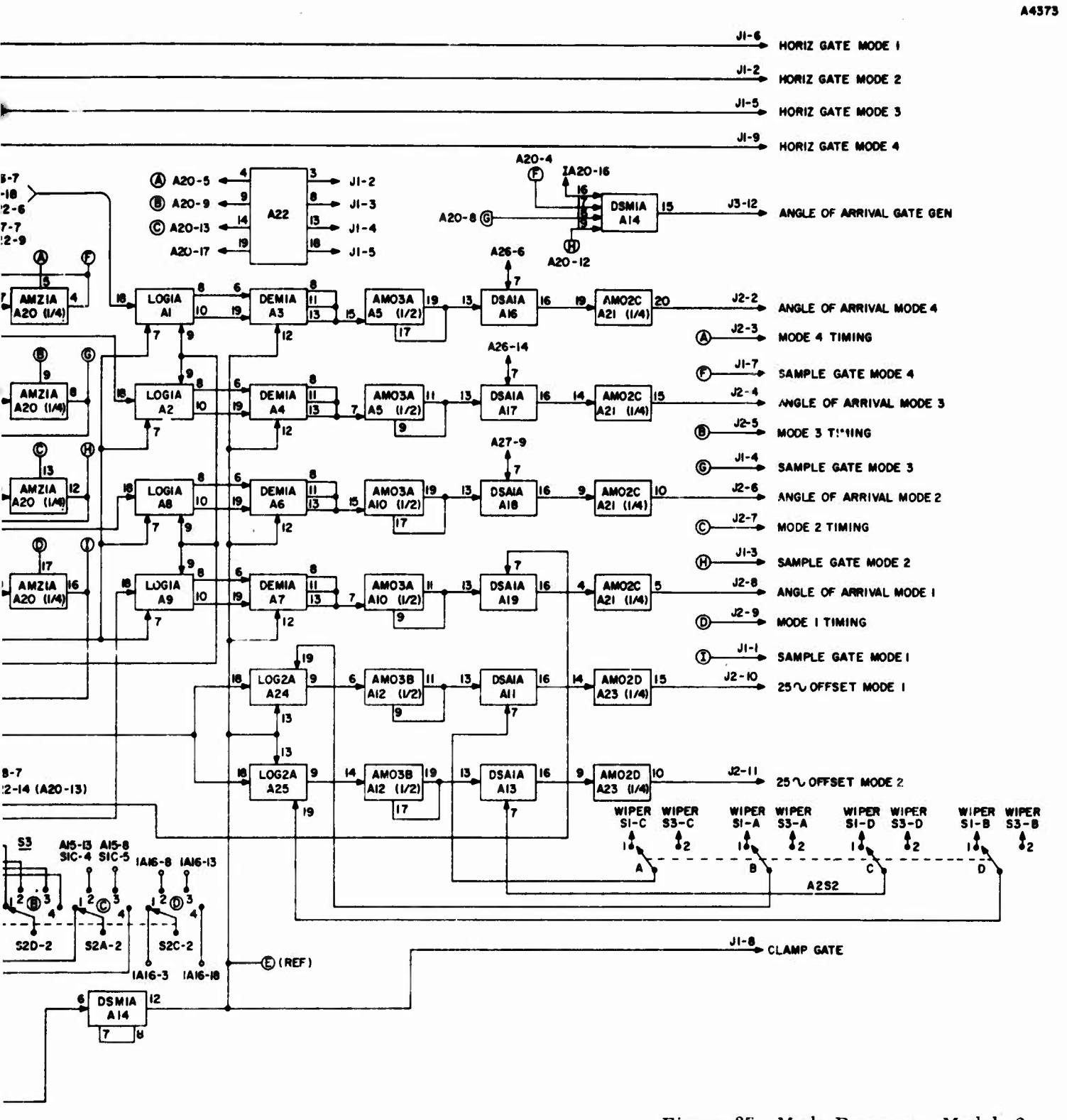

Figure 37. Mode Processor Module 2

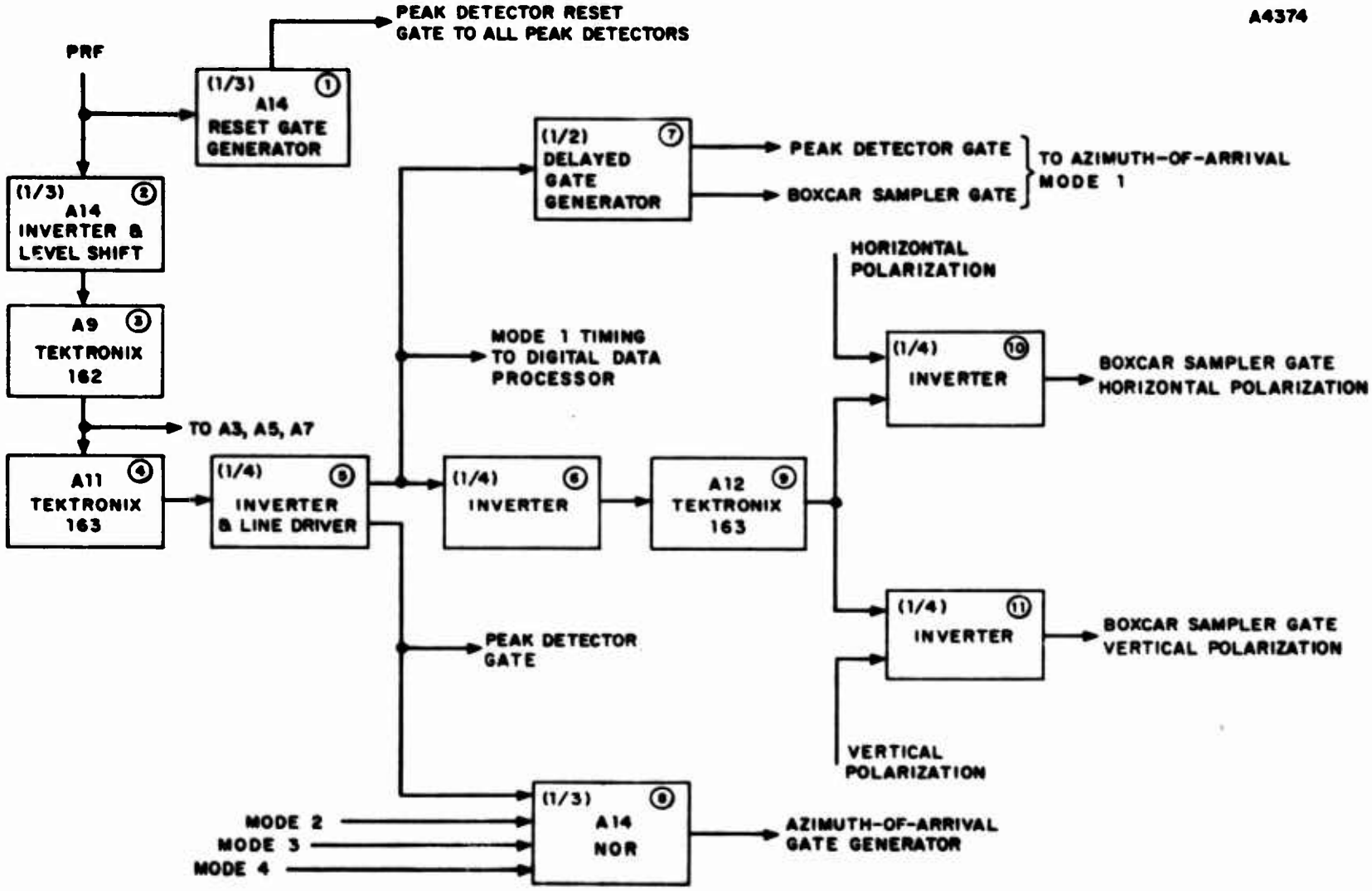

Figure 38. Timing Equipment, One Mode

The negative-going edge of the prf input is used to trigger a monostable multivibrator (Block 1) which provides a gate for resetting the output of all peak detector circuits. The negative-going edge is also level-shifted and inverted (Block 2) and used to trigger a Tektronix 162 waveform generator (Block 3). The sawtooth output of Block 3 is used to drive four Tektronix 163 generators. A delayed pulse is generated by a Tektronix 163 (Block 4) and the delay can be varied by allowing the Tektronix 163 to trigger at different levels of the sawtooth input. The pulse from Block 4 is then processed in an inverter and line driver circuit (Block 5) which provides one output to drive the peak detector gates for the mode loss receiver video channel and the mode loss receiver 25-Hz channel, and is also NORed (Block 8) with the peak detector gates of the other modes to provide an input for the azimuth-of-arrival gate generator.

The second output of Block 5 is a line driver output which provides a timing signal to the digital processor as well as driving an inverter (Block 6) and a delayed gate generator (Block 7). The delayed gate generator consists of three monostable circuits in series. The first monostable provides a delay for the azimuth-of-arrival peak detector and boxcar gates. This is necessary because of an approximate 15-μs delay between the sending of the azimuth-of-arrival gate generator pulse from Block 8 and the receiving of the corresponding azimuth-of-arrival receiver signal. The turn-off of the first monostable of Block 7 triggers the second monostable which provides the peak detector gate for the Mode 1 azimuth-of-arrival channel. The trailing edge of the inverter output (Block 6) triggers the Tektronix 163 (Block 9) which has a 10-μs wide pulse output. This output is NANDed with the horizontal polarization signal (Block 10) and with the vertical polarization signal (Block 11) to provide boxcar sample gates. A timing diagram for Mode 1 is shown in Figure 39.

(2) Mode Loss Receiver Video Processing

One mode of the mode loss receiver video processing circuitry is shown in block diagram form in Figure 40. The video input is sampled for 10 μs and the peak voltage in this interval is stored by the peak detector (Block 1). The boxcar driver (Block 2) provides a current drive for the boxcar circuit (Blocks 3 and 7). The boxcar is gated to sample the peak detector output for 10 μs following the peak detector sample period. The boxcar output is amplified (Block 4) and sent to the digital processor. The output of Block 4 is also passed through an active 1-Hz, three-pole low pass filter (Blocks 5 and 6) and this filtered output is also sent to the digital processor. Blocks 7, 8, 9, and 10 operate identically to Blocks 3, 4, 5, and 6 -- except one group processes a horizontal polarization input and the other group processes a vertical polarization input during one 10-ms time interval.

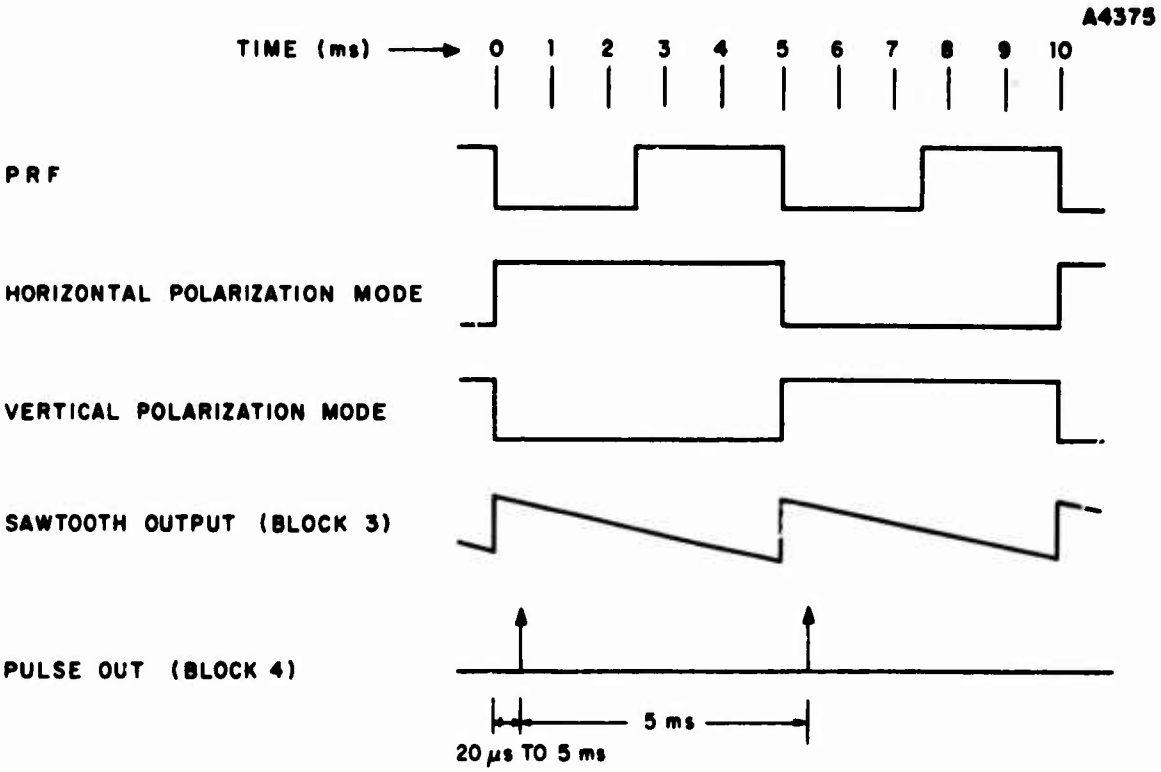

Figure 39. Timing Diagram

A 10-V output is obtained from the operational amplifier (Block 4) for 1.0-V peak input signal and the corresponding filtered output is 5.0 V.

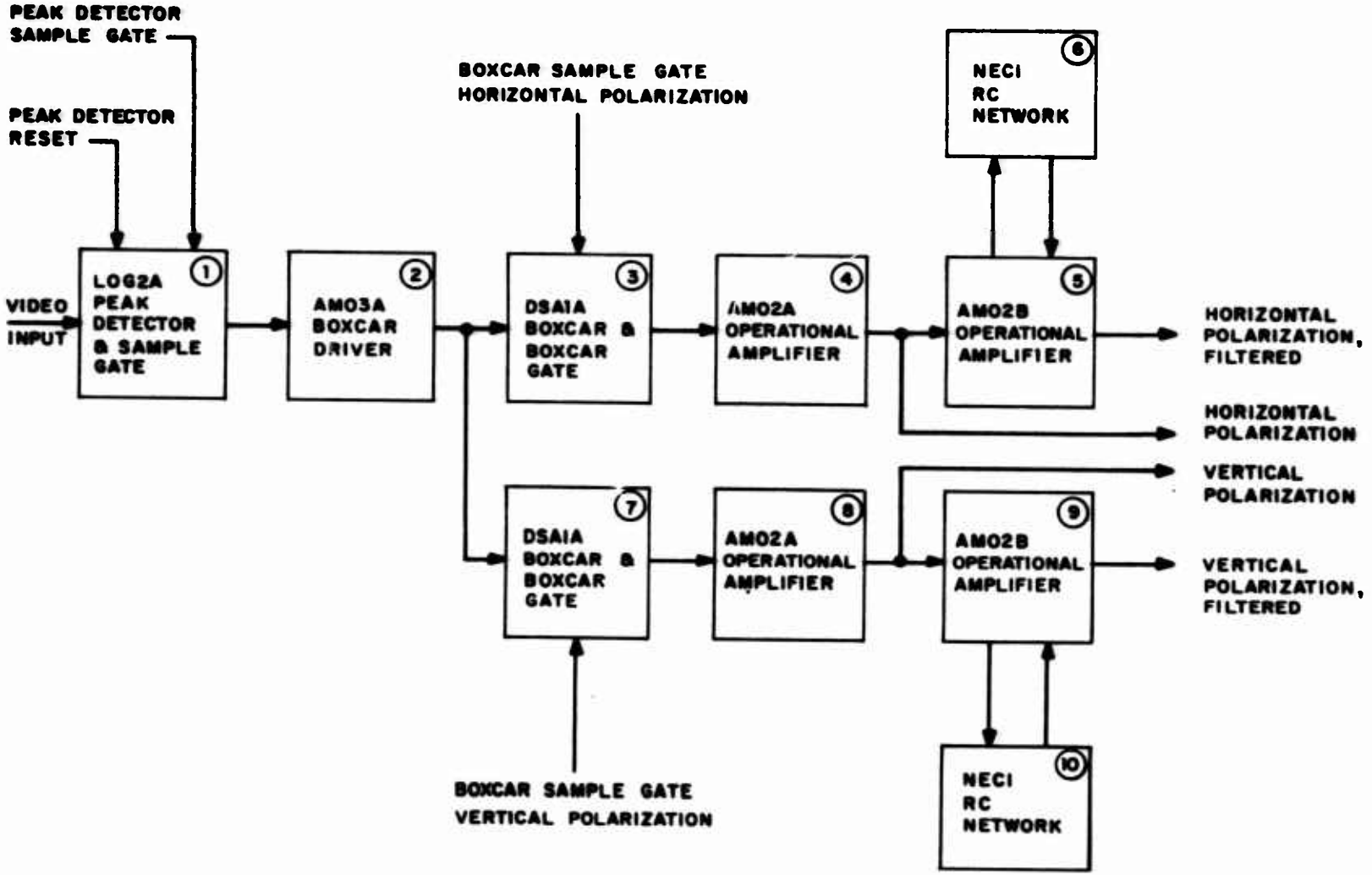

Figure 40. Mode Loss Receiver Video Processing, One Mode

(3) Mode Loss Receiver 25-Hz Output Processing

The block diagram of one mode for the processing of the mode loss receiver 25-Hz signal is shown in Figure 41. The operation of the blocks is identical to those explained for the video inputs, with the exception that there is no low pass filter for the 25-Hz signal. The boxcar sample gate for the 25-Hz signal occurs at the same time as the boxcar gate for horizontal polarization output for the video signal. An output of 5.0 V is obtained for a peak input of 1.0 V.

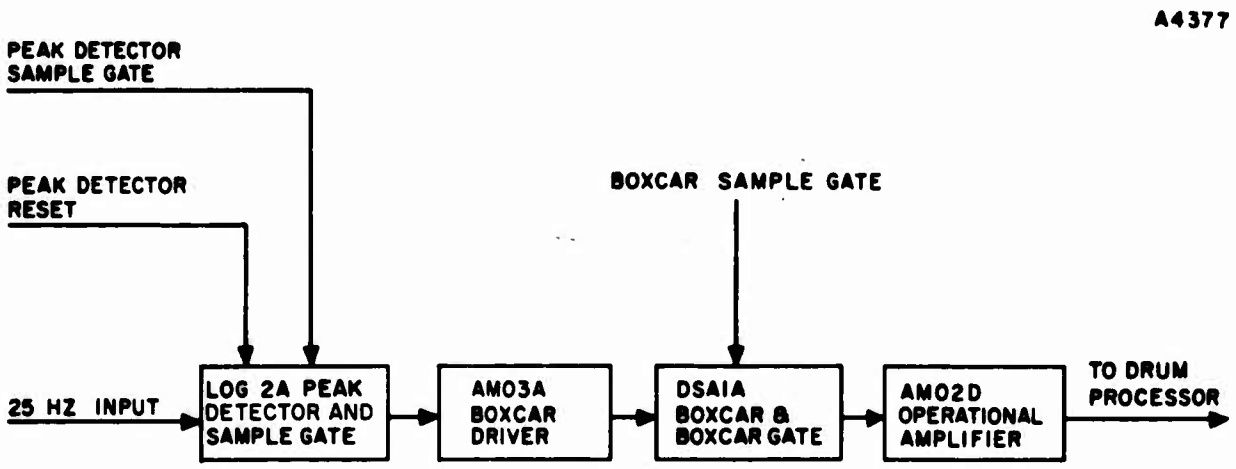

Figure 41. Mode Loss Receiver 25-Hz Output Processing, One Mode

(4) Azimuth-of-Arrival Processing

One mode of the azimuth-of-arrival processing circuits is shown in Figure 42. A dual sample gate (Block 1) is gated on during the time interval that the two azimuth-of-arrival inputs are present. The dual peak detector (Block 2) detects the peaks of the two inputs and provides the summing resistors for the peak detected signals -- one of which is inverted -- and an offset voltage. The output of the boxcar driver (Block 3) is then the summed voltage of the two azimuth-of-arrival inputs and an offset voltage, and provides the current drive for the boxcar capacitor. The inverting of one input and addition of an offset voltage is necessary to provide an output to the digital processor that varies from a minimum of 0 V to a maximum of 3.75 V. Although the azimuth-of-arrival inputs are both positive pulses of varying magnitude, the functions of Blocks 4 and 5 are identical to similar blocks explained for the Mode Loss Receiver video processing. Figure 43 is a plot of azimuth-of-arrival output voltage to the digital processor versus the difference voltage of the two azimuth-of-arrival inputs to the mode processor.

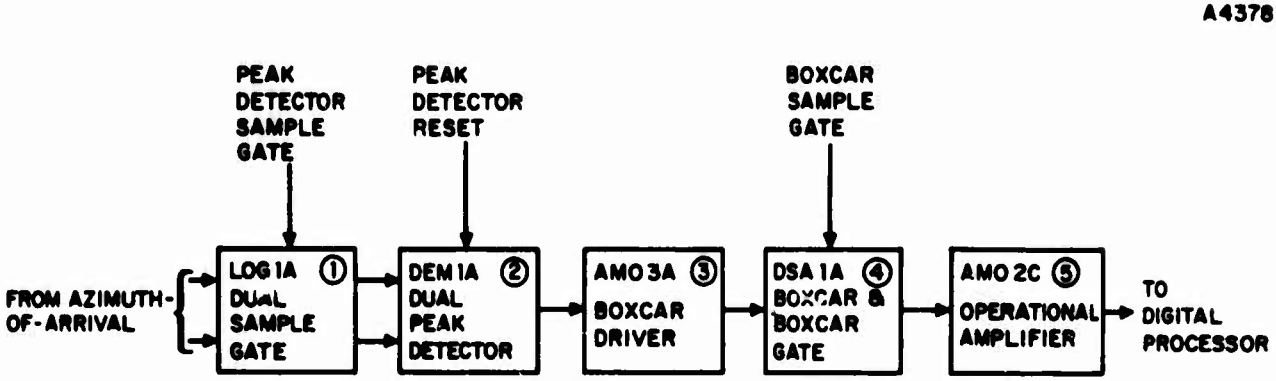

Figure 42. Azimuth-of-Arrival Processing, One Mode

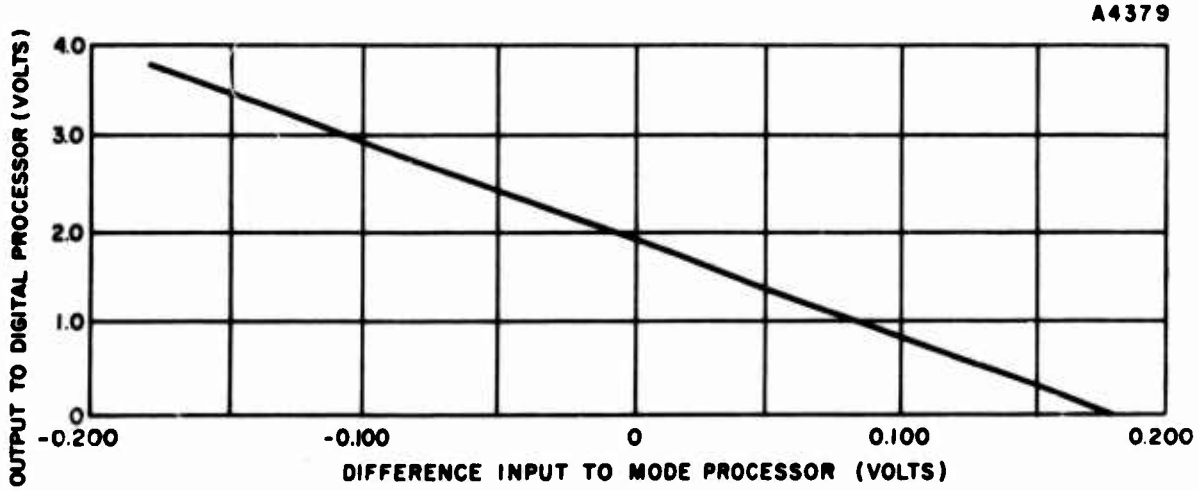

Figure 43. Azimuth-of-Arrival Output to Digital Processor

b. Card Description

(1) Operational Amplifier (AMO2 A/B/C/D)

The basic operation of the AMO2 card is that of an operational amplifier; there are four identical sections on each card. One section contains A1 (Figure 44) and will be explained. A1 is an operational amplifier which has an inverting input (pin 18) and a noninverting input (pin 19). Pin 19 provides a very high input impedance suitable for loading a storage capacitor in a boxcar circuit. The gain of A1 is determined by R1, R2, and R4, and with the input at pin 19 is

$$G = 1 + \frac{R4}{R1 + R2}$$

R3 is used to set the offset voltage of A1 to zero and R5 and R6 are a simple voltage divider.

(2) Operational Amplifier and Current Driver (AMO2A)

AMO3A provides current drive for the boxcar capacitor and contains two identical circuits. The one containing A1 (Figure 45) will be explained. A1 is an operational amplifier and, with pins 17 and 19 tied together, the gain from pin 14 to pin 19 is

$$G = -\frac{R3}{R1}$$

for the frequency range of interest. C1 is for noise reduction and decreasing of overshoot. R21 provides a bias current to offset the voltage at pin 19. CR1 is a zener diode and provides dc coupling from the emitters of Q1 and Q2 to the base of Q3. The transistors provide the current drive necessary for charging the boxcar capacitor in the circuit following the AMO3A.

(3) Line Driver, Inverter (AMZ1A)

The AMZ1A provides a line driver output and an inverted output for each input signal. There are four identical circuits in the AMZ1A board; the operation of one will be explained (Figure 46). R1 and R2 are a voltage divided at the input, Q1 provides a line driver output, and Q2 provides an inverted output.

(4) Dual Peak Detector (DEM1A)

The dual peak detector card, DEM1A, takes one of the azimuth-of-arrival inputs and inverts and amplifies it by the means of operational amplifier A1 (Figure 47). CR3 and C2 peak detect and store the most negative signal out of A1. The diode, CR3, is within the gain loop of the operational amplifier to minimize the contact potential of the diode.

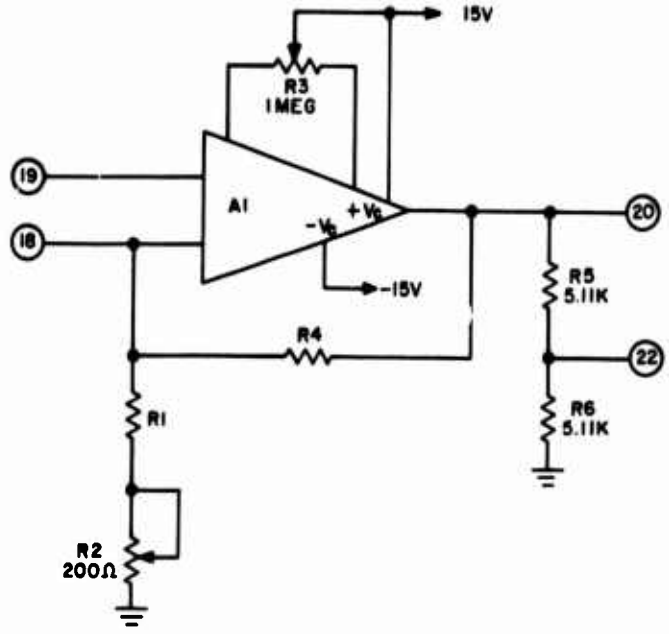

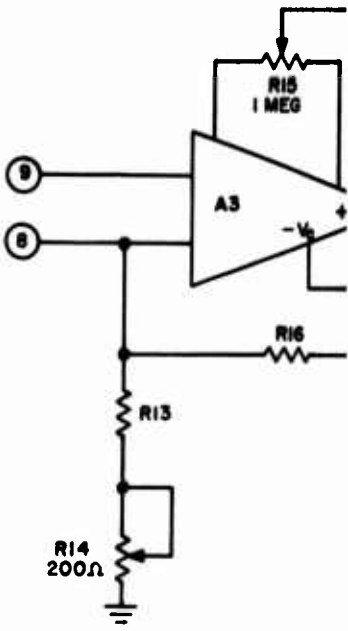

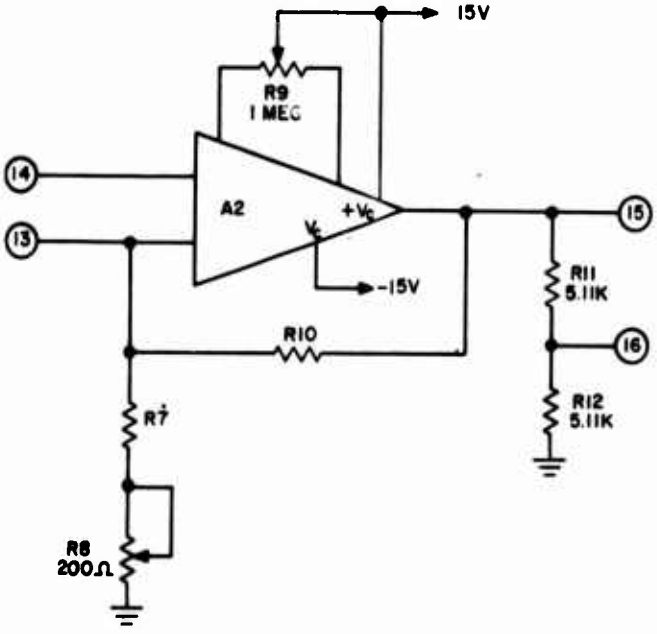

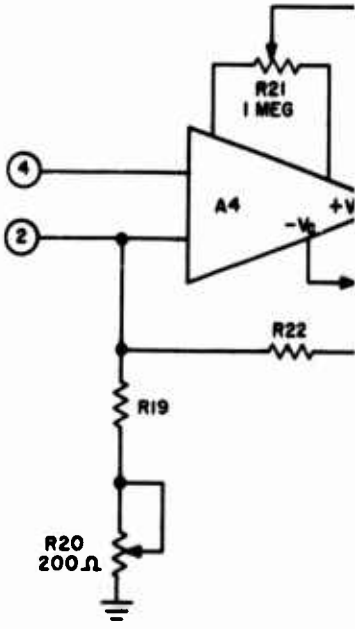

NOTE: PINS 7, 12, 17 MUST BE GROUNDED FOR PROPER OPERATION.

A4380

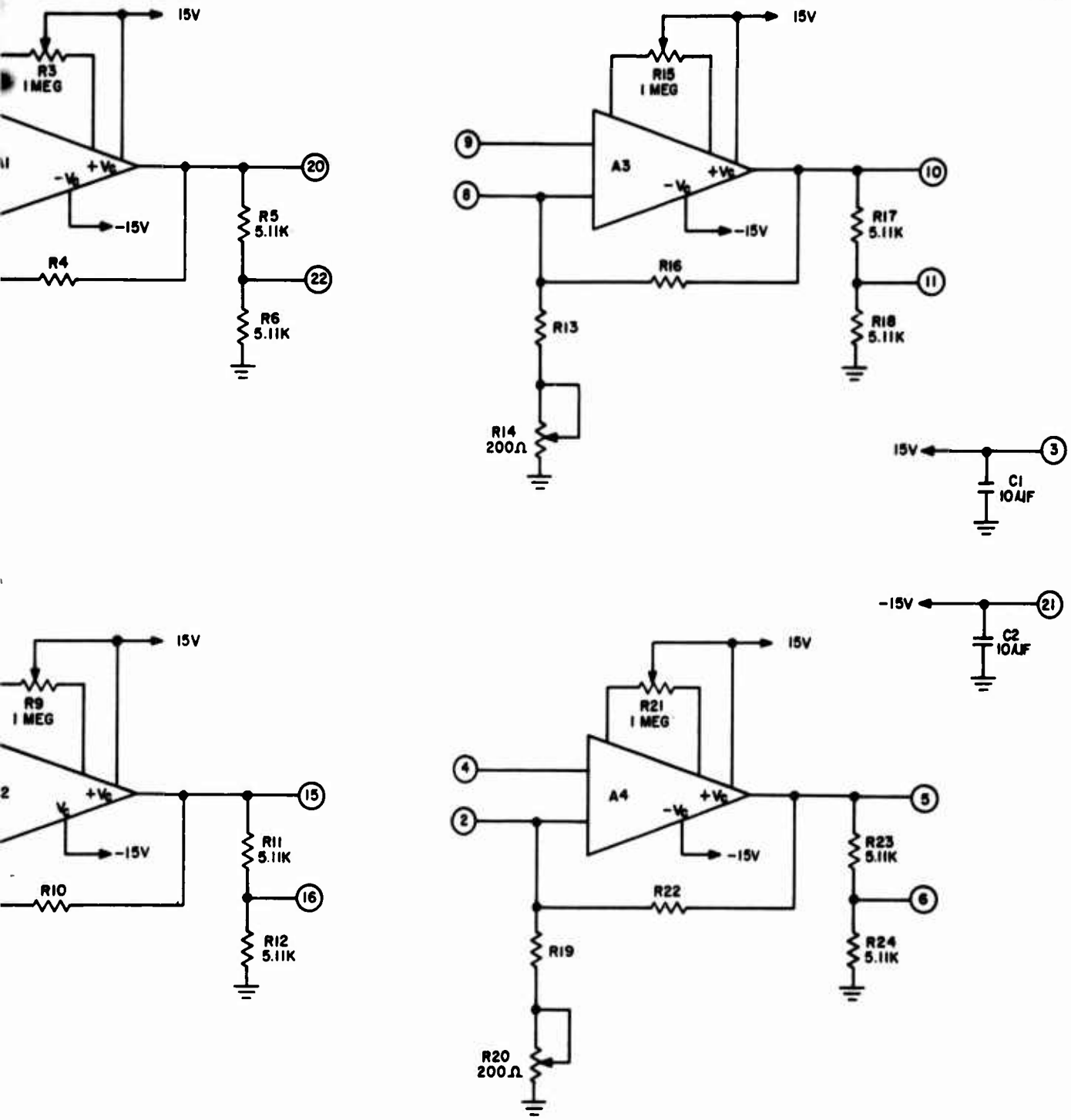

NOTE: PINS 7, 12, 17 MUST BE GROUNDED FOR PROPER OPERATION.

Figure 44. Operational Amplifier (AMO2 A/B/C/D)

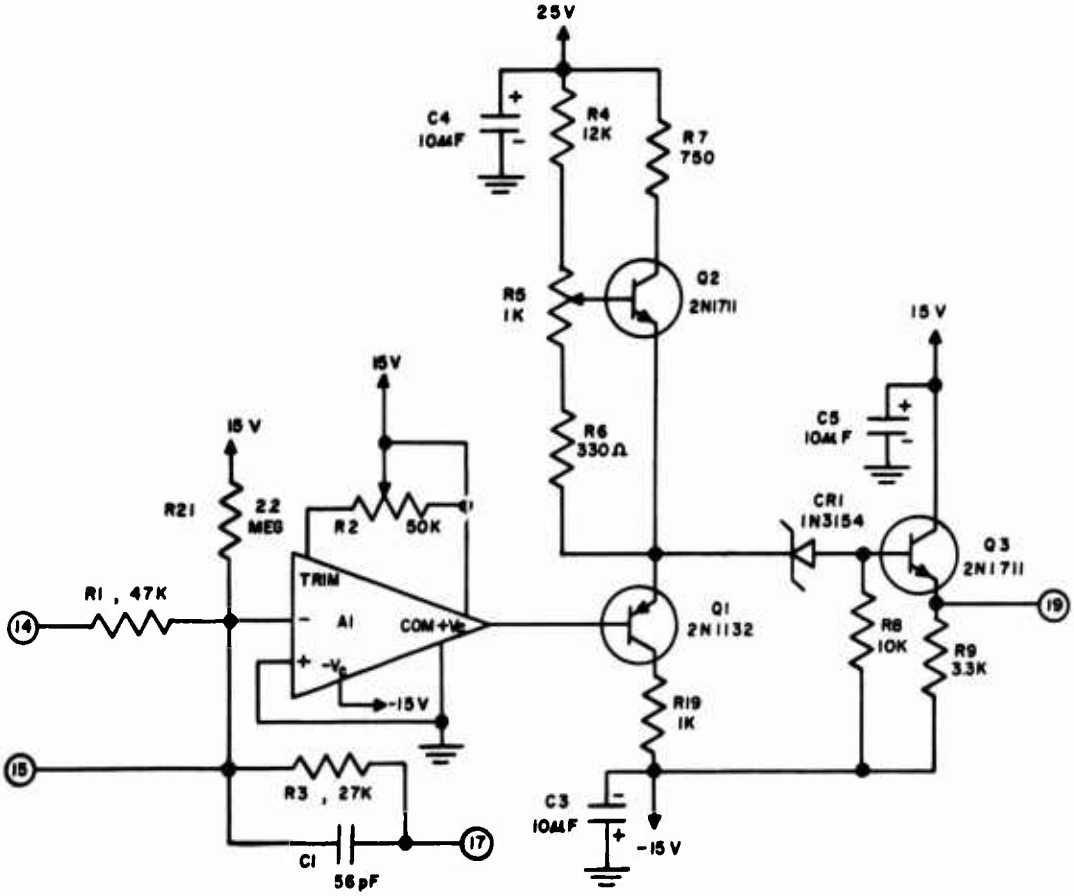
25V
C4
10MF
R4
12K
R7
750
Q2
2N1711
R5
1K
R6
330Ω
15V
15V
15V
C5
10MF
CR1
1N3154
Q3
2N1711
R21
22
MEG
R2
50K
TRIM
A1
COM
-15V
R1 , 47K
Q1
2N1132
R8
10K
R9
3.3K
R19
1K
14
15
17
19
R3 , 27K
C1
56pF
C3
10MF
-15V

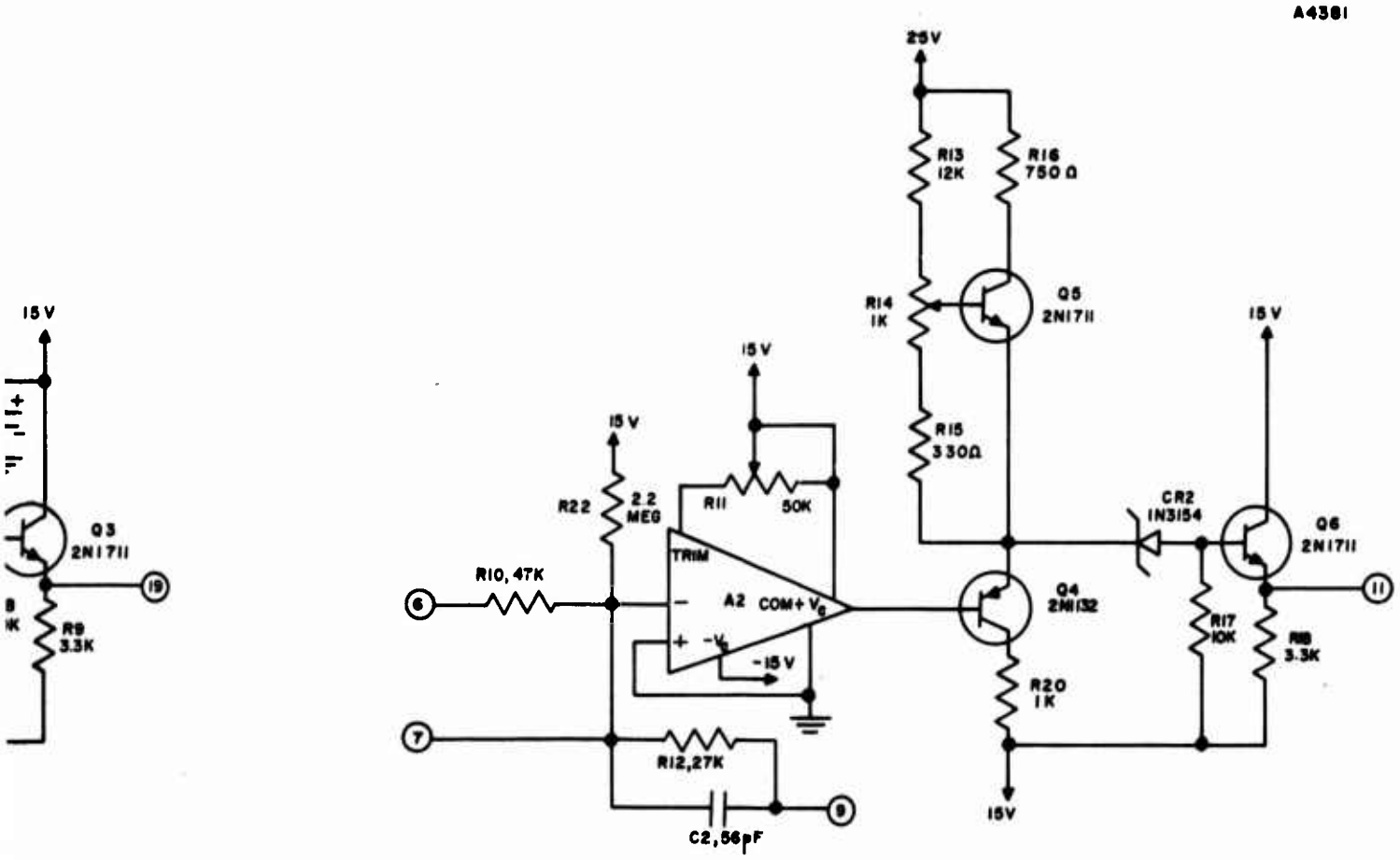

Figure 45. Operational Amplifier and Current Driver (AMO3A)

2

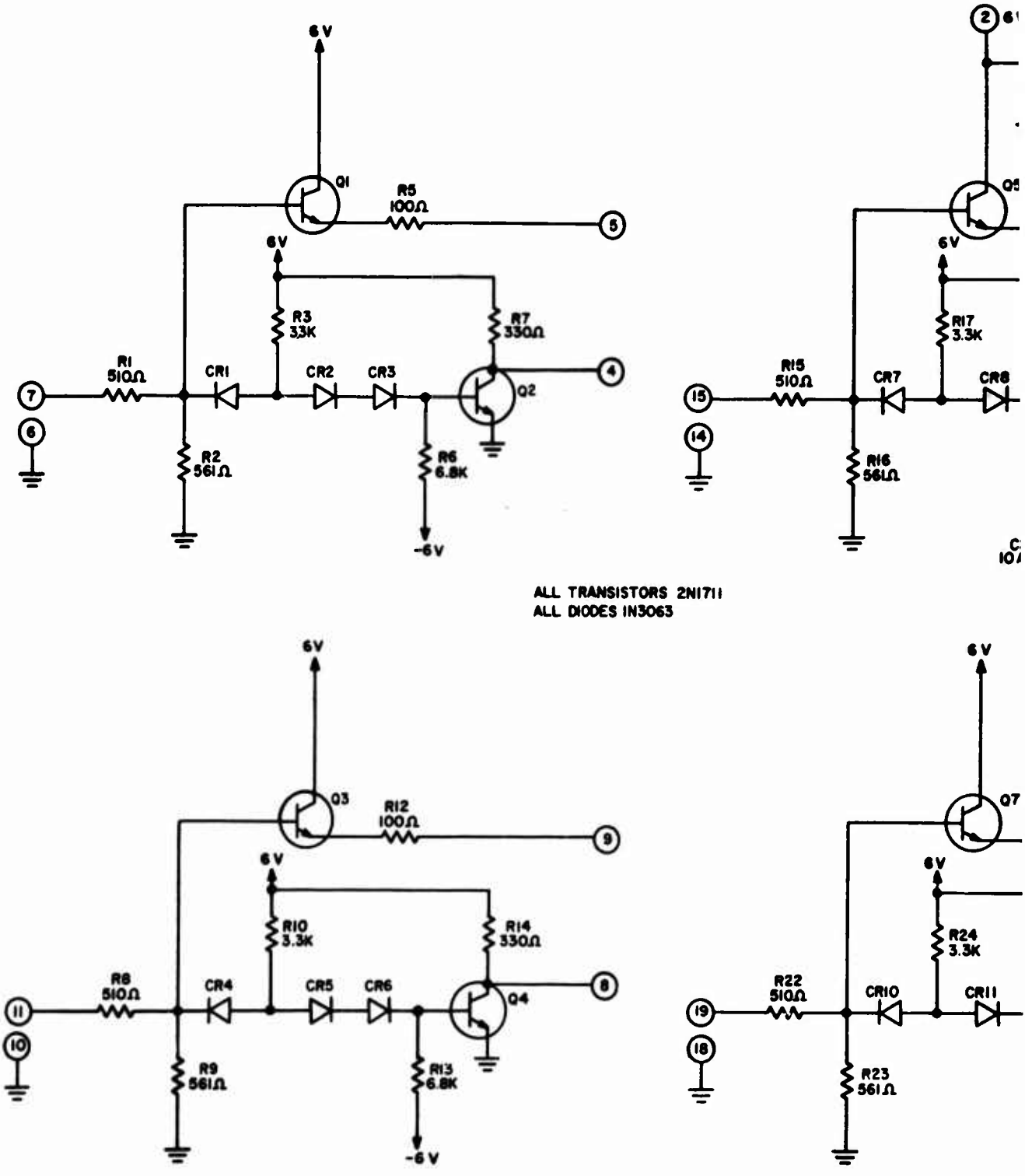

Figure 46. Line

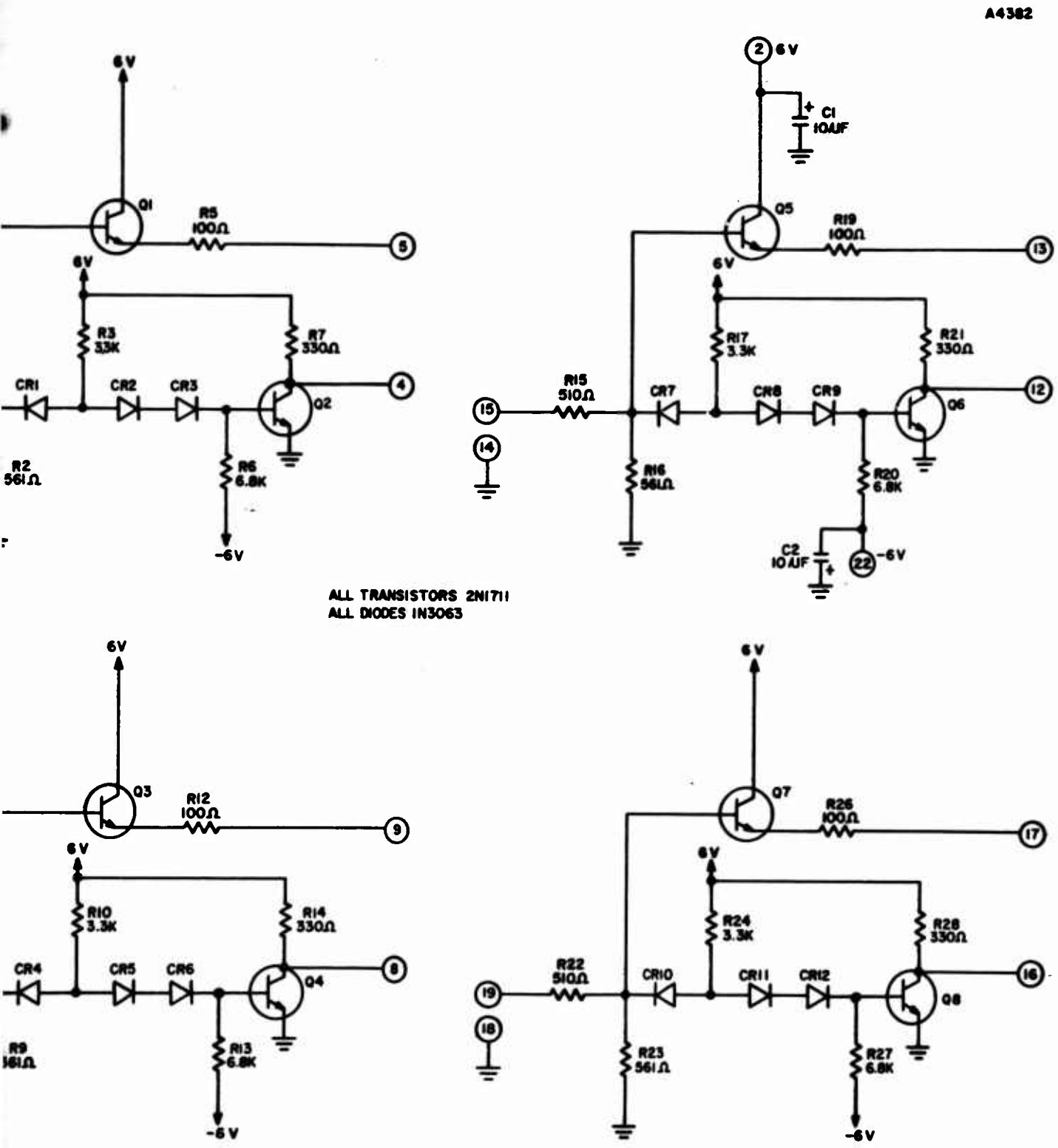

Figure 46. Line Driver, Inverter (AMZ1A)

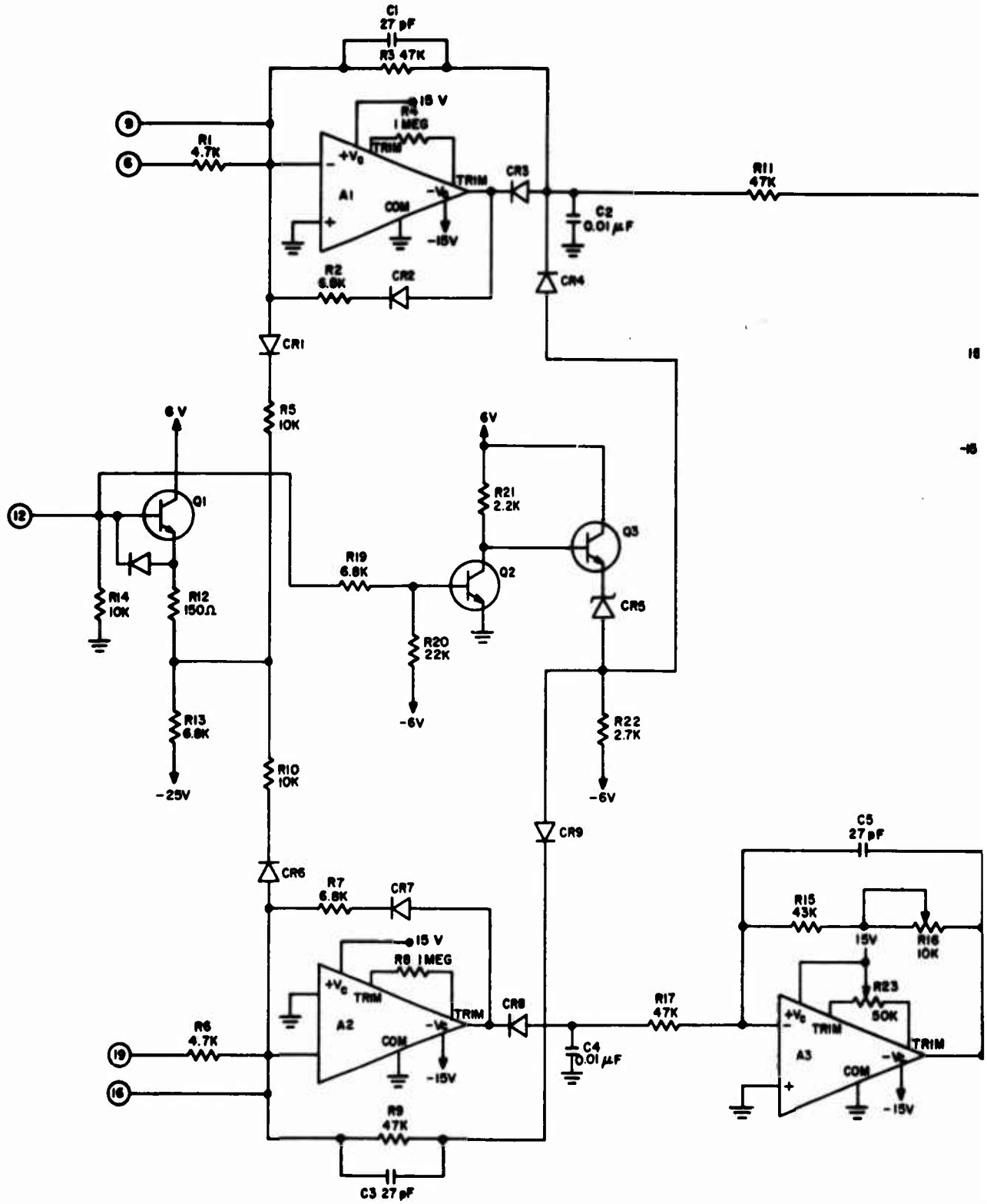
C1
27 pF
R3 47K
15 V
R4
1 MEG
TRIM
+Vo
-Vo
A1
COM
-15V
TRIM
CR3
R11
47K
C2
0.01 µF
R1
4.7K
R2
6.8K
CR2
CR4
CR1
R5
10K
6 V
Q1
R14
10K
R12
150Ω
-25V
R19
6.8K
6V
R21
2.2K
Q3
Q2
CR5
R20
22K
-6V
R22
2.7K
-6V
R13
6.8K
R10
10K
CR9
C5
27 pF
CR6
R7
6.8K
CR7
15 V
R8 1 MEG
A2
R6
4.7K
CR8
C4
0.01 µF
R17
47K
R15
43K
15V
R16
10K
R23
50K
A3
-15V
R9
47K
C3 27 pF

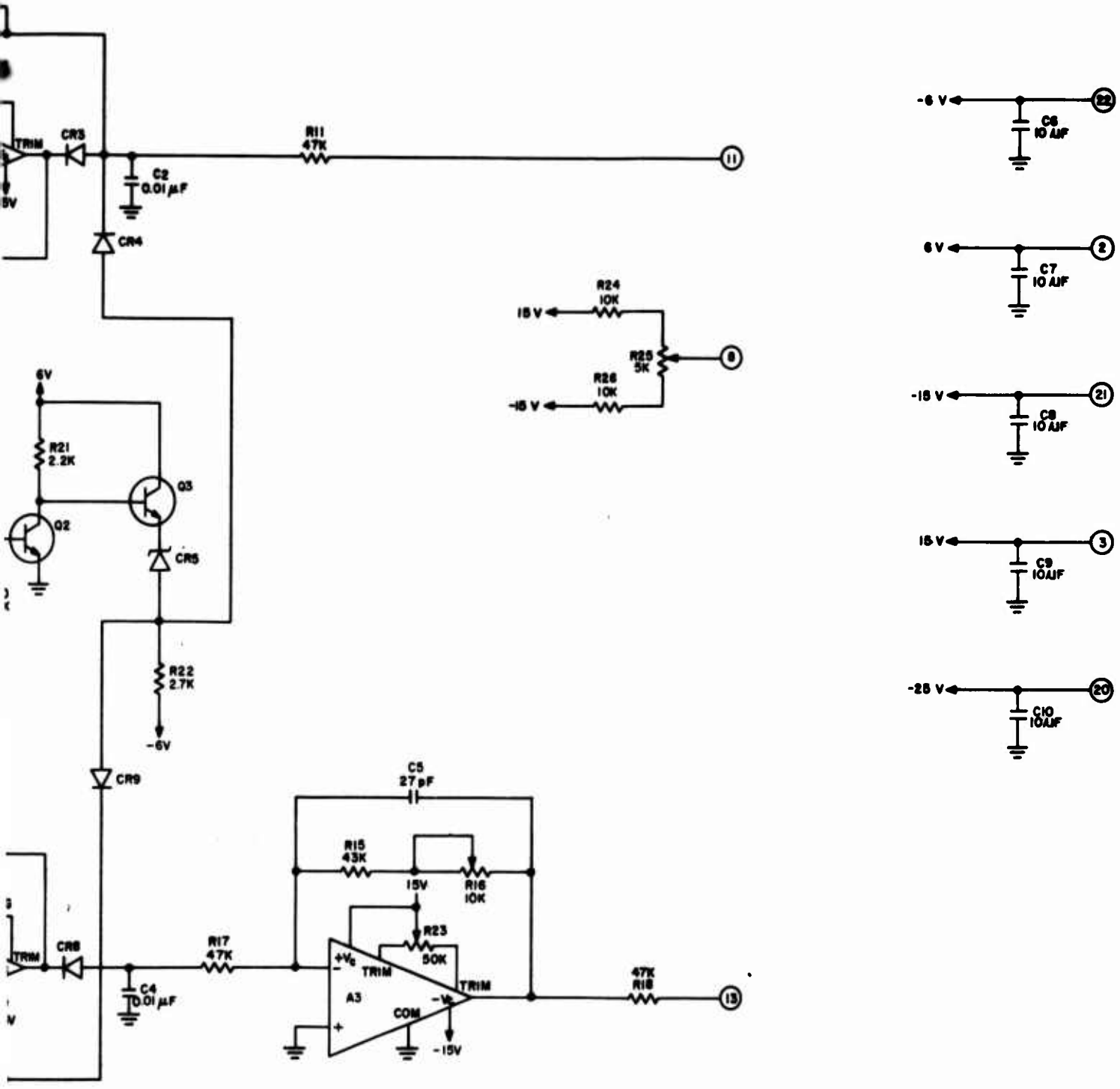

Figure 47. Dual Peak Detector (DEM1A)

If the voltage out of A1 is less than the voltage across C2, the gain of the operational amplifier from input to the output across C2 is

$$G = -\frac{R3}{R1}$$

R2 and CR2 limit the gain of the operational amplifier when CR3 is back-biased and keep A1 out of saturation.

A2 operates the same as A1, and A3 is a unity gain operational amplifier which inverts the voltage across C2. R16 is varied to make the voltage gain from pin 6 to the peak detected output across C2 equal to the voltage gain from pin 19 to the output of A3.

R11, R18, and R27 are the summing resistors for the two azimuth-of-arrival inputs and the offset voltage, and they provide the input for the following card.

Q1, Q2, and Q3 provide the reset function for the peak detector capacitor through CR4 and CR9. Q1 provides current through R5 and R10 necessary to drive the outputs of A1 and A2 positive while the peak detector capacitors are being reset.

(5) Boxcar and Boxcar Gate (DSA1A)

DSA1A is a boxcar and boxcar gate amplifier (Figure 48). C3 is the boxcar storage capacitor and CR1 through CR4 is a four-diode gate turned on by turning off Q2 and Q3, and Q1 provides the bias voltage necessary to turn the two transistors off. The voltage present at pin 13 is then also present at pin 16. When Q2 and Q3 are turned on by Q1, then CR4 and CR1 are back-biased by -5.5 V, and CR2 and CR3 are back-biased by 5.5 V and the voltage across C3 is then stored. Pin 16 must feed a very high impedance driver.

(6) Multivibrator, Four-Input NOR, Level Converter (DSM1A)

This card consists of three circuits which perform different functions. The first circuit (Figure 49) is a one-shot monostable multivibrator consisting of Q1, Q2, and Q3. Q1 and Q2 are a one-shot monostable and Q3 is a line driver output. A negative-going slope is necessary at pin 6 to trigger the monostable. The period of the monostable can be lengthened by adding a capacitor across pins 11 and 13.

The second circuit is a four-input OR function and consists of Q4, Q5, and their associated components. CR4, CR5, CR6, and CR7 with Q4 provide a four-input NOR circuit, and Q5 is a line driver output. The inputs to pins 16, 17, 18, and 19 are normally positive and any one of the inputs going to zero cause the output voltage at pin 15 to go positive to about 5 V.

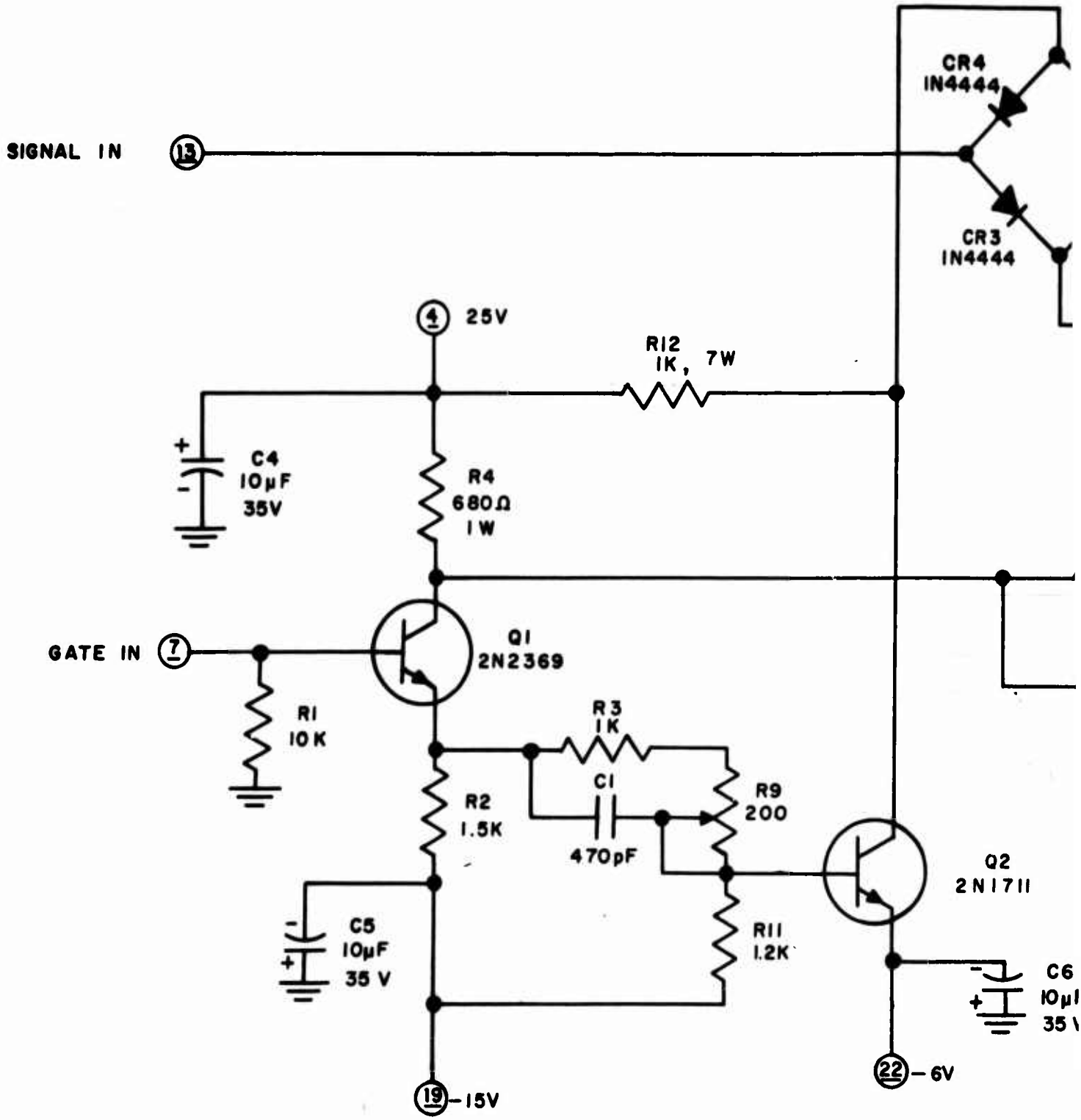
SIGNAL IN
13
CR4
IN4444
CR3
IN4444
4
25V
R12
1K, 7W
C4
10μF
35V
R4
680Ω
1W
GATE IN
7
Q1
2N2369
R1
10K
R3
1K
C1
470pF
R9
200
R2
1.5K
Q2
2N1711
C5
10μF
35 V
R11
1.2K
C6
10μ
35
22
-6V
19
-15V

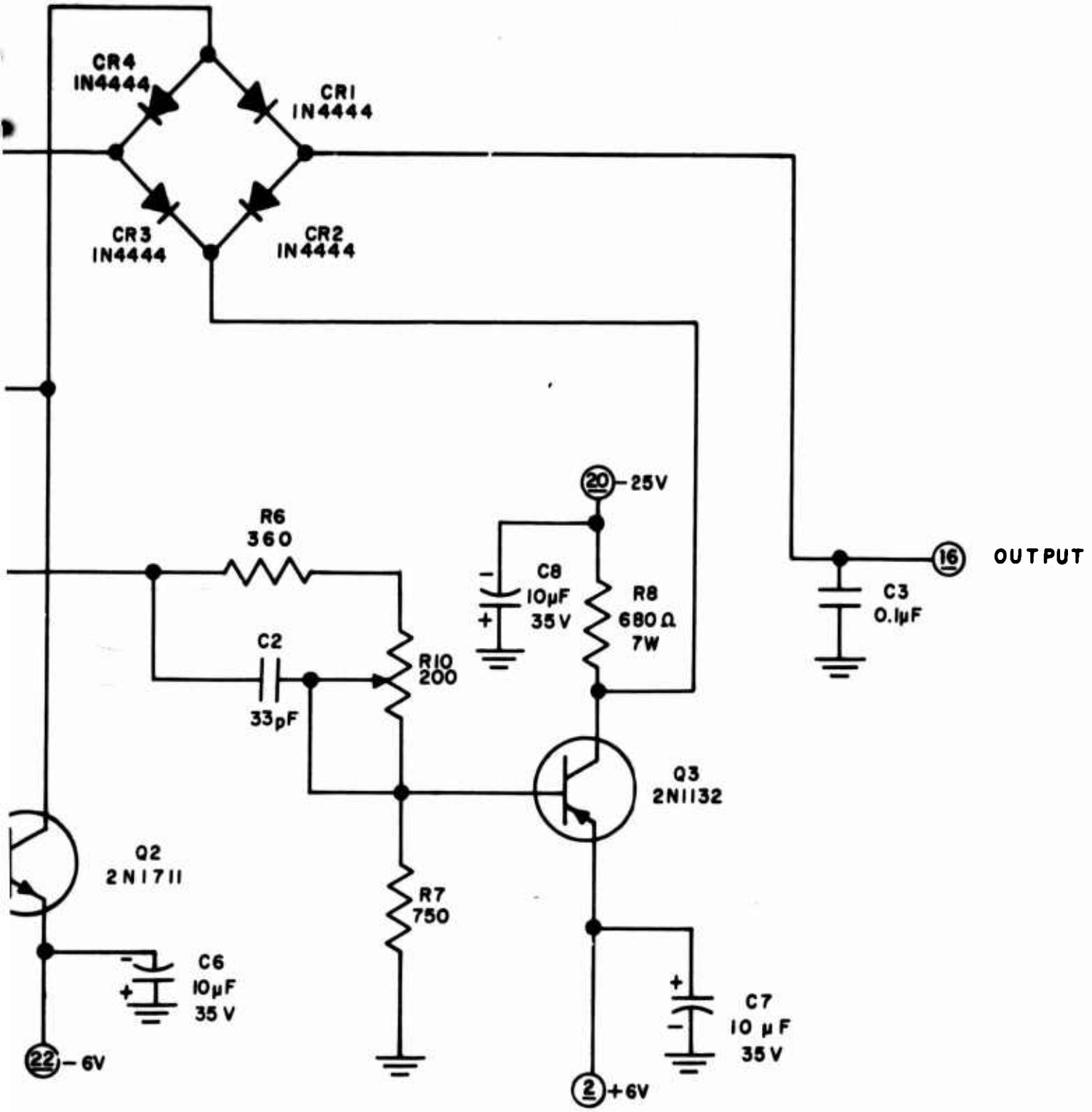

Figure 48. Boxcar and Boxcar Gate (DSA1A)

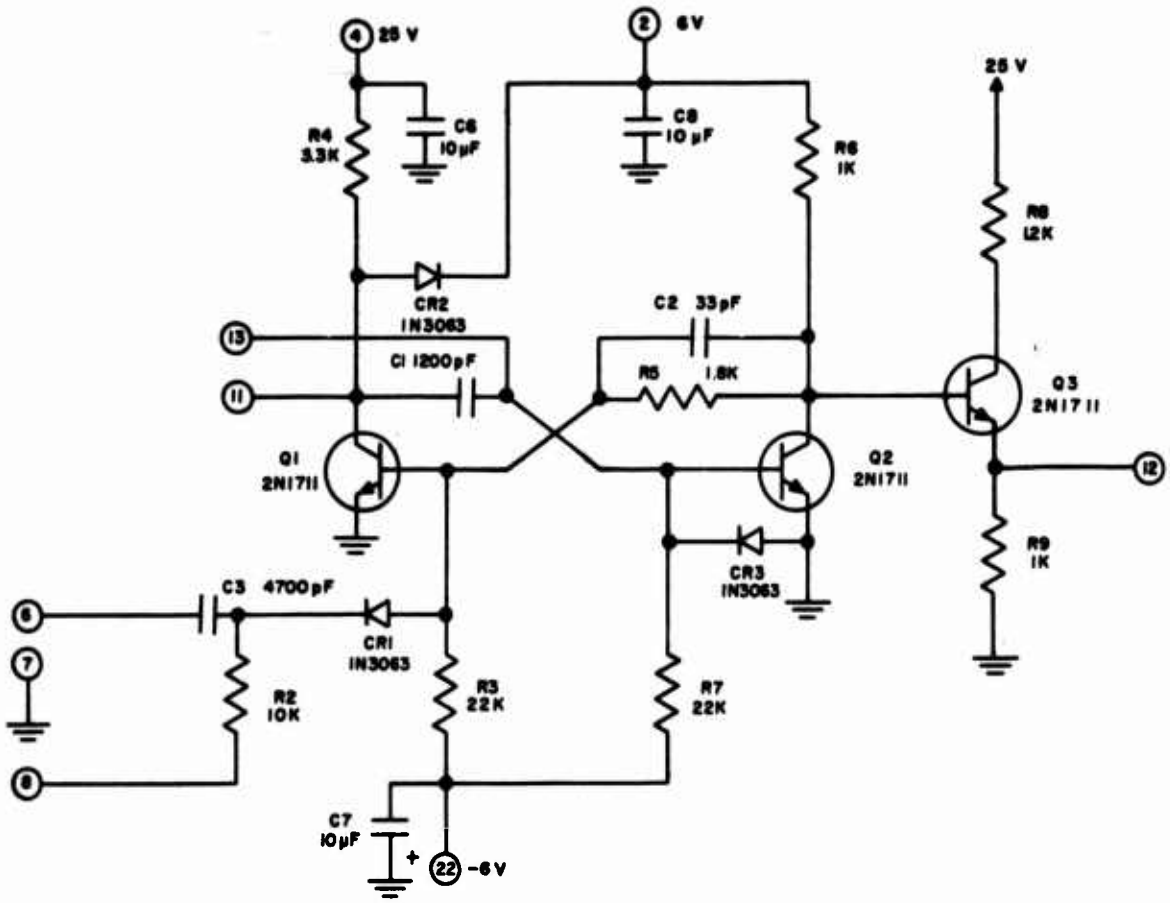
4 25 V
2 6V
25 V
R4 3.3K
C6 10 μF
C8 10 μF
R6 1K
R8 12K
CR2 IN3063
C2 33pF
13
C1 1200pF
R5 1.8K
11
Q3 2N1711
Q1 2N1711
Q2 2N1711
12
R9 1K
CR3 IN3063
C3 4700pF
6
CR1 IN3063
7
R2 10K
R3 22K
R7 22K
8
C7 10μF
+
22 -6V

A4385

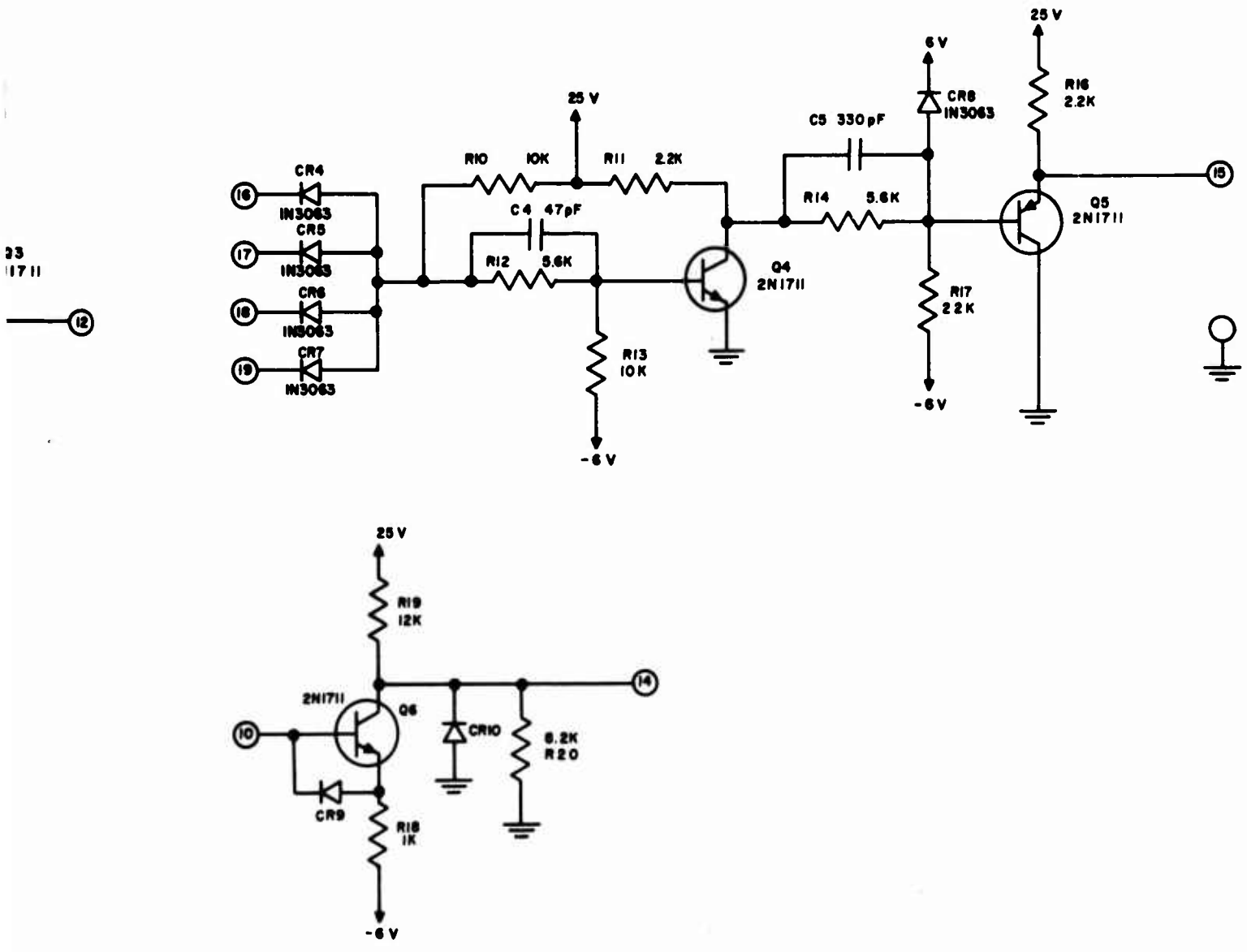

Figure 49. Multivibrator, Four-Input NOR, Level Converter (DSM1A)

2

The third circuit is a level converter which takes a square wave input at pin 10 that varies from -12 V to -2 V and gives an output at pin 14 that varies from 25 V to 0 V.

(7) Delay Gate Generator (DSM2A)

This card consists of two separate delay gate generators for the azimuth-of-arrival modes. The circuits necessary for one mode consist of three monostable multivibrators and two inverter-amplifier circuits (Figure 50). A1, A2, A3, A4, A5, and A6 are flip-flops connected such that they operate as monostable multivibrators with the pulse length determined by the values of the associated resistors and capacitors.

Taking one mode as an example, an input at pin 17 is normally a positive pulse and A1 is triggered by the leading, positive-going edge. The pulse at pin 4 of A1 is a negative-going pulse and the length of the pulse is varied with R1. The trailing edge of this pulse triggers A2, which gives a negative-going pulse at pin 4 and a positive-going pulse at pin 5. The pulse length can be varied with R3. The pulse at pin 5 is inverted and amplified for use as the peak detector gate. The trailing edge of the pulse at pin 4 triggers A3. The positive-going pulse at pin 5 of A3 is inverted and amplified and used as a gate for the boxcar sampling circuit. The pulse length at pin 5 of A3 is varied with R5.

(8) Dual Input NAND (LOA1A)

This card consists of four dual input NAND circuits (Figure 51). If both inputs of a NAND circuit are positive, the output is zero. If one input is zero, the output is positive.

(9) Dual Sample Gate (LOG1A)

The LOG1A card contains dual sample gates which are turned on at the same time (Figure 52). With the voltage at pin 18 at 5 V, the collector of Q2 is held at 6 V by CR8 and CR7, and the collector of Q3 is held at -6 V by CR6 and CR5. This causes all the diodes in the two diode bridges to be back-biased and the diode gates act as open circuits. When the voltage at pin 18 goes to 0 V, the collector of Q2 is held at -6 V by CR4 and CR5, and the collector of Q3 is held at 6 V by CR9 and CR7. This turns all the diode bridges on and the voltage present at the inputs (pins 7 and 9) are also present at the respective outputs (pins 8 and 10). Q1 is an inverter stage.

(10) Peak Detector, Sample Gate, Reset Gate (LOG2A)

LOG2A contains a peak detector, sample gate, and reset gate (Figure 53). The sample gate operates similar to the one described for LOG1A with CR12, CR13, CR14, and

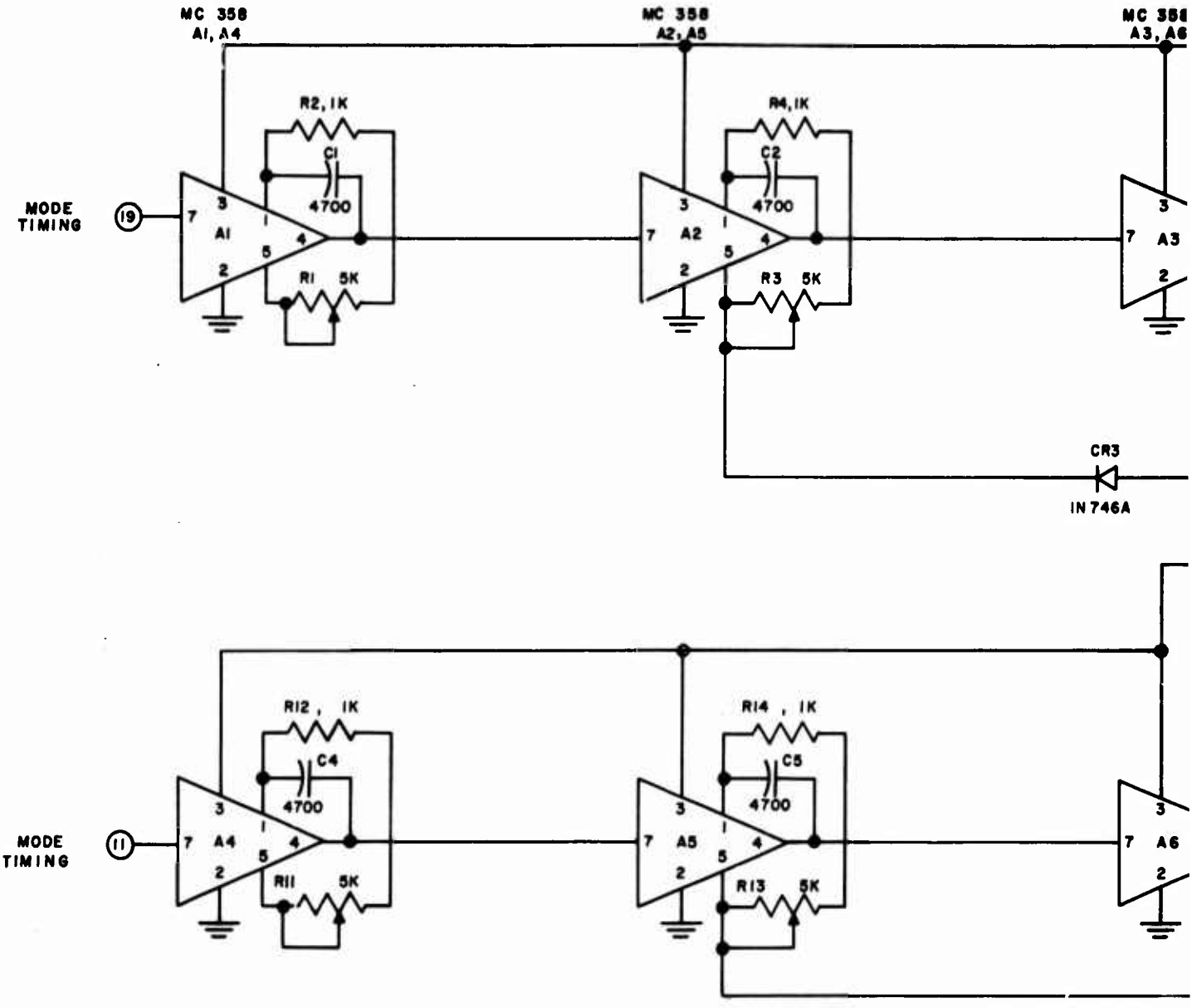
MC 358
A1, A4
MC 358
A2, A5
MC 358
A3, A6
MODE
TIMING
19
R2, 1K
C1
4700
A1
R1 5K
R4, 1K
C2
4700
A2
R3 5K
A3
CR3
IN746A
MODE
TIMING
11
R12, 1K
C4
4700
A4
R11 5K
R14, 1K
C5
4700
A5
R13 5K
A6

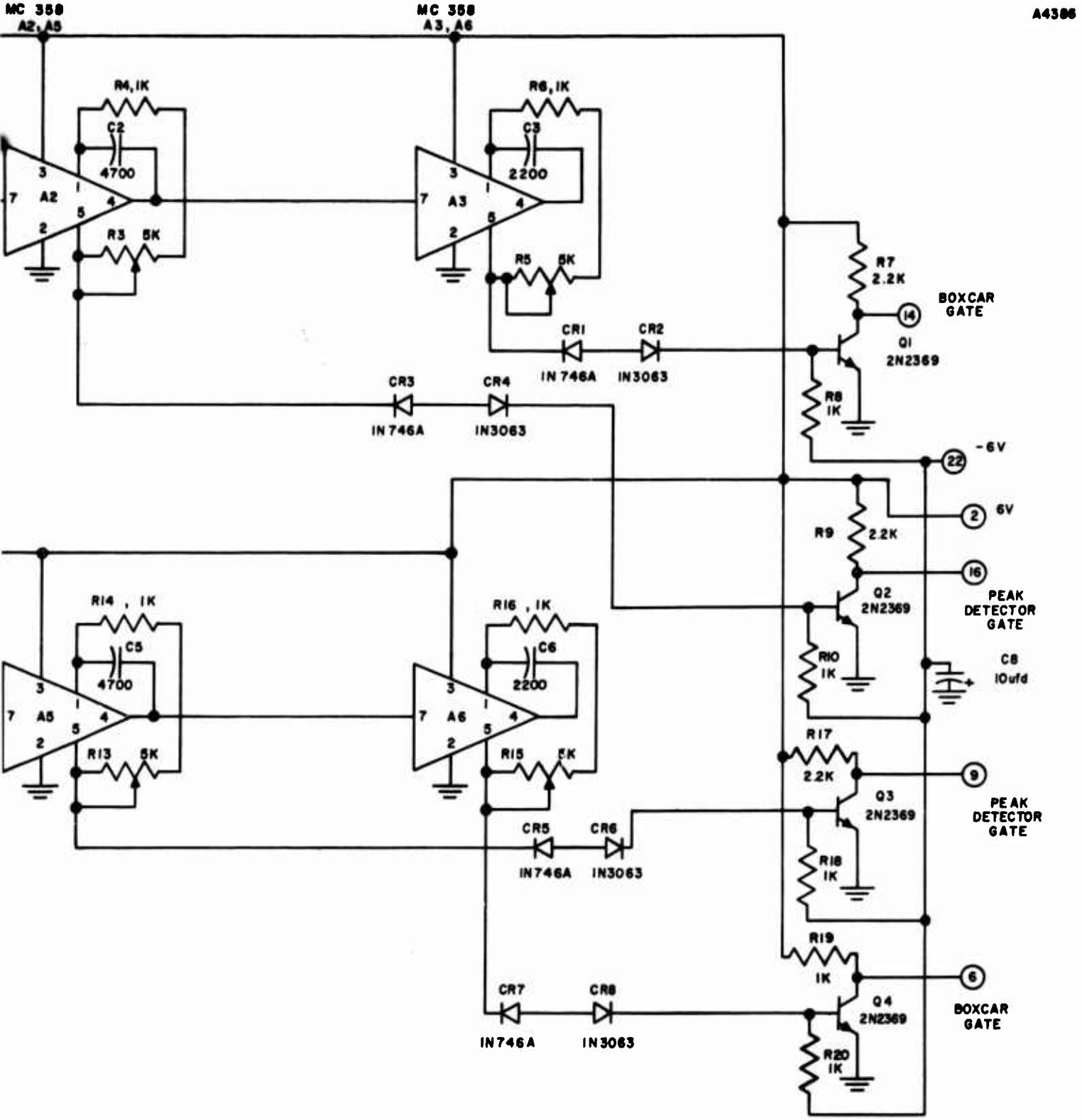

Figure 50. Delay Gate Generator (DSM2A)

1

2

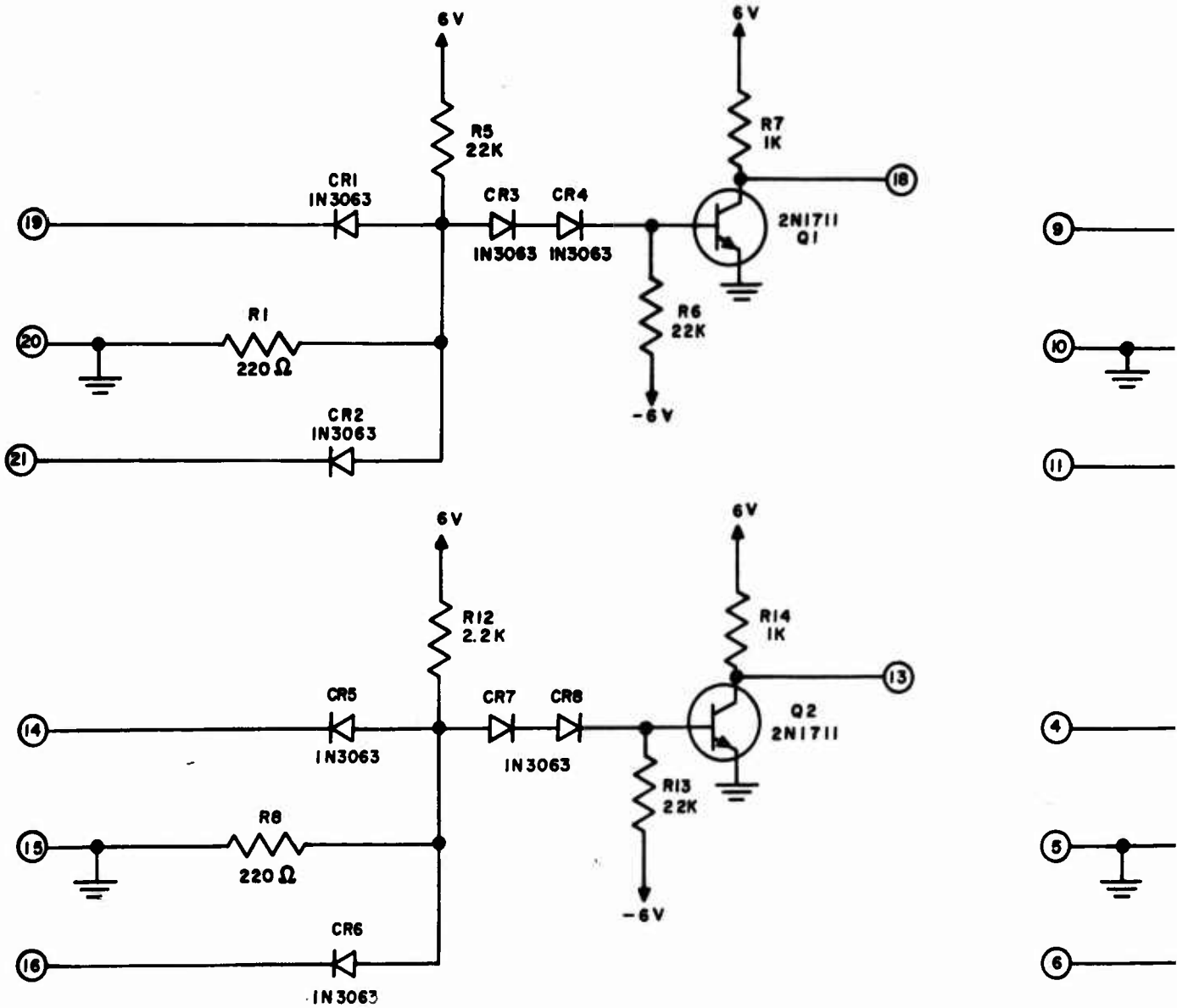
6V
R5
22K
CR1
IN3063
CR3
CR4
IN3063
IN3063
6V
R7
1K
2N1711
Q1
19
18
9
R1
220Ω
20
R6
22K
10
-6V
CR2
IN3063
21
11
6V
R12
2.2K
6V
R14
1K
CR5
CR7
CR8
13
14
IN3063
IN3063
Q2
2N1711
4
R13
22K
R8
220Ω
15
5
-6V
CR6
16
IN3063
6

A4387

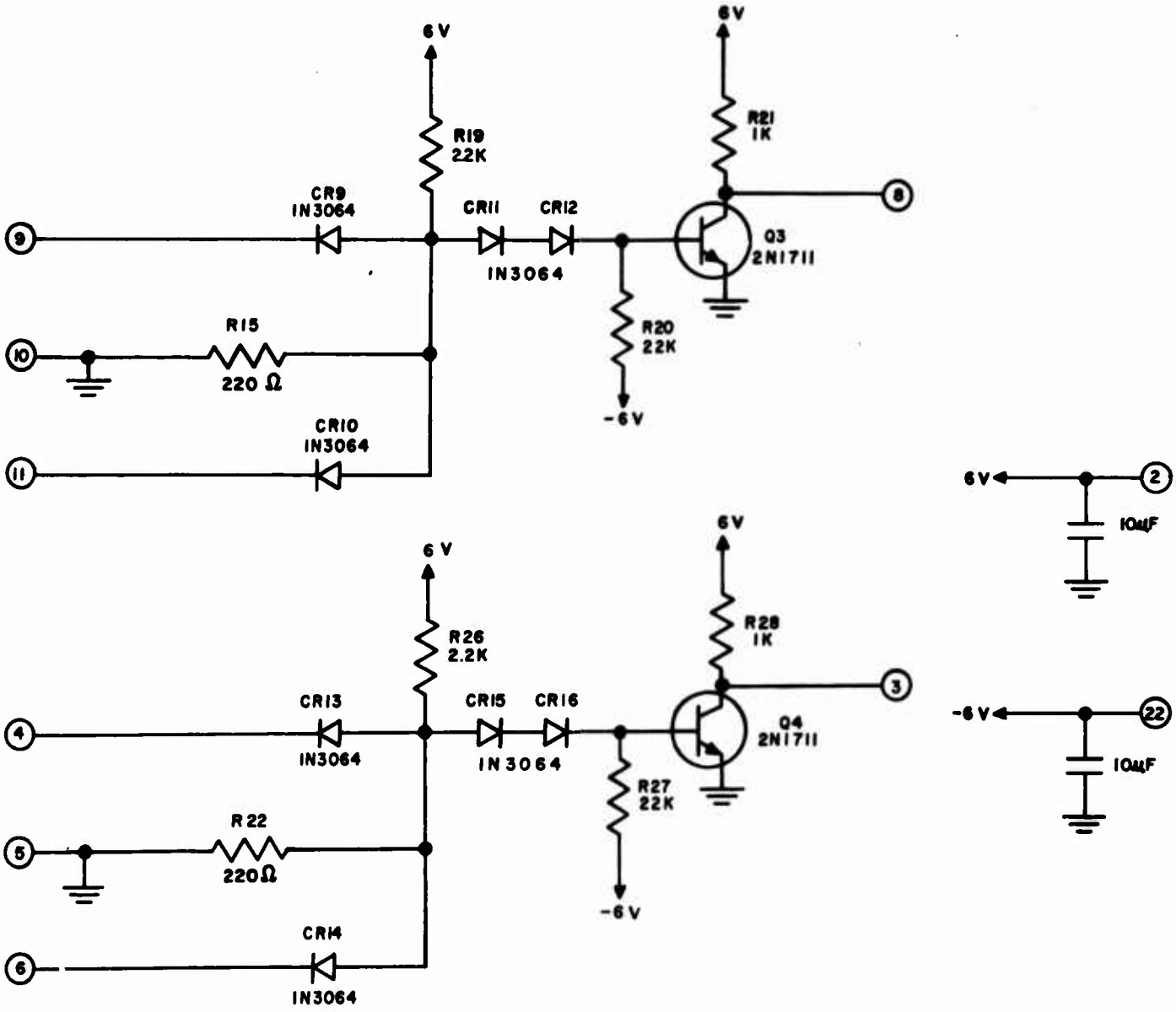

Figure 51. Dual Input NAND (LOA1A)

1

2

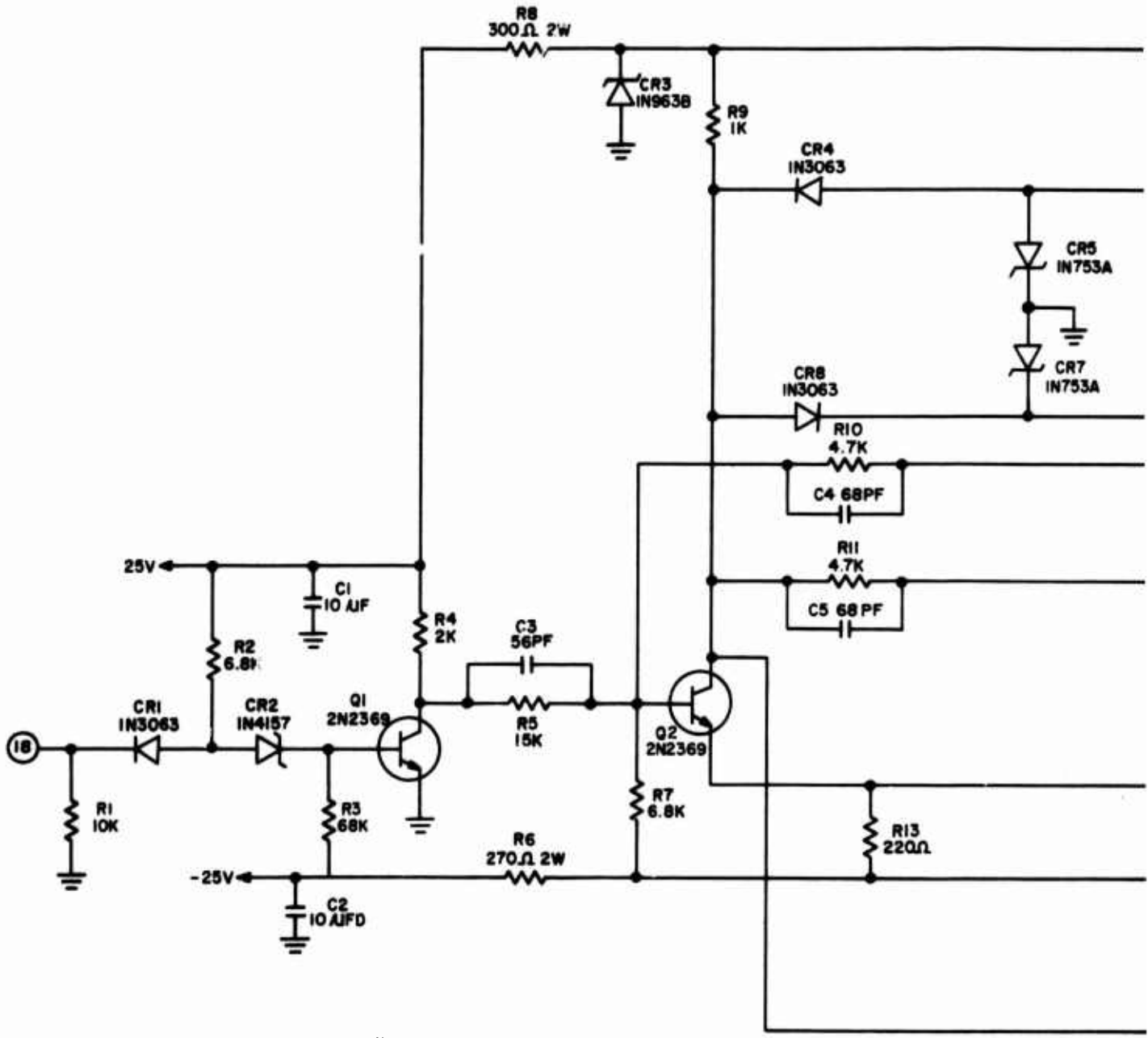
R8
300Ω 2W
CR3
IN963B
R9
1K
CR4
IN3063
CR5
IN753A
CR7
IN753A
CR8
IN3063
R10
4.7K
C4 68PF
R11
4.7K
C5 68PF
25V
C1
10 MF
R4
2K
C3
56PF
R2
6.8K
CR1
IN3063
CR2
IN4157
Q1
2N2369
R5
15K
Q2
2N2369
18
R1
10K
R3
68K
R7
6.8K
R13
220Ω
R6
270Ω 2W
-25V
C2
10 MFD

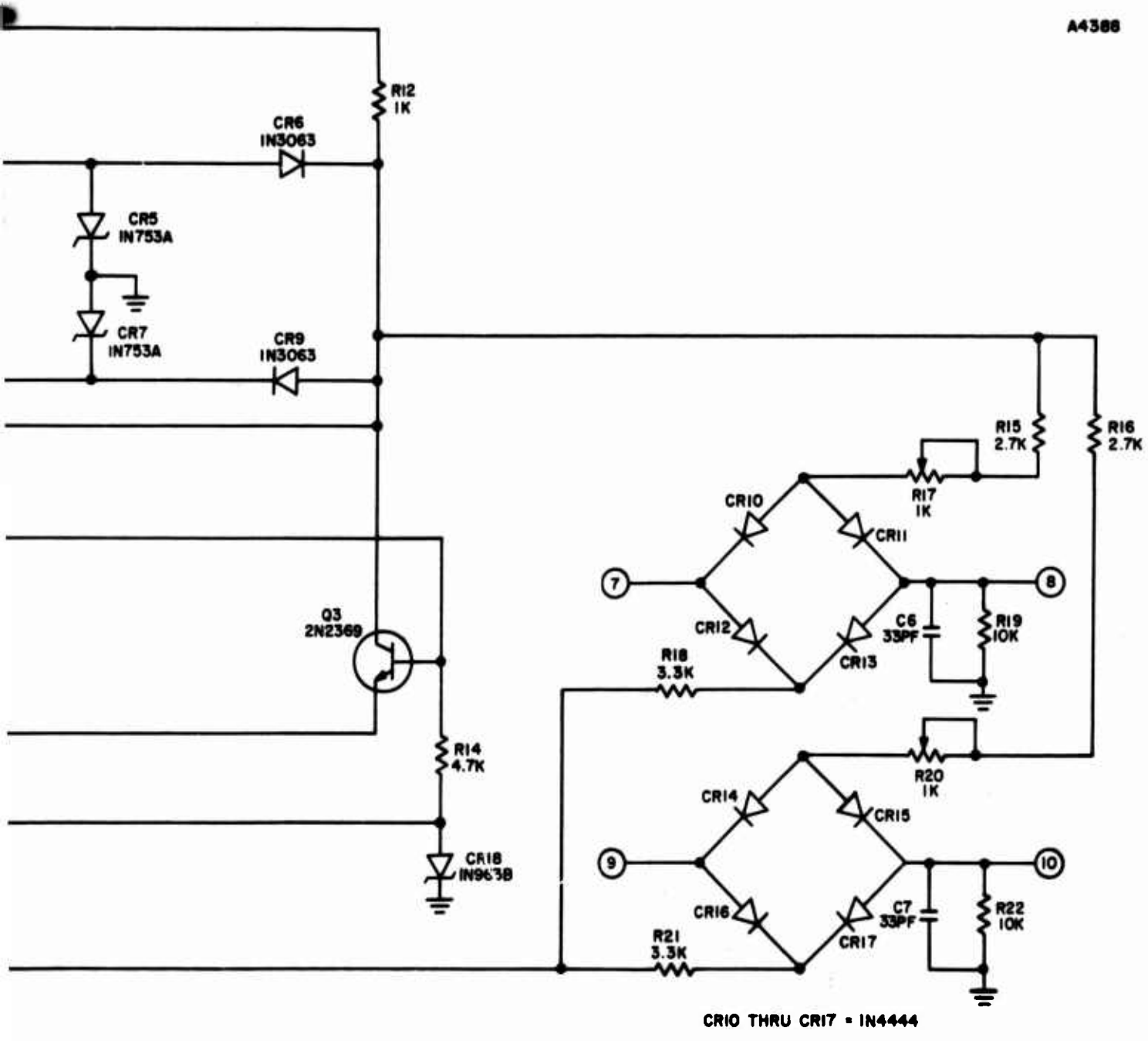

Figure 52. Dual Sample Gate (LOG1A)

2

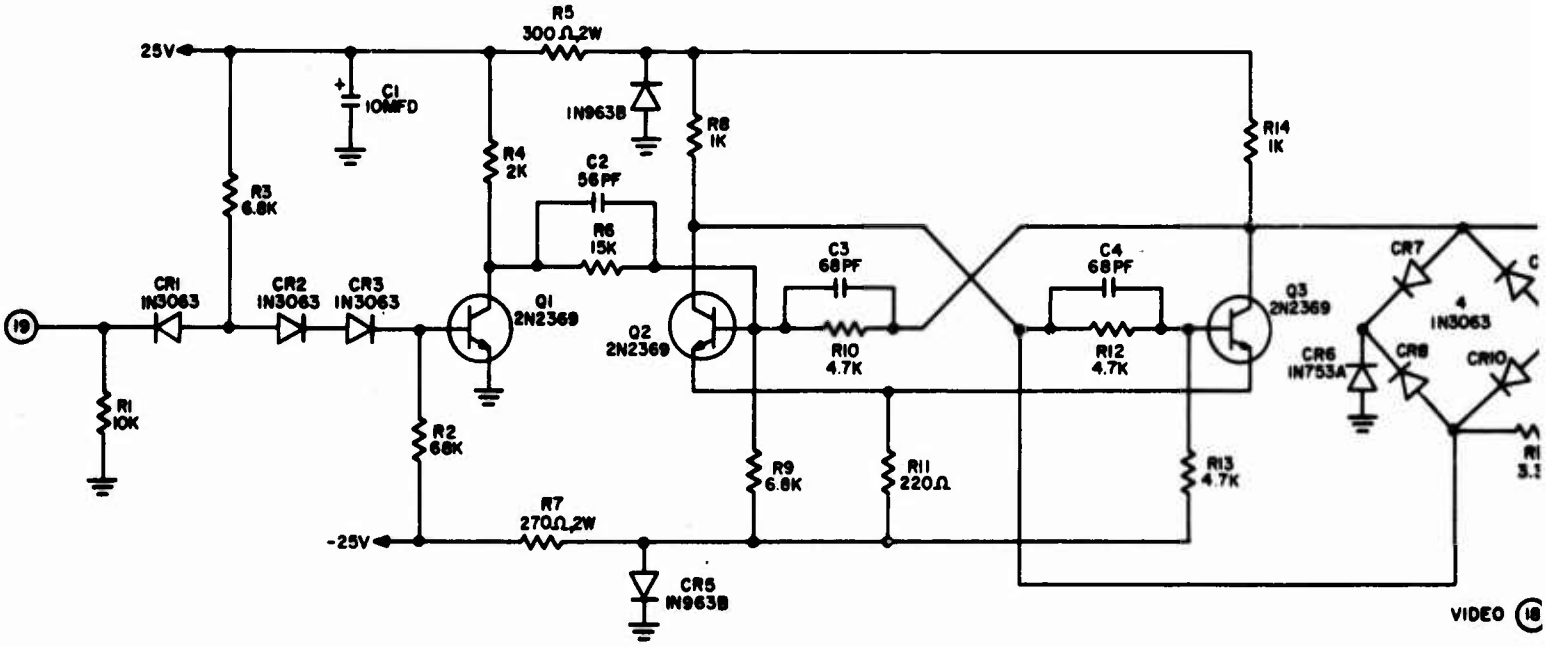
R5
300Ω,2W
25V
C1
10MFD
IN963B
R6
1K
R14
1K
R4
2K
C2
56PF
R3
6.8K
R8
15K
C3
68PF
C4
68PF
CR7
CR1
IN3063
CR2
IN3063
CR3
IN3063
Q1
2N2369
Q2
2N2369
Q3
2N2369
4
IN3063
19
R10
4.7K
R12
4.7K
CR6
IN753A
CR8
CR10
R1
10K
R2
68K
R9
6.8K
R11
220Ω
R13
4.7K
R7
270Ω,2W
-25V
CR5
IN963B
VIDEO 18

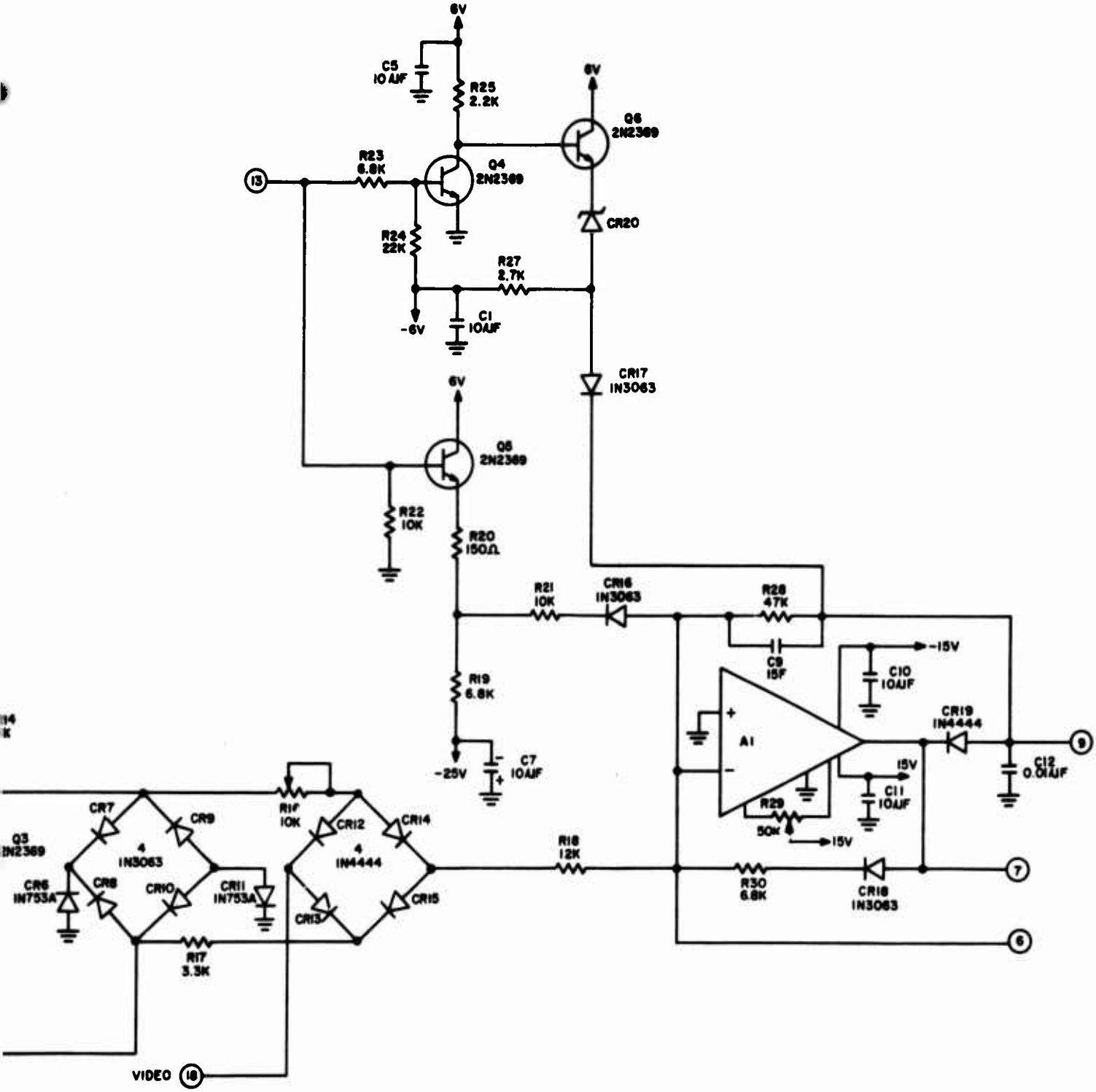

Figure 53. Peak Detector, Sample Gate, Reset Gate (LOG2A)

CR15 being the four-diode gate. The other circuitry on this board consists of an operational amplifier, peak detector, and reset functions which operate similar to circuits described for DEM1A.

(11) Low Pass Filter (NEC1A)

This card (Figure 54) contains the resistors and capacitors necessary to produce a 1-Hz, three-pole low pass filter in conjunction with one section of an AMO2B. The filter contains an active device with positive feedback to produce the three poles.

A4390

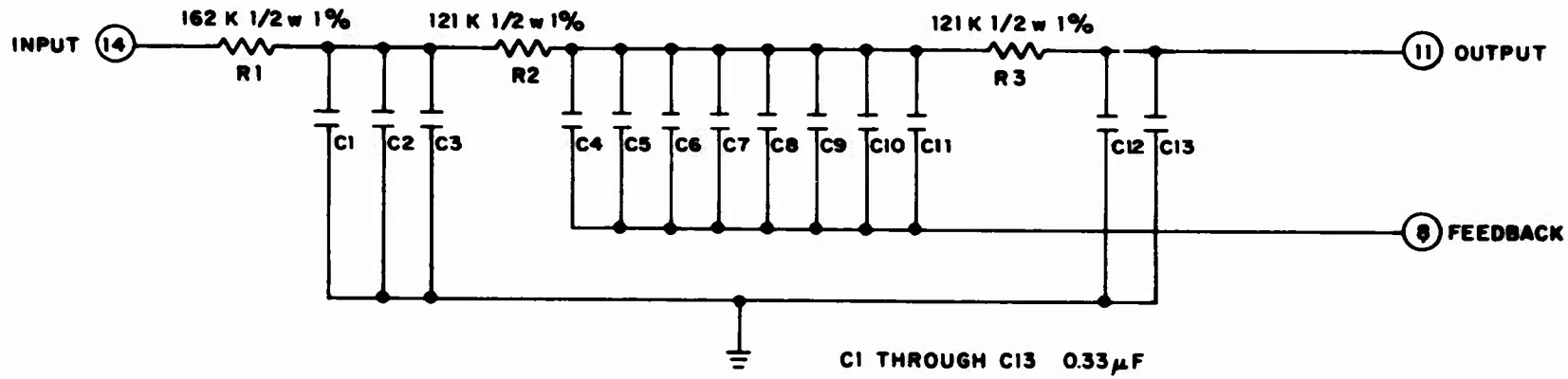

Figure 54. Low Pass Filter (NEC1A)

3. OPERATING INSTRUCTIONS

a. Switch and Dial Positions of Timing Equipment

(1) Tektronix 162: A9

(a)	Operating mode	--	triggered
(b)	Vernier	--	calibrated position
(c)	Waveform duration	--	5.0 ms
(d)	Multiplier	--	1
(e)	Output switch	--	pulse out

(2) Tektronix 163: A3, A5, A7, A11

(a)	Trigger selector	--	negative sawtooth
(b)	Pulse width	--	10 μs
(c)	Pulse width multiplier	--	1
(d)	Pulse amplitude	--	maximum
(e)	Output pulse delay	--	see part b.

(3) Tektronix 163: A4, A6, A8, A12

(a)	Trigger selector	--	positive pulse
(b)	Pulse width	--	10 μs
(c)	Pulse width multiplier	--	1
(d)	Pulse amplitude	--	6 V

b. Timing Adjustments

The delay controls of A11, A7, A5, and A3 are used to adjust for the proper position of the peak detector and boxcar sample gates for modes 1, 2, 3, and 4 respectively.

4. ALIGNMENT PROCEDURES

a. Individual Cards

(1) AMO2 A, B, C, D (Omit steps (b) and (e) for AMO2D)

(a) Ground pins 19, 14, 9, and 4.

(b) Adjust R3, R9, R15, and R21 until the voltages at pins 20, 15, 10, and 5 respectively are 0.000 V dc ±0.001 V.

(c) Remove grounds from pins 19, 14, 9, and 4.

(2) AMO3A

Set R2 and R11 to midrange.

(3) DSA1A

Adjust R9 until pulse at junction of CR1 and CR4 is squared.

(4) LOG1A

(a) Ground pins 7 and 9.

(b) Adjust R17 until pulse offset at pin 8 is minimum and adjust R20 until pulse offset at pin 10 is minimum.

(5) DSM2A

(a) Adjust R5 and R15 for the proper width of the azimuth-of-arrival boxcar gate pulses at pins 14 and 6, respectively.

(b) Adjust R3 and R13 for the proper width of the azimuth-of-arrival peak detector gates at pins 16 and 9, respectively.

(c) Adjust R1 and R11 until the pulses at pins 16 and 9 occur approximately 15 μs later than the pulses at pins 17 and 11, respectively.

b. Channel Alignments

Individual card alignments should be done first and all timing signals must be present.

(1) Mode Loss Receiver Video Channels

(a) Apply 1.010 V ±0.001 V dc to pin 18 of A4 of Module 1.

(b) Adjust R14 of A10 until output on pin 11 of A10 is a representative pulse of the input at pin 6 of A10.

(c) Ground pin 18 of A4.

(d) Adjust R29 of A4 to midrange.

(e) Adjust R16 of A4 for zero at pin 20 of A29.

(f) Adjust R10 of A14 for zero at pin 15 of A29.

(g) Apply 1.000 V ±0.001 V dc to pin 18 of A4.

(h) Adjust R2 of A29 until voltage at pin 20 of A29 is 10.000 V ±0.010 V dc.

(i) Adjust R8 of A29 until voltage at pin 15 of A29 is 10.000 V ±0.010 V dc.

(j) Steps (a) through (i) should be repeated for the three remaining video channels, using the appropriate A and R numbers.

(2) Mode Loss Receiver, 25-Hz Channels

The alignment of the mode loss receiver 25-Hz channels is identical to that for the mode loss receiver video channels except step (f) and (i) are omitted and the voltage in step (h) would be 5.000 V ±0.010 V dc.

(3) Azimuth-of-Arrival Channels

(a) Set R16 and R23 of A3 in Module 2 to midrange.

(b) Ground pins 7 and 9 of A1.

(c) Adjust R25 of A3 until voltage at pin 20 of A21 is 0.000 V ±0.010 V dc.

(d) Apply 0.340 V ±0.001 V dc to pins 7 and 9 of A1.

(e) Adjust R16 of A3 until voltage at pin 20 of A21 is 0.000 ±0.010 V dc.

(f) Ground pin 7 and apply 0.175 V ±0.001 V dc to pin 9 of A1.

(g) Adjust R25 of A3 until voltage at pin 20 of A21 is 0.000 V ±0.010 V dc.

(h) Ground pin 9 and apply 0.175 V ±0.001 V dc to pin 7 of A1.

(i) Adjust R2 of A21 until voltage at pin 20 of A21 is 3.750 V ±0.010 V dc.

(j) For the three remaining azimuth-of-arrival channels, repeat steps (a) through (i) using appropriate A and R numbers.

SECTION V

AZIMUTH OF ARRIVAL

1. EXPERIMENT DESIGN

In brief, the azimuth of arrival experiment is designed to compile data which will depict the statistical behavior of the azimuth of arrival for various modes over long (2000 nmi) propagation paths. These results will then be correlated with seasonal variations, dawn-dusk transitions, and other natural phenomena as well as with the data from other experiments being performed on this program. These statistical results will then be used to predict the behavior of the ionosphere in order to optimize HF radar detection. A more detailed discussion of the experiment design may be found in Interim Report No. 2 on this program, pp. 39-48.

With these objectives in mind, and knowing what equipment was available at the beginning of this program, two important sources of error due to external phenomena need to be considered. This will enable the experiment system designer to place further specifications on the instrumentation for this experiment. These include the stationarity of the environment over the measurement interval and the peak signal to rms noise ratio at the input.

a. Signal Stationarity

Velocities in the ionosphere have been investigated by several authors. Manning and Eshleman (Ref. 1) report near maximum values for winds in the E layer as 70 m/sec. Booker and Crain (Ref. 2) give the neutral acoustic velocity due to a traveling disturbance as 700 m/sec. Briggs (Ref. 3) states that the drift velocity in the F region is up to 100 m/sec. AFCRL (Ref. 4) reports measurements made at Puerto Rico as indicating mean values about 70 m/sec with 96 percent confidence value at 400 m/sec.

Assume the following model

The actual angle is given by $\phi = \tan^{-1} \frac{\ell}{R}$. For small angles of arrival

$$\phi = \frac{\ell}{R} \text{ in radians}$$

Since ℓ is a function of time, so will ϕ be,

$$\text{or } R \times \phi(t) = L - vt$$

$$\text{or } \phi(t) = \frac{L}{R} - \frac{v}{R} t$$

Differentiating yields the rate of change of angle given by

$$\frac{d}{dt} [\phi(t)] = \phi'(t) = - \frac{v}{R}$$

For the 2E mode, the near maximum value given above is 70 m/sec. The half-hop range is 1000 km. Therefore, $\phi'(t) = -0.004$ deg/sec. For the 1F2 mode the neutral acoustic velocity is v = 700 m/sec and R is 2000 km.

$$\phi'(t) = -0.02 \text{ deg/sec}$$

To keep the resulting error due to stationarity in the worst case (F region) to a maximum of 1° (±0.5°), the maximum acceptable accumulation interval is $\frac{1}{0.02}$ = 50 seconds. Instrumentation system parameters reduce this further to a convenient 40 seconds. For this interval the resulting errors are

2E mode = 0.16° or ±0.08°
1F2 mode = 0.8° or ±0.4°

Thus, the maximum expected error would be ±0.4°. As stated in references 3 and 4, a more typical figure would be that represented by the drift velocity in the F region reported as 100 m/sec. This yields an error of ±0.057°.

b. Peak Signal to rms Noise Error

In analyzing the effect of the signal-to-noise ratio (SNR) on the accuracy of determining the azimuth of arrival, the following factors must be considered: (1) the frequency of measurement, (2) the integration (accumulation) interval, and (3) the antenna spacing. The accumulation interval has already been determined from stationarity considerations as 40 seconds. Likewise, the frequency of existing equipment is 800 kHz. The antenna spacing was a compromise between the large spacing desired for high angle sensitivity and the requirement that the two elements have high sum gain. Two-thirds wavelength was selected and corresponds to a mechanical to electrical conversion factor of 4.17 to 1.

Consider the noise to be a random vector rotating about the end of the signal vector. The noise component that is normal to the signal vector will be the only source of error. By the trigonometry of the problem the resulting rms electrical phase error is given by

$$\epsilon_{SNR} = \cot^{-1}\left[\frac{E_{signal}\ (peak)}{N_{noise}\ (rms)}\right]$$

and for good SNRs (>10 dB)

$$\epsilon_{SNR} = \frac{(57.3)}{SNR} \text{ in degrees}$$

This analysis results from investigating the following model

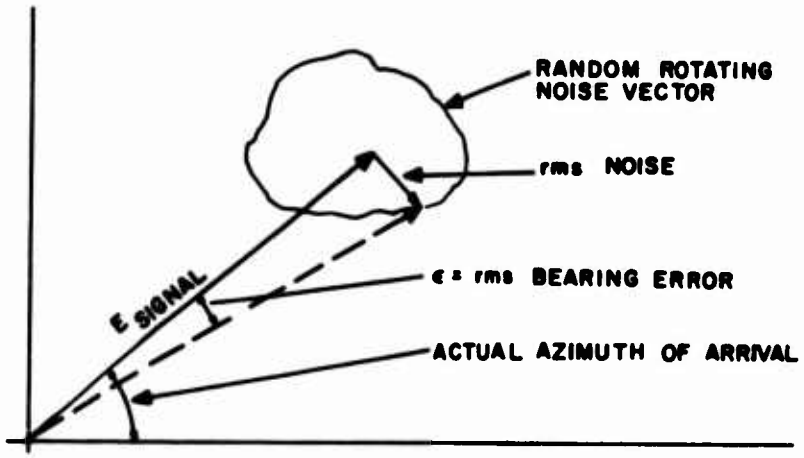

Accumulating n samples of E_{signal} in N_{noise} results in enhancing the certainty with which the actual azimuth of arrival can be determined. In essence, accumulating n samples of E_{signal} results in $n \times E_{signal}$ strength or $\frac{n \times E}{n}$ average signal strength. Accumulating n samples of random noise results in a distribution characterized by $\frac{\sigma^2}{n}$ explicitly given by

$$\text{Noise} = (n)\ \frac{1}{\sqrt{\pi}\ \frac{\sigma}{\sqrt{n}}}\ \exp\left[-\frac{1}{2}\ \frac{(N_{mean} - \sigma)^2}{n}\right]$$

or with respect to N_{mean}

$$\text{Noise} = \frac{1}{\sqrt{\pi}\ \frac{\sigma}{\sqrt{n}}}\ \exp\left[-\frac{1}{2}\ \frac{\sigma^2}{n}\right]$$

The resulting distribution, centered about E_{signal} is given by

$$SNR = \frac{n\,E_{signal}}{\frac{1}{\frac{\pi\sigma}{\sqrt{n}}}\exp\left[-\frac{1}{2}\frac{\sigma^2}{n}\right]} = \sqrt{n}\,\frac{E_{signal}}{\frac{1}{\pi\sigma}\exp\left[-\frac{1}{2}\frac{\sigma^2}{n}\right]}$$

or the peak SNR has been improved by $\sqrt{n}$ and the rms error by $\sqrt{n}$. The new error is given by

$$SNR = \frac{57.3}{\sqrt{n}\ (SNR)} \text{ in degrees}$$

where $\begin{cases} n = \text{number of samples} \\ SNR = \text{old SNR ratio} \end{cases}$

$$SNR = \frac{18.1°}{\sqrt{n}} \qquad (SNR = 10\ dB)$$

For SNR = 10 dB, n = 4000, the one sigma error is 0.285 electrical degrees. For a confidence factor of 96 percent (3σ) and the given antenna spacing, the ϵ_{SNR} becomes ±0.206°. Note that for SNR = 20 dB, ϵ_{SNR} becomes ±0.065°.

c. Combined External Errors

The two types of errors discussed above combine as the square root of the sum of the squares and result in a worst case error of $\sqrt{(0.4)^2 + (0.206)^2} = \pm 0.450°$. If the more typical value is used for the velocity in the F region the combined error is ±0.208°.

These errors are combined with the experiment equipment generated errors in Section V-4.

2. HISTORY

The basic azimuth of arrival instrumentation was developed in 1964 under RADC contract AF30(602)-3198 for OHD making use of Phantom pulse compression communications equipment. In 1965 this equipment was assigned to Little IDA to be evaluated for use in measurement of natural azimuthal deviations. A description of the initial azimuth of arrival equipment is contained in Interim Report No. 5 on Dispersive Characteristics of the Ionosphere, pp. 86-103. Also contained is a report on the aircraft flight tests conducted to calibrate this equipment.

These tests successfully calibrated the equipment, so data taking was begun using an oscilloscope and a frame camera as the recording devices. Although these pictorial records revealed some very wide short term variations, by careful examination of the records, periods of "good data" could be identified and reduced. This permanent record form (i.e.,

a series of frame pictures) however, was extremely time consuming to reduce. This made it difficult to reduce enough data for a base from which to draw valid conclusions. To alleviate this condition, a boxcar Sanborn pen recorder combination was set up for each of the four modes of propagation. The result of this change was that although data reduction was now less time consuming, it became evident after a period of data collection that it was now extremely difficult to identify "good" data from that which was invalid because the gate was off the center of the pulse or because the SNR was too low.

The results of experiments run using this method revealed both large off-boresight signals and wide variations of the azimuth of arrival. Continued investigation of the possible cause of these phenomena revealed that these apparent variations were present even when a single antenna was connected to both channels. Both the tapped delay lines (matched filters) and the receivers were investigated as the possible source of this error. The delay lines were carefully realigned for best performance. During this process, tests showed that the apparent angle measured was extremely sensitive to the gate position on the pulse. Correct results were obtained at the peak of the pulse, but serious errors soon appeared as the gate was moved off the center. It was evident that the characteristics of the received signals from our remote sites would preclude the operators from adequately tracking the modes under these restrictions. Investigation of the cause of the critical gate setting showed that the time response of the two receivers (although of identical design) was sufficiently different to produce the effect described as the pulse shifted in the gate.

In summary then, the basic source of the problem was a phase mismatch between the two pulse compression receiver chains resulting in extreme gate position sensitivity. Unfortunately, apparent good results during certain times depended on operator care, and ionospheric conditions precluded an early identification of this problem.

3. NEW APPROACH TO AZIMUTH OF ARRIVAL

To overcome the criticalness of gate position setting caused by the phase mismatch associated with the two receiver chain approach to azimuth of arrival, various techniques were investigated to eliminate this difficulty. This led to an in-depth investigation into sequential pulsing techniques whereby only one receiver chain is used.

The two most prominent candidates were the scanning oscillator approach (see Figure 55) and the delay line approach (see Figure 56). In reality, the scanning oscillator approach was but a quick alternative to the delay line approach. In both techniques, only one receiver chain would be used and it would be switched from one antenna of the interferometer pair to

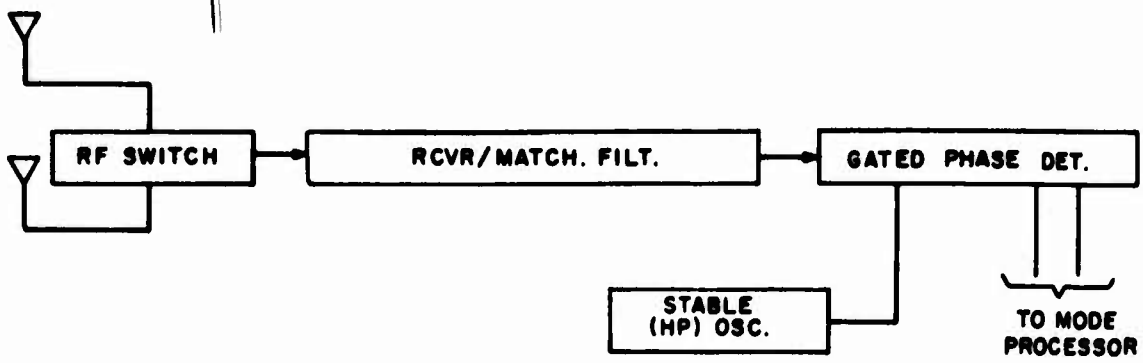

Figure 55. Block Diagram of Scanning Oscillator

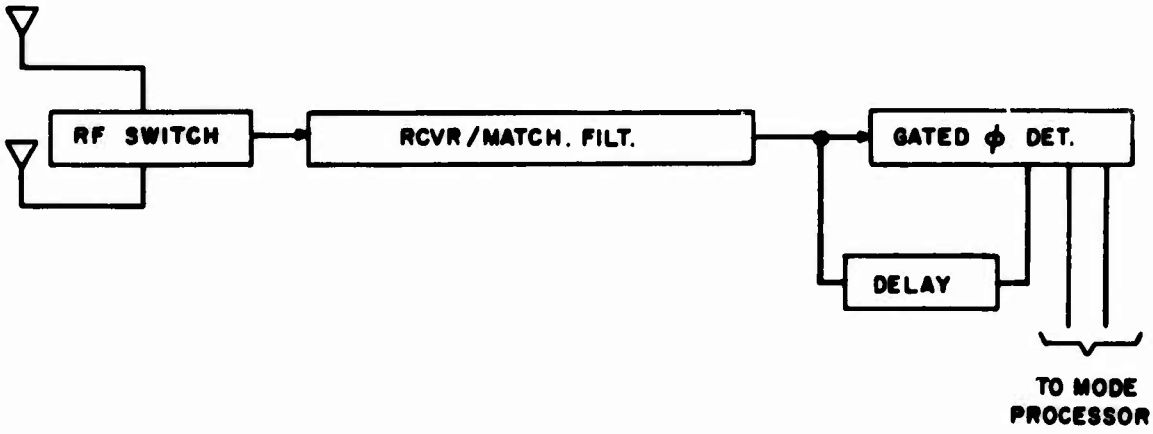

Figure 56. Block Diagram of Delay Line Approach

the other antenna of the interferometer pair. Thus, the output of the receiver would sequentially contain antenna A and antenna B information. The azimuth of arrival information is contained in the relative phase of successive signals. The most obvious way of demultiplexing would be to compare a return with the return that occurred 5 ms earlier (accomplished by delaying the preceding signal 5 ms). This undelayed and delayed pair, when presented to the gated phase detector, will yield the azimuth of arrival information. Since a suitable delay line was not available for verification of the sequential pulsing technique, an alternate scheme was derived: the scanning oscillator approach. Here, the delay line was replaced by a stable frequency generator (HP synthesizer) at a small offset from the IF. The demultiplexing was provided by a modified mode processor. The result was a pair of outputs for each mode with each output rotating through all possible phases. By comparing the two signals (differencing), the relative phase was extracted. However, this technique requires a method for performing this difference, results in less integration gain, and a proportionately higher error for the same SNR. It did provide data that were consistently close to boresight -- with a rather narrow distribution. Samples of the Sanborn recordings for the scanning oscillator approach are shown in Figures 57 and 58.

The scanning oscillator technique provided a breadboard verification that the delay line technique would work. The delay line technique, however, had two important advantages. The output from the phase detector was in the same format as before and, hence, required no new processing before recording. Also, the technique proved just as fast to implement. Hence, this technique is being implemented and the results will be discussed in the next report.

4. ERROR ANALYSIS

It is important to define the characteristics and sources of errors that will contaminate the azimuth of arrival data. Since data will be compiled in a statistical fashion, it will behoove us to identify the statistical parameters governing the errors associated with azimuth of arrival. The end result of this error analysis is to be able to predict the degree of confidence in the data.

Typically, 100 x 40 samples of data (4000) will be accumulated. If all samples are independent members of a normal population, an effective integration gain of 63.4:1 will be achieved. This says, for example, that if each sample may occur with a standard deviation of 5°, then the effective standard deviation of the entire 4000 samples will be 0.079°, or the mean of the distribution can be predicted within 0.23° with 96 percent confidence.

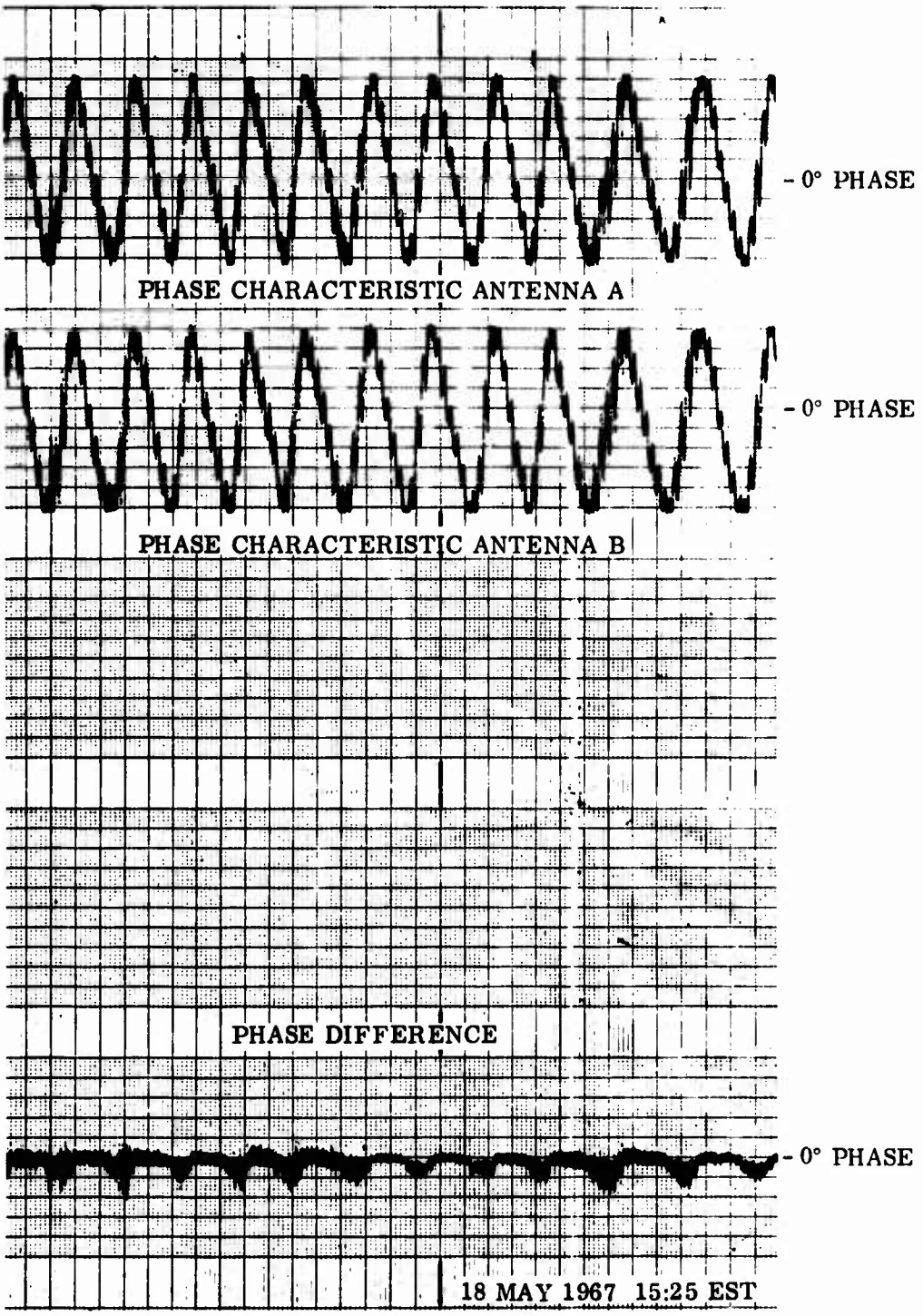

Figure 57. Azimuth of Arrival, Coco Solo Path

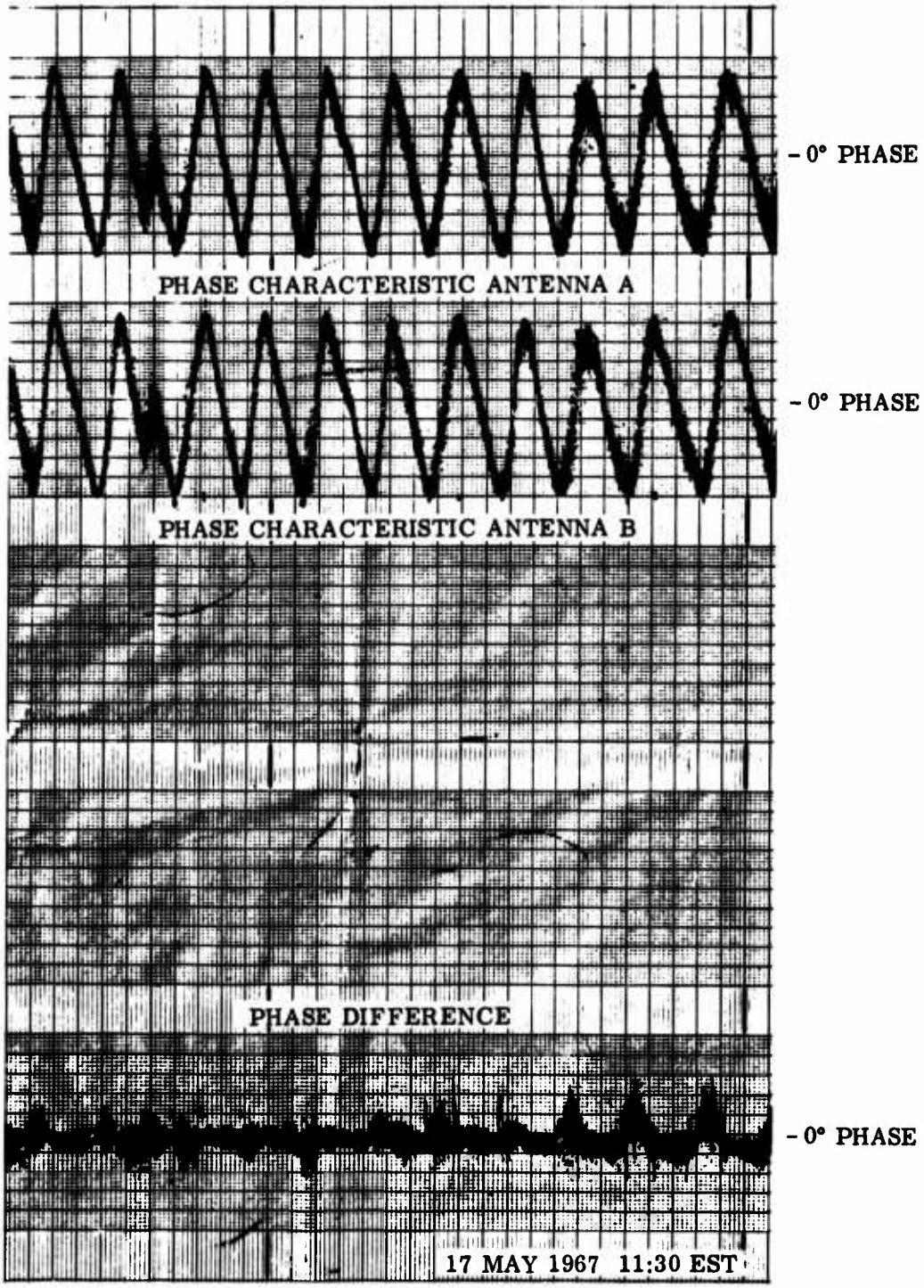

Figure 58. Azimuth of Arrival, Thule Path

The errors that can influence the azimuth of arrival accuracy are: (1) the peak signal to rms noise ratio of each sample, (2) the stationarity of the environment, (3) the change in phase introduced by doppler offset coupled with 5 ms delay between the two signals being detected, and (4) the one channel signal to spurious ratio of the delay line. The impacts of the first two were previously discussed, but will be statistically summed with the other errors derived below to obtain the overall expected accuracy.

a. Doppler Offset Error

The delay line technique requires that the phase of one signal be compared with the phase of one received (and delayed) exactly 5 ms earlier. If the IF is precisely 800 kHz and there is no angle deviation, this is an integer number of IF cycles. If, however, there is a doppler offset, there will be a phase change introduced by this offset.

To calculate the error associated with this phenomena, assume the undelayed output is given by

$$\cos [\omega(t) + \phi_2]$$

and the delay line output by

$$\cos [\omega(t + \tau) + \phi_1]$$

The desired phase information is given by

$$\phi = \phi_2 - \phi_1$$

However, the time delay makes this look like

$$\phi = \phi_2 - \phi_1 - \omega\tau = \phi_2 - \phi_1 - \epsilon_D$$

where

ϵ_D = error introduced by the time delay and doppler

Now

$$\omega = 2\pi \times 800 \times 10^3 + \Delta_D$$

where

Δ_D = doppler offset in Hz

Then

$$\epsilon_D = [2\pi \times 800 \times 10^3 + \Delta_D]\ \tau$$

Since $2\pi \times 800 \times 10^3 \times \tau$ is an integer number cycles of phase the error is given by

$$\epsilon_D = \Delta_D\ \tau \times 360 \text{ in degrees}$$

The maximum error is given by

$$\epsilon_{D_{max}} = 1.8\ \Delta_{D_{max}}$$

The doppler is being measured as a part of the spectrum experiment. Results thus far indicate measured doppler on the order of 0.01 to 0.1 Hz. Earlier work using CW instead of Phantom pulses reported up to 0.3 Hz. However, simple calculations based on rate of change of ionospheric height indicate dopplers up to several cycles may occur. Taking all of this into account, a maximum expected doppler of 0.5 Hz has been selected. This implies an electrical error of 0.9 degrees and an azimuth error of 0.215°.

b. Delay Line Errors

(1) Signal to Spurious Error

The delay line manufacturer has guaranteed the spurious to be at least 30 dB below the signal level. By the same analysis as for external noise, this would correspond to an electrical error of

$$\epsilon_{DL1} = \frac{1}{30}\ (57.3) \text{ electrical} = 1.91 \text{ degrees}$$

with an antenna conversion factor of 4.17:1

$$\epsilon_{DL1} = 0.457 \text{ degree actual (one } \sigma)$$

Since the spurious is noise-like in nature (may be at any random angle), accumulating 4000 samples would result in 96 percent confidence rms error contribution of

$$\epsilon_{DL1} = 0.022 \text{ degree actual}$$

(2) Error Due to Time Delay Drift in Delay Line

Assume the delay line temperature to vary uniformly between $T + \tau$ and $T - \tau$. For a temperature coefficient for the delay line of 1×10^{-6}/°C, the time delay change for a control of $\pm\tau$ and a line length of 5×10^{-3} sec would be $\pm 5 \times \tau \times 10^{-9}$ sec or $\pm 5 \times \tau$ ns. Thus, a temperature excursion of 0.5°C yields a time delay excursion of 2.5 ns which corresponds to a phase error of

$$\epsilon_{DL2} = \frac{2.5 \times 10^{-9}}{1.25 \times 10^{-6}} \times 360 = 0.72 \text{ degree electrical}$$

Dividing by the antenna conversion factor of 4.17:1 yields

$$\epsilon_{DL} = 0.173 \text{ degree actual}$$

This error is systematic in nature and represents a bias error in the readings. This is due to the fact that the oven on the delay line cycles at a rate comparable to the integration interval (40 seconds) and the phase error over a 40-second interval may be described as shown below.

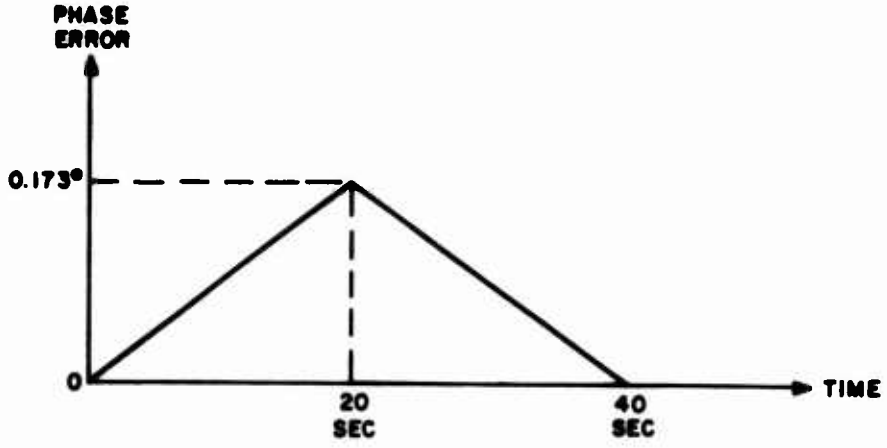

An error curve like this over the interval would yield a bias error on the distribution comparable to the center of gravity of ±0.055° or if the error is more sinusoidal in nature than the error would be ±0.11°. Since sometimes the errors would be equally distributed about zero error, this approximation is not unreasonable, and we will use for the error ±0.083° (average of the two presented).

(3) Error Due to Dispersion in the Delay Line

Dispersion in the delay line results in a mismatch between the delayed and undelayed channels. This mismatch may be represented by a pulse R dB below the desired pulse. This pulse contaminates the measurement of the relative phase between the two signals and presents an error to our measurement. The mismatch signal is probably a combination of systematic and random errors. However, a systematic error of this nature is one that may be calibrated out and at worse it is a vector normal to the signal vector and produces an error given by:

$$\epsilon_{DL3} = \frac{1}{4.17} \cot^{-1}(R) \qquad R = \text{cancellation ratio}$$

For R = 26 dB

$$\epsilon_{DL3} = 0.687°$$

If this error were entirely random in nature (from a uniform distribution) a collection of

4000 samples would yield a normal distribution with a variance given by

$$\sigma^2 = \frac{1}{3}\left[\frac{1}{4000}\right] (0.687)^2$$

and for the 96 percent confidence requirement we have

$$3\sigma = \frac{3}{63.4} (0.687) = 3.27 \times 10^{-2} = 0.0327°$$

The nature of the residue is to consist of quite a few significant phasors which would be a function of the doppler frequency (effect of dispersions depends on exact frequency of pulse) and its precise effect on the measurement is difficult to determine except to say that is probably lies between ±0.0327° and ±0.687°. By the time full scale data collection begins, this error will be assessed and its impact on the system error incorporated.

c. Summary of Errors

Table VII summarizes all errors discussed in tabular form. If a worst case is assumed (i.e., acoustic velocity in F region, SNR = 10 dB, doppler offset = 0.5 Hz, all delay line errors maximum with the exception that the unknown dispersion error is assumed random), then the statistical addition of these errors results in an rms error of ±0.51°. If the F mode drift velocity is used in place of the acoustic velocity the rms error total is reduced to ±0.32°.

TABLE VII

ERRORS ASSOCIATED WITH AZIMUTH OF ARRIVAL

Error	Case	Variance	
		Single Pulse	Integrated
Stationarity	E Mode drift	0.08°	0.08°
	F Mode acoustic	0.40°	0.40°
	F Mode drift	0.057°	0.057°
SNR	SNR = 10 dB	4.35°	0.206°
	SNR = 20 dB	1.37°	0.065°
Doppler offset	Doppler = 0.5 Hz	0.215°	0.215°
Delay line	Signal/spurious	0.437°	0.022°
	Time delay drift	0.083°	0.083°
	Dispersion-random	0.687°	0.0327°
	Dispersion-systematic	0.687°	0.687°

d. Conclusions

The delay line approach has been implemented at Starr Hill and initial testing corroborates the expectation of success. The effect of temperature on the delay line is a time delay error of only 1×10^{-9} second for 14 hours.

Both system oriented and experimental errors have been analyzed and the impact on the azimuth of arrival has been calculated. The azimuth of arrival equipment is ready to test against actual signals. Results will be reported in the Seventh Interim Report.

APPENDIX

NOISE TRANSFER IN MIXERS

A. THEORY

The output voltage or current of any device may be represented approximately by a power series expansion of its input as follows.

$$e_{out} = A_0 + A_1 e_{in} + A_2 e_{in}^2 + \ldots + A_n e_{in}^n \tag{1}$$

The number of terms required to express the output to any given degree of accuracy depends on the degree of nonlinearity in the device transfer characteristic. Ideally, in an amplifier, all A coefficients should be zero, except for A_1. In an ideal mixer, on the other hand, all coefficients except A_2 would be zero.

Assume now a mixer which, for simplicity, can be adequately represented by the first three terms of its power series expansion.

$$e_{out} = A_0 + A_1 e_{in} + A_2 e_{in}^2 \tag{2}$$

Assume, further, that the input voltage consists of two sinusoids simultaneously applied

$$e_{in} = e_s + e_{LO} \tag{3}$$

where

e_s is the input signal voltage

e_{LO} is the local oscillator (LO) voltage

Substituting Equation (3) into Equation (2)

$$\begin{aligned} e_{out} &= A_0 + A_1 (e_s + e_{LO}) + A_2 (e_s + e_{LO})^2 \\ &= A_0 + A_1 (e_s + e_{LO}) + A_2 (e_s^2 + 2e_s e_{LO} + e_{LO}^2) \end{aligned} \tag{4}$$

Now, if

$$e_s = E_s \cos \omega_s t \tag{5}$$

and

$$e_{LO} = E_{LO} \cos \omega_{LO} t \tag{6}$$

A4391

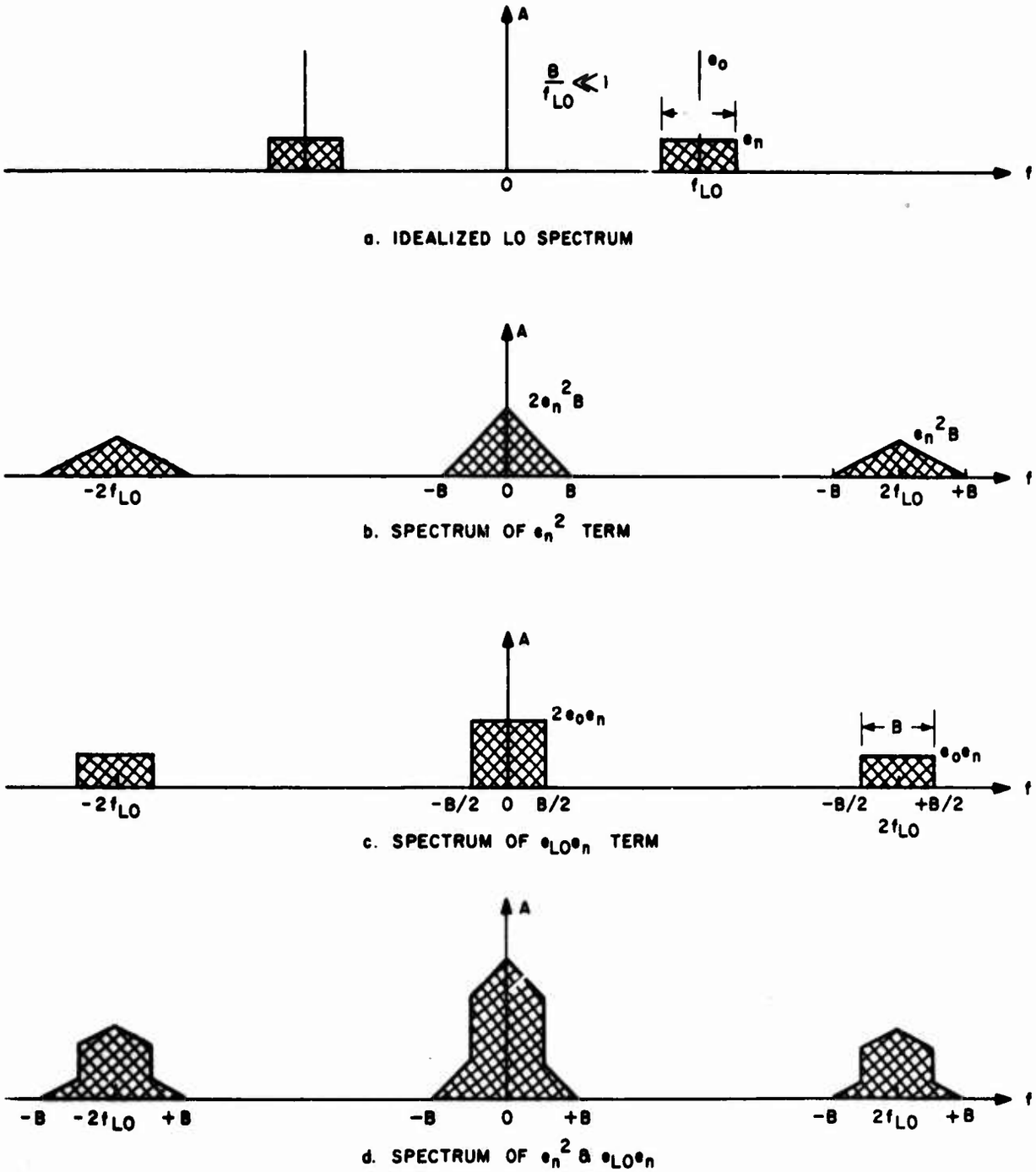

Figure 59. Noise Spectra Generated by Mixer Excited by LO with Narrowband Noise

then substituting Equations (6) and (5) into Equation (4) and omitting those undesired terms which may easily be rejected by filtering, we obtain

$$e_{out} \approx 2A_2 E_s E_{LO} \cos(\omega_{LO} - \omega_s) t + \cos(\omega_{LO} + \omega_S) t \quad (7)$$

which are the expected sum and difference frequencies of signal and LO. It is evident from the foregoing that it is the square law term which provides the required IF signal and which is necessary to the operation of a device as an efficient mixer.

Consider now the case where narrowband noise is present, together with the LO voltage applied to a mixer. An idealized spectral representation is shown in Figure 59. Returning to Equation (4), and substituting the noise voltage e_n for e_{LO}, we obtain

$$e_{out} = A_0 + A_1 (e_s + e_n) + A_2 (e_s^2 + 2e_s e_n e_n^2) \quad (8)$$

To determine the output voltage which will be passed by a filter at the IF, it is necessary to determine the spectrum of the above terms. The linear terms are merely reproductions of the input voltage with amplitude modified by the coefficient A_1, but with no change in spectrum. This is not the case, however, with those terms which are multiplied by the coefficient A_2, where we have three terms consisting of products of time functions. Resorting to the convolution theorem to obtain the spectrum of each of these products, we obtain

$$F[f_1(t) \cdot f_2(t)] = \frac{1}{2\pi} \int_{-\infty}^{\infty} F_1(y) F_2(\omega - y) dy \quad (9)$$

where

$F_1(\omega)$ is the Fourier transform of $f_1(t)$

$F_2(\omega)$ is the Fourier transform of $f_2(t)$

$F[f_1(t) \cdot f_2(t)]$ is the Fourier transform of the product of $f_1(t)$ and $f_2(2)$

after replacing ω by the variable of integration, y, and shifting $F_2(-y)$ with respect to $F_1(y)$ by ω. In the case where the spectra of $f_1(t)$ and $f_2(t)$ can be approximated in graphical form, the indicated integration can be accomplished by numerical methods. Also, the spectrum of a time function to any power can be determined by successive convolutions with itself.

Figure 61 shows the spectra resulting from the square-law term of Equation (3), or the third term in Equation (8). The e_{LO}^2 term merely results in the generation of the second harmonic of the local oscillator frequency and may be neglected for the purposes of this discussion. It is evident that the squaring process inherent in the mixer has generated two

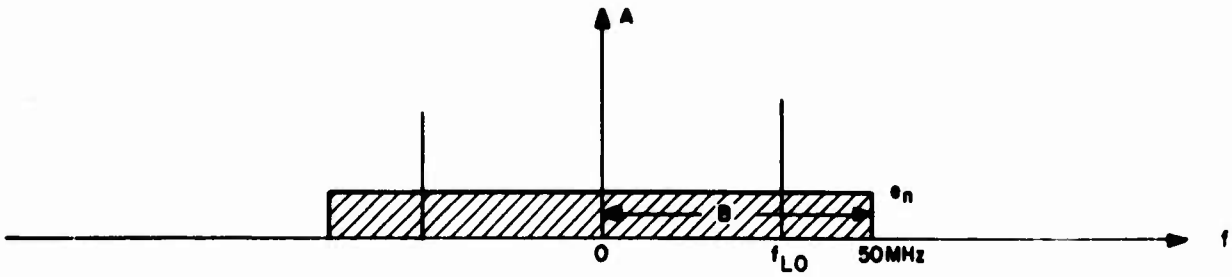

a. IDEALIZED LO SPECTRUM

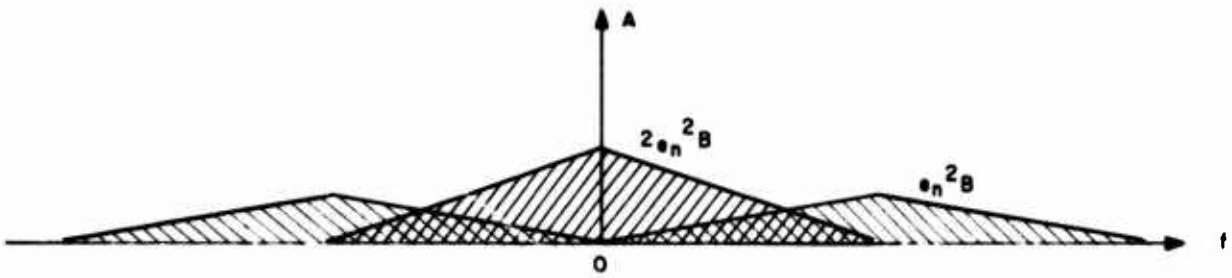

b. SPECTRUM OF e_n^2 TERM

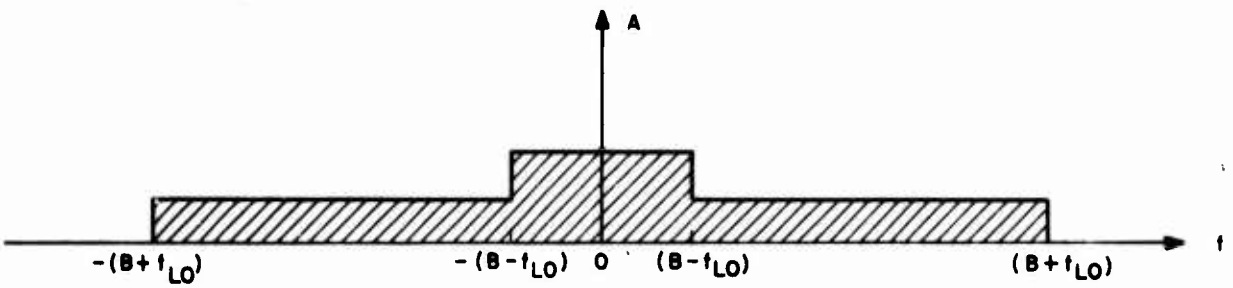

c. SPECTRUM OF $e_{LO}e_n$ TERM

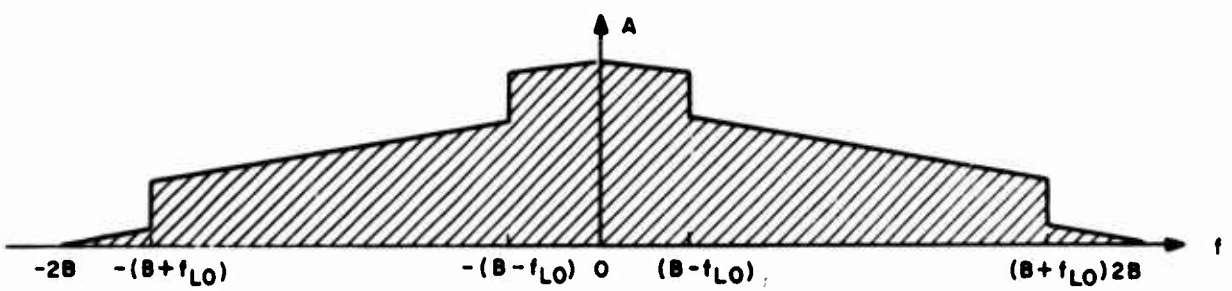

d. SPECTRUM OF $(e_n^2 + e_{LO}e_n)$

Figure 60. Noise Spectra Generated by Mixer Oscillator by LO with Wideband Noise

significant components of noise with composite spectral representation as shown in Figure 59c. Obviously, so long as

$$B < f_{IF} < (f_{LO} - B) \tag{10}$$

or

$$(f_{LO} + B) < f_{IF} < (2f_{LO} - B) \tag{11}$$

the narrowband IF amplifiers which follow the mixer will not be affected by the mixer-generated noise arising from the use of an LO containing noise.

The case illustrated above is one where the noise accompanying the LO voltage is relatively narrowband. In the case where a wideband frequency synthesizer is employed as the LO source, however, the spectra change markedly from from those in Figure 59, as shown in Figure 60. A noise bandwidth of 50 MHz is used, which is typical of the HP 5100A frequency synthesizer. In this case, it is obvious that unless

$$f_{IF} > 2B \tag{12}$$

noise generated in the mixing process will fall in the passband of the IF amplifiers which follow the mixer.

The latter of the two cases illustrated above corresponds to the one which existed in the noise/interference receiver as originally conceived. This receiver design was dictated by three requirements:

1. The first LO must be frequency agile to accomplish the required frequency scanning. This led to the use of the HP 5100A frequency synthesizer as the first LO.
2. A high LO injection level was required at the first mixer (30 dBm) in order to achieve high dynamic range.
3. Good mixer spurious and narrowband IF filter amplitude response was required, leading to the use of IFs less than (2), the LO noise bandwidth. As a result, despite the presence of bandstop filters in the first LO path designed to prevent direct LO noise transfer at the three first IFs, noise components were generated in the mixing process itself after bandstop filtering at each first IF, thereby greatly increasing receiver noise figure.

This difficulty was not evident until the delivery of the broadband LO power amplifiers which excite the receiver mixers. Previously, narrowband laboratory test equipmant amplifiers were employed to supply the required 1-W LO power, since they were the only

devices available which were capable of this power output level across the required frequency range. The relatively narrow bandwidth of these power amplifiers (typically 800 kHz at -3 dB) resulted in LO noise spectra like the narrowband case discussed above and illustrated in Figure 59.

Two solutions are available to remedy this noise problem. The first is to lower the LO injection level to the first mixer. Unfortunately, this adversely affects receiver dynamic range and is therefore an unacceptable solution. The second solution involves narrowband filtering of the first LO signal, with no penalties in receiver performance. This latter solution has been chosen for implementation.

In order to provide an interim operation capability, the proposed LO narrowbanding is being implemented in two steps. The first step (Phase I) incorporates an HP 230A power amplifier into the receiver design to furnish the first LO for each receiver channel at 30 dBm. The 800-kHz, 3-dB bandwidth of this amplifier is sufficiently narrow to alleviate the LO noise problem while simultaneously permitting automatic tuning of the receiver across any 1-MHz wide RF band in the 4- to 40-MHz range with negligible dynamic range performance penalty at the band edges (nominally 4 dB). Manual tuning of the power amplifier is required after each 1-MHz scanning operation. The second step (Phase II) involves the substitution of broadband LO power amplifiers and remotely selected narrowband bandpass filters for the narrowband manually-tuned power amplifier.

REFERENCES

1. Manning, L.A., and Eshleman, V.R., "Meteors in the Ionosphere," Proc. IRE, p. 186, February 1959.

2. Booker, H.G., and Crain, C.M., Rocket-Generated Mechanical Waves in the Ionosphere, Rand Corporation, Memo RM-2977, January 1962.

3. Briggs, B.H., "A Preliminary Report on Horizontal Drifts in the F Region During the IGY," Some Ionospheric Results Obtained During the IGY, W.J.G. Beynon, Editor, Elsemier, 1960.

4. Handbook of Geophysics and Space Environments, Shen L. Valley, Editor, Chapter 12, Air Force Cambridge Research Laboratories.

Unclassified

Security Classification

DOCUMENT CONTROL DATA - R & D

(Security classification of title, body of abstract and indexing annotation must be entered when the overall report is classified)

1. ORIGINATING ACTIVITY (Corporate author) General Electric Co. H. M. E. D. Syracuse, New York	2a. REPORT SECURITY CLASSIFICATION Unclassified 2b. GROUP

3. REPORT TITLE

Expanded Little IDA - Instrumentation

4. DESCRIPTIVE NOTES (Type of report and inclusive dates)

Interim Report #5

5. AUTHOR(S) (First name, middle initial, last name)

Coates, Raymond J.
et.al

6. REPORT DATE	7a. TOTAL NO. OF PAGES	7b. NO. OF REFS
October 1967	123	4

8a. CONTRACT OR GRANT NO.	9a. ORIGINATOR'S REPORT NUMBER(S)
AF30(602)-3946 b. PROJECT NO. 5582 c. 558202 d.	9b. OTHER REPORT NO(S) (Any other numbers that may be assigned this report) RADC-TR-67-502

10. DISTRIBUTION STATEMENT

This document is subject to special export controls and each transmittal to foreign governments, foreign nationals or representatives thereto may be made only with prior approval of RADC (EMLI), GAFB, N.Y. 13440.

11. SUPPLEMENTARY NOTES	12. SPONSORING MILITARY ACTIVITY
	RADC (EMAS) Griffiss AFB NY 13440

13. ABSTRACT

This report presents the status and description of the equipment which has been designed and configured specifically to meet the experimental objectives of the Expanded Little IDA Program. These objectives are to provide a more accurate estimate of the major environmental factors needed for over-the-horizon radar system design.

Transmitter and receiver site block diagrams and system parameters are presented. Equipments not covered in previous reports are discussed in detail.

DD FORM 1 NOV 65 1473

Unclassified

Security Classification

14. KEY WORDS	LINK A		LINK B		LINK C	
	ROLE	WT	ROLE	WT	ROLE	WT
High Frequency Propagation						
Absorption						
Ionosphere						
High Frequency Radar						